A MEASUREMENT OF THE FORWARD-BACKWARD ASYMMETRY AND $\sin^2\theta_W$ FROM THE PROCESS $Z^0 \longrightarrow \mu^+\mu^-$ AT $\sqrt{s} = 1.8$ TEV

by

LEIGH ANN MARKOSKY

A thesis submitted in partial fulfillment of the requirements for the degree of

DOCTOR OF PHILOSOPHY

(Physics)

at the

UNIVERSITY OF WISCONSIN - MADISON

1992

E-741

Abstract

A measurement of the forward-backward charge asymmetry in the decay of Z^0 bosons produced from $\bar{p}p$ collisions at $\sqrt{s} = 1.8$ TeV at the Fermilab Tevatron collider, and decaying to $\mu^+ \mu^-$ pairs is presented. From this asymmetry, a value for the Weinburg angle, $\sin^2 \theta_W$, is extracted and compared to values from other experiments.

AAC6512

Acknowledgements

I would like to thank the following persons for their help along the way: First, my thesis advisor, Lee Pondrom, for supporting me for the past six years. Hovhannes Keutelian, for helping me to get started early in my career. Also, Peter Hurst, for his assistance with this analysis. Finally, my parents, for their love and support.

This work was supported by the United States Department of Energy Contract DE-AC02-76ER00881.

Contents

List of Tables

List of Figures

Chapter 1

Apparatus

1.1 The Tevatron Collider

The Fermilab Tevatron is currently the world's largest proton- anti-proton collider. Its design energy is 1000 GeV/beam (1 GeV = 10^9 electron volts), and it is currently operating at $\sqrt{s}$ = 1.8 TeV (1 TeV = 10^{12} eV). In the first step of the process which produces 900 GeV protons and anti-protons, 750 keV H^- ions are injected from a Cockroft-Walton Generator into a linear accelerator, where they are accelerated to .5 GeV and then injected into the booster ring. See Figure 1.1. The ions are stripped of their electrons and then further accelerated to 8 GeV. They are then injected into the Fermilab Main Ring, a proton synchrotron two kilometers in diameter, which serves as the injector for the Tevatron, and also as the source of protons for anti-proton production. To produce anti-protons, 120 GeV protons are peeled off from the main ring and focused on a tungsten

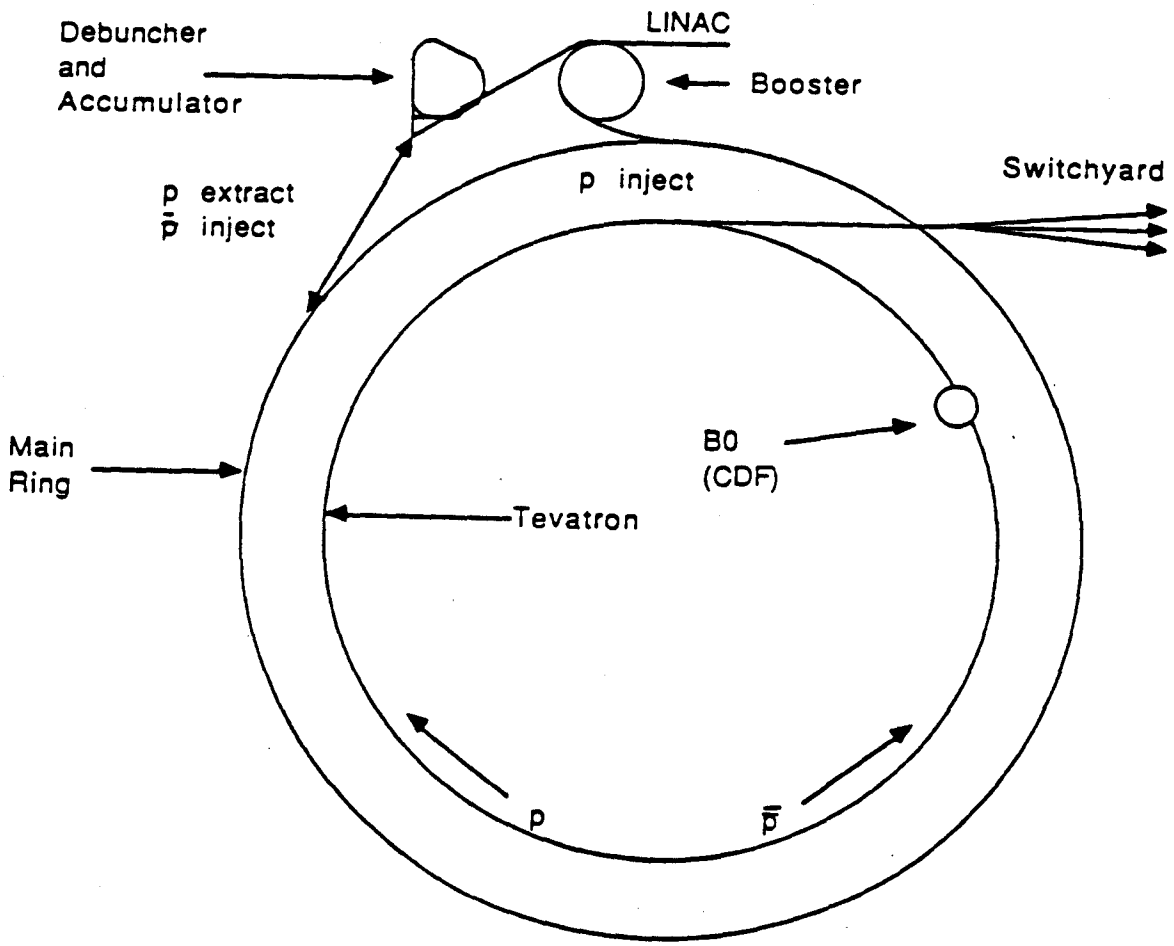

Figure 1.1: Overhead view of the Fermilab accelerator complex.

target. The resulting $\bar{p}$'s are focussed with a lithium lens and injected into the Debuncher storage ring with an energy of approximately 8.5 GeV, at time intervals of 3 seconds. Once in the debuncher, the anti-protons undergo stochastic cooling to reduce their transverse emittence (or the amount of phase space the particles occupy in the transverse plane), and rf bunching (bunch rotation) to reduce their momentum spread. Stochastic cooling refers to a technique of sampling the average direction of protons within a bunch, and quickly applying a magnetic 'kick' to the bunch to get the average direction of travel better aligned along the beam pipe. The bunch rotation technique uses rf power to decrease the energy spread of the particles within the bunch while increasing their time spread in order to maintain a constant area in phase space. The bunches remain in the Debuncher for 2 seconds, during which time they experience successive applications of bunch rotation and stochastic cooling. Then, the partially cooled anti-protons are injected into the Accumulator where they undergo further stochastic cooling and are stored in a 'stack' until ready to be injected into the Tevatron for their final acceleration. Six proton bunches are injected into the Tevatron first, and once sufficient $\bar{p}$ have been accumulated, 6 bunches of anti-protons are extracted from the Accumulator, injected back into the Main Ring where they are accelerated to 150 GeV, and then into the Tevatron. As the protons and anti-protons enter the Tevatron, they encounter a system of dipole and quadrupole magnets, interspersed with RF cavities, similar to that in the Main Ring. The dipole magnets bend the bunches around the path of the Tevatron; the quadrupoles focus the

bunches down to increase their density, and hence the rate at which $p\bar{p}$ interactions occur, i.e. the luminosity. This 6 bunch scheme creates 12 $p\bar{p}$ intersection points along the ring. The position of these crossings is modified by the radio-frequency cavities using a technique called 'cogging', in which the positions of the crossing points are adjusted to coincide with the positions of the particle detectors. Once the beam has been successfully cogged, the bunches are accelerated to 900 GeV. The low beta quadrupole magnets located around the beam pipe inside the B0 collision hall then squeeze the beam down to increase its density as much as possible and maximize the interaction rate. The final step is scraping, in which eliminates some of the beam halo, the stray protons and anti-protons travelling around the tevatron at the edges of the bunches. The bunches have a gaussian shape in three dimensions; and the beam luminosity is given by

$$\mathcal{L} = \frac{N_p N_{\bar{p}} C}{4\pi\sigma^2} \tag{1.1}$$

where N_p is the number of protons in the bunch, $N_{\bar{p}}$ is the number of anti-protons, C is the crossing rate of the bunches (every 3.5 μsec), and σ is the rms width of the bunch in the plane transverse to the direction of motion. CDF measured luminosity using the beam-beam counters (BBC). These consisted of two planes of concentric rings of scintillator placed symmetrically east and west about the interaction point, between the forward detectors and the central detectors. The BBC also served as a minimum bias trigger for the entire CDF detector. When a hit was recorded in both the east and west side counters within the time window

allowed for particles coming back from the interaction point, the detector read-out was triggered. The cross-section for the BBC was 44 mb. So, the luminosity observed at CDF was

$$\mathcal{L} = \frac{\mathcal{R}}{44\text{mb}} \tag{1.2}$$

where $\mathcal{R}$ was the measured rate of $\bar{p}p$ collisions. The error on $\mathcal{L}$ is 8%.

1.2 The CDF Detector

The Collider Detector Facility at Fermilab is a multi-component high- energy particle detector weighing 5000 tons and composed of three tracking systems, seven calorimeters, two muon detectors, and a silicon vertex detector in the forward region. Beam-beam counters provided luminosity information and a minimum bias trigger (discussed briefly in the previous section). A super-conducting solenoidal coil provided a uniform 1.4116 Tesla magnetic field to study charged particle momenta in the central region. A pair of iron toroids placed symmetrically east and west served the same purpose for the forward muon detector. The following sections will contain brief descriptions of the detector systems relevant to the analysis of this thesis. Detailed information of the entire CDF detector is available elsewhere [2]. The lay-out of the CDF detector and its coordinate system are shown in two perspective views in figure 1.2 and figure 1.3. The CDF

convention for pseudo-rapidity, η is

$$\eta = -ln(tan\frac{\theta}{2}) \tag{1.3}$$

1.2.1 The VTPC

The VTPC consisted of eight Vertex Time Projection modules surrounding the 5.08 cm Beryllium beam pipe about the collision point. See Figure 1.4. The chambers extended a total length in z of 2.8 m and in radius from 6.8 cm to 21 cm, and covered pseudo-rapidities $-2.6 < \eta < 2.6$. The VTPC was used to determine the vertex postion of a charged particle's track by measuring its direction in the $r-z$ plane. Each module was divided into two 15 cm long regions by a high voltage grid. At the end of both of these regions was a proportional chamber segmented azimuthally into 45° octants. Each octant consisted of a layer of 24 anode drift wires strung azimuthally, as shown in figure 1.4, and a layer of 24 cathode pads. The drift regions contained a 50-50 mixture of argon and ethane. Charged particles crossed the drift regions, the electrons from their ionization trails drifted along the z direction to the wires. Their drift times gave the $r - z$ position of the track. The azimuthmal segmentation of the modules gives ϕ information. Also, adjacent modules were rotated in ϕ by 11.3° to give stereo information and to help compensate for inefficencies around octant and module boundaries when the track crossed more than one module. The VTPC

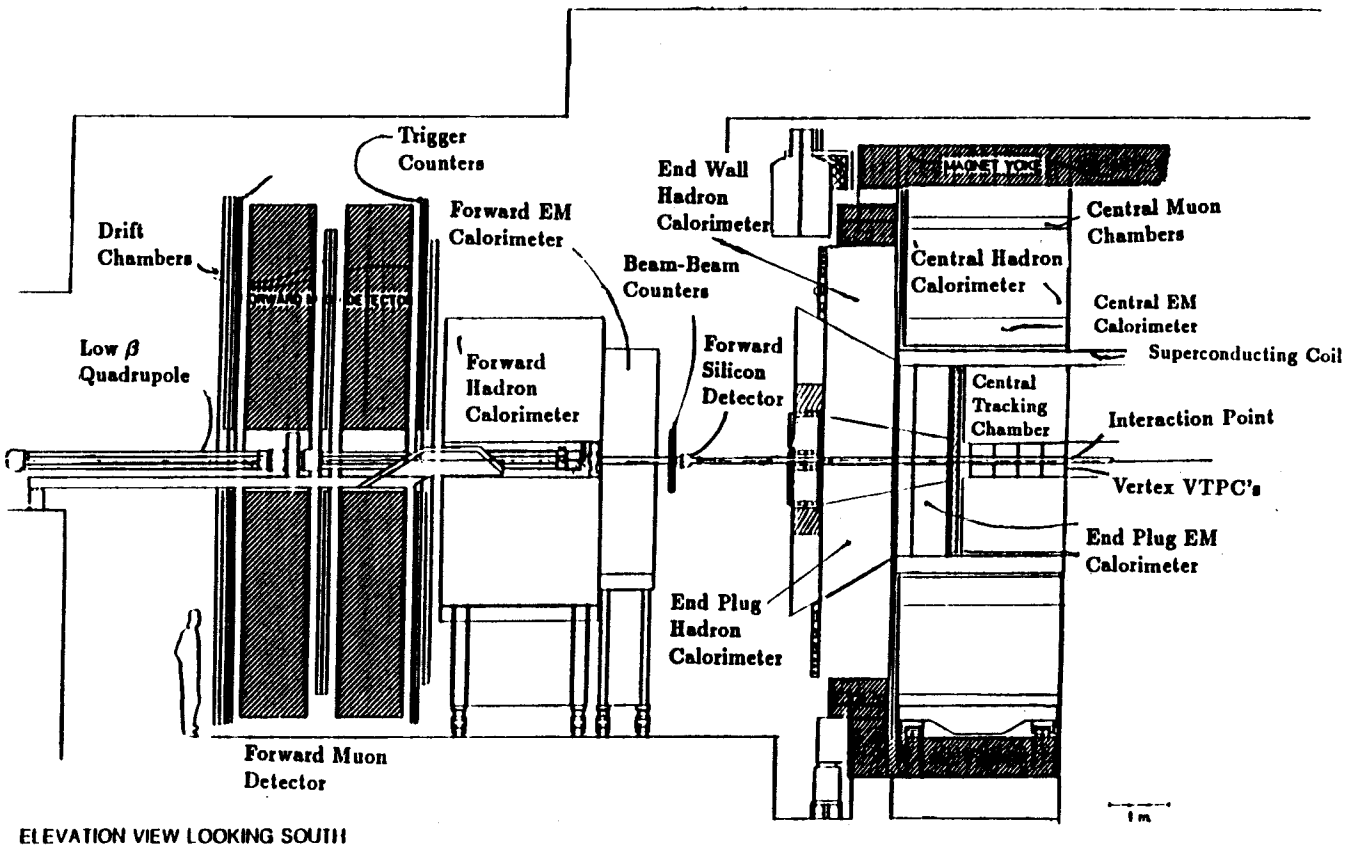

Figure 1.2: Side view of the CDF detector.

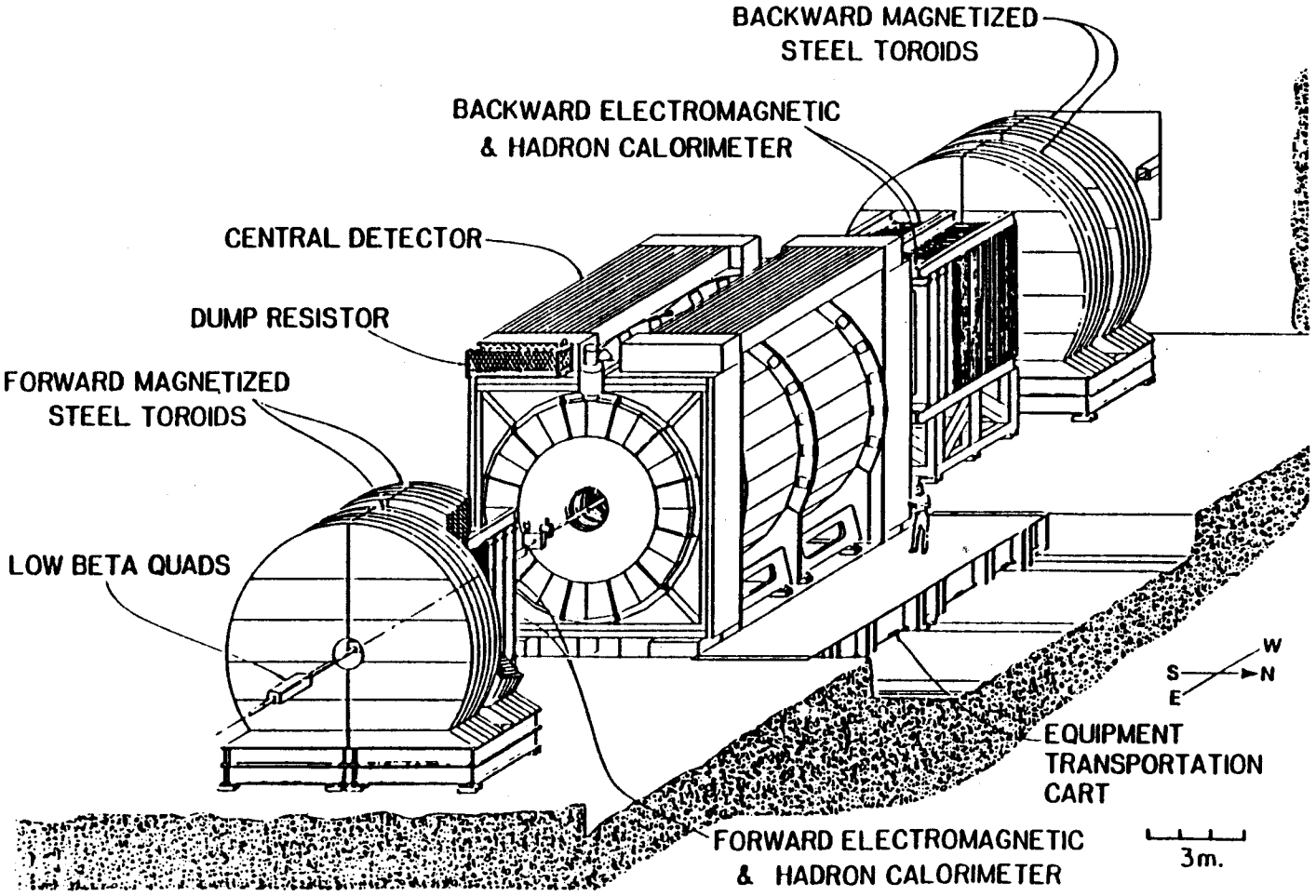

Figure 1.3: Perspective view of the CDF detector.

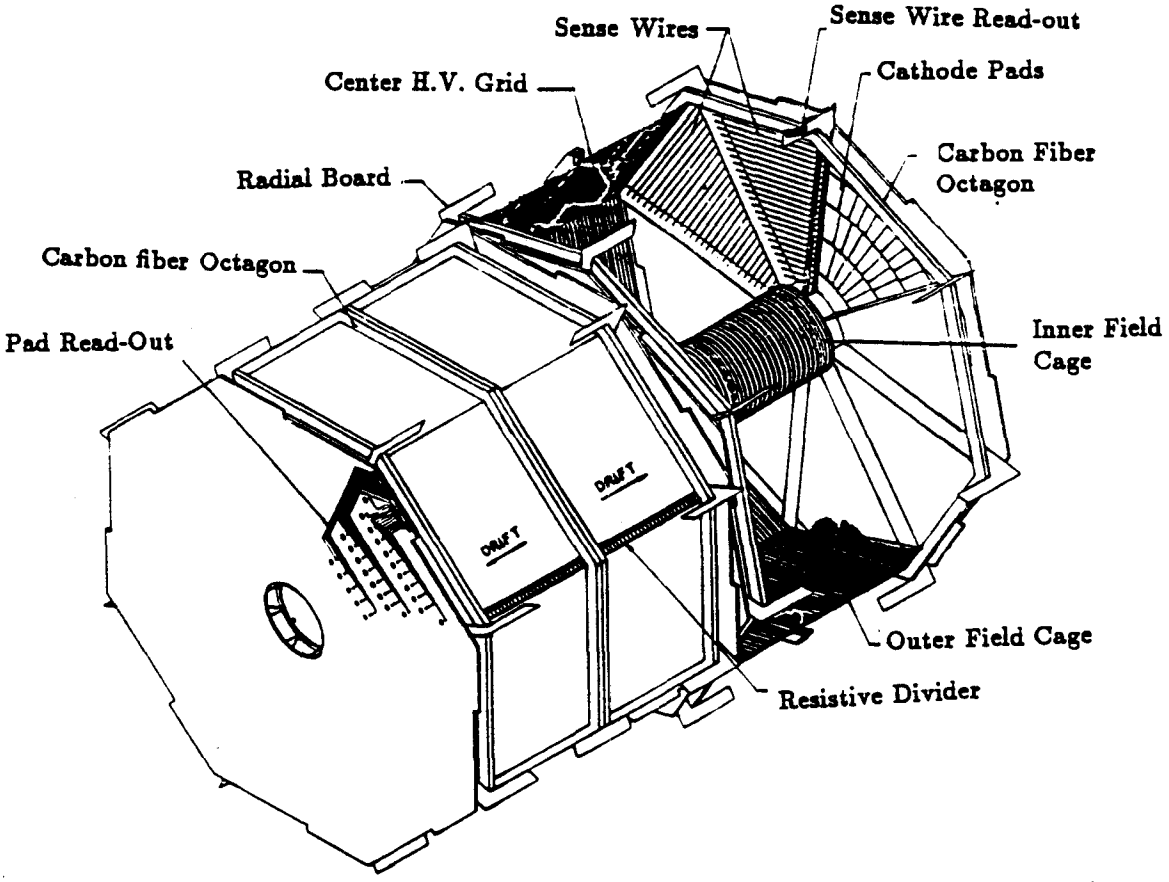

Figure 1.4: The VTPC.

had an rms resolution in the z direction of 1 mm.

1.2.2 The Central Tracking Chambers

The CTC was a cylindrical drift chamber 3.2 meters long, with an inner radius of .3 meters, and an outer radius of 1.3 meters, and was located just outside the VTPC. The CTC was surrounded by a super-conducting solenoidal coil of NbTi/Cu 3 meters in diameter and 5 meters long with 1164 turns. The coil provided the CTC and VTPC a uniform magnetic field of 1.4119 Tesla, making possible the precision measurements of charged particle momenta for which these tracking detectors were designed. The momentum of a particle crossing the CTC was extracted by measuring the curvature in the $r - \phi$ plane of that particle's track, which was reconstructed from the positions of the ionization trails left in the CTC's drift cells. The CTC was composed of 84 layers of sense wires, strung axially (i.e. along z) and grouped into 9 so-called 'super-layers'. These super-layers are shown numbered in an end-on view of the CTC in figure 1.5. Wires within each super-layer were grouped into drift cells having a constant drift time of about 800 nanoseconds. Five of these layers had 12 wires per drift cell, and were designated 'axial super-layers', since their sense wires ran strictly parallel to the z axis. These cells provided information in the $r - \phi$ direction. The other four super-layers were called 'stereo layers' since their sense wires were tilted 3° with respect to the beam direction to provide a stereo information (i.e. in the $r - z$ direction). The electrons resulting from the passage of a charged

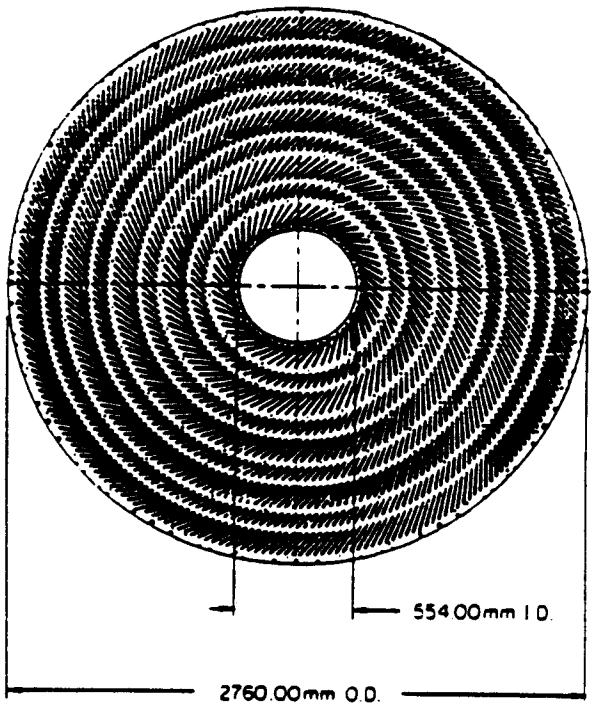

Figure 1.5: $R-\phi$ view of the CTC with its 9 superlayers of wires

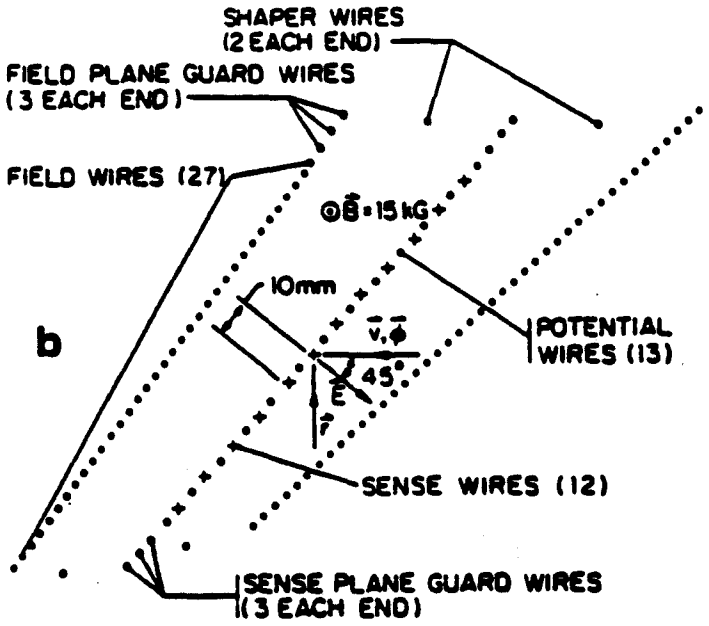

Figure 1.6: Wire geometry for the CTC superlayer cells

particle drifting in the purely axial magnetic field of the solenoid experienced a force which had components in both the radial and azimuthal directions. The radial component results in a non-linearity in the time-distance relationship of the CTC cells. To compensate for this, the sense wires of the CTC were all tilted by 45° relative to the radial direction. See figure 1.6. This adjustment in the direction of the electric field of the sense wires compensated for the radial component of the magnetic force felt by the drift electrons. Hence, motion in the fields was approximately azimuthal. The nine CTC super-layers covered the pseudo-rapidity region $-1 < \eta < 1$. The momentum resolution in this region

was $\frac{\delta p_t}{p_t^2} < 0.002$. Adding a vertex point to the track extended the effective track radius, l, to 1.3 meters, and improved the rms resolution, which scales as $\frac{1}{Bl^2}$, to $\frac{\delta P_t}{P_t^2} < 0.0011$ (where B is the value of the magnetic field).

1.2.3 The Calorimeters

1.2.3.1 The Central Electromagnetic and Hadronic Calorimeters

The CDF calorimeter system can be divided into three regions: Central ($|\eta| < 1.1$), Plug ($1.1 < |\eta| < 2.4$), and Forward ($2.2 < |\eta| < 4.2$). They were designed to measure the energies and position of hadronic jets and electromagnetic showers. All of the calorimeters were segmented into projective towers (i.e. pointing back to the origin), with each electromagnetic shower counter tower laying in front of a corresponding hadronic shower counter tower. In the central region, the towers subtended the area in $\eta - \phi$ space $\Delta\eta = .1$ and $\Delta\phi = 15°$. In the plug and forward regions, $\Delta\eta = .1$ and $\Delta\phi = 5°$. The central electromagnetic and hadronic calorimeters were constructed in wedges subtending 15° in ϕ and grouped together in 4 'arches' symmetrically east and west around the solenoid and central tracking chamber (refer to Figure 1.3). Each wedge contained an electromagnetic shower counter, with a hadronic calorimeter module directly behind it. Figure 1.7 is a cut-away view of one central wedge showing a central electromagnetic calorimeter module with its light collection and transmission system. The electromagnetic shower modules consisted of polystyrene scintillator and lead sandwich comprising

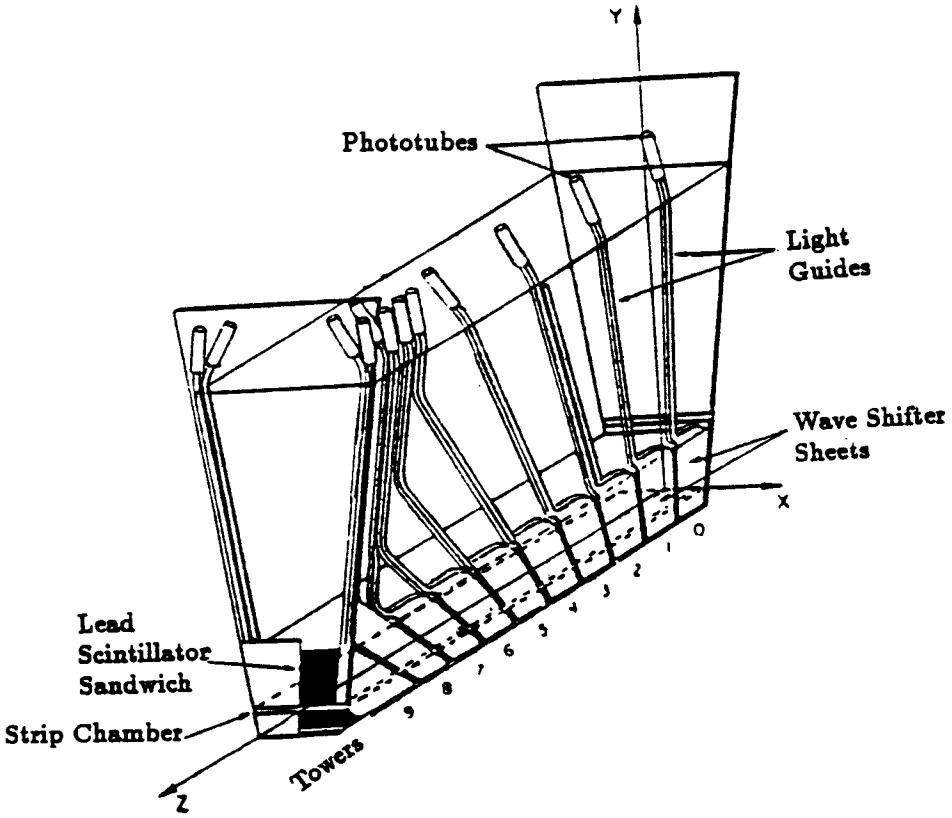

Figure 1.7: A cutaway view of a central calorimeter wedge.

18 radiation lengths of material (this counts the inner wall of the wedge and the coil). Each module contained 10 towers. Light from the scintillators was collected via wave-guides positioned on each side of the tower and leading to phototubes at the top of the wedge. At a depth of 6 radiation lengths was a strip chamber (Central Electromagnetic Strip chamber - CES) used to determine the shower position in ϕ and z by measuring the charge depostion on orthogonal strips and wires. The CES was shown by test beam electrons to have a resolution of 2 mm. The energy resolution for CEM shower modules (also determined from test beam

data) was given by

$$\frac{\sigma_E}{E} = \sqrt{(\frac{13.5\%}{\sqrt{E sin\theta}})^2 + (2\%)^2} \tag{1.4}$$

where the first term under the square root was the energy resolution for an indiviual tower, and the second term took into account variations in individual tower response across the whole calorimeter (variation in actual detector response, and shower leakage). The Central Hadronic modules (CHA) were located in the wedges just behind the CEM modules. These modules consisted of 6 interaction lengths of iron-scintillator sandwich (with the same tower geometry as the CEM module). The energy resolution of the CHA was given by

$$\frac{\sigma_E}{E} = \frac{80\%}{\sqrt{E \sin\theta}} + 4\% \tag{1.5}$$

which was about 4 times higher than that of the Central Electromagnetic calorimeter.

1.2.4 The Gas Calorimeters

The Plug and Forward calorimeters were all composed of layers of gas- filled proportional tubes with cathode pad read-out sandwiched with layers of lead or iron absorber. The gas sampling tubes for the four detectors all had basically the same design. The tube was made up of resistive plastic with an anode wire held at high voltage running down its center. Above and below the tubes were layers of G10. The lower surface of the upper layer was covered with copper which had been etched into pads .1 in η by 15° in ϕ and connected to charge integrated

amplifiers. When a charged particle passed through the tube, it ionized the gas, the electrons move towards the anode wire, leaving a cloud of positive ionization in the gas. This induced an opposite charge on the pads which was digitized and read-out. The gain of gas proportional tubes was sensitive to not only the gas composition, but also to air pressure and temperature. The gain of the gas in these in tubes of all of the gaseous calorimeters was carefully monitored during the run using a system of smaller proportional tubes containing Fe^{55} sources. The position of the peak produced by the 6 KeV photon from the Fe^{55} is a well-known quantity. Shifts in this peak versus changes in gas gain were mapped in the test beam, and this information was used during the run to adjust the data online on a run by run basis. The Plug Electromagnetic Calorimeter (PEM) was composed of 34 layers of proportional tubes (running vertically to the beam) interleaved with lead sheets 2.7 mm thick. It was separated into four quadrants, covering the eta range $1.1 < |\eta| < 2.4$. The cathode pads of the tubes were ganged together to form three depth segments: layers 1-5, 6-29, and 30-34, which were read-out separately. Individual layers were also read-out. The depth segments gave an idea of the longitudinal development of a shower. Layers 6-15, near shower maximum, also had $\theta - \phi$ cathode strips which gave further spatial information. The gas in the tubes was a $50\% - 50\%$ mixture of Argon-Ethane bubbled through methanol. The energy resolution of the PEM, as determined in a test beam with 50 GeV Electrons was

$$\frac{\sigma_E}{E} = \frac{28\%}{\sqrt{E}} + 2\% \tag{1.6}$$

The Plug Hadron Calorimeter (PHA) was composed of 20 layers of tubes separated by 5 cm thick steel absorber. The tubes were arranged in the ϕ direction in 30° wedges. 20 layers of tubes in a wedge formed a 'stack'. The cathode pads were ganged together to form projective towers 20 layers deep and 1 pad wide. The wires from each layer, in each stack are also ganged together to give longitudinal information on the shower development. The η coverage of the PHA is $1.3 < |\eta| < 2.4$. The gas used was $50 - 50$ Argon-Ethane, bubbled through methanol. Its gain was monitored as described above. The energy resolution of the PHA was determined in the test beam to be

$$\frac{\sigma_E}{E} = \frac{86\%}{\sqrt{E}} + 4\% \tag{1.7}$$

1.2.5 The Forward Calorimeters

The Forward Electromagnetic Calorimeter (FEM) covered the eta range $2.2 < |\eta| < 4.2$. It consisted of 30 layers of tubes with 4.5 mm lead sheets divided into four independent quadrants. The segmentation of the cathode pads was .1 in η and 5° in ϕ. The towers in the first 15 layers were ganged together, and also in the layers 16-30 giving 2 signal per tower. The wires of each layers were also ganged together in groups of 25, and were read out to give longitudinal shower information. The gas was also $50 - 50$ Argon-Ethane, and was bubbled through

isopropynol. The energy resolution measured in the test beam was given by

$$\frac{\sigma_E}{E} = \frac{25\%}{\sqrt{E}} + 0.5\% \tag{1.8}$$

The Forward Hadronic Calorimeter (FHA) covered the η region $2.3 < |\eta| < 4.2$. It was composed of 27 layers of tubes separated by 5 cm thick layers of steel, and was also divided into quadrants. The wires were read out in regions, and the segmentation of the cathode pads was the same as for the FEM. The gas was also the same as the FEM, as was the system of gas gain monitoring. The energy resolution was approximately

$$\frac{\sigma_E}{E} = \frac{140\%}{\sqrt{E}} \tag{1.9}$$

1.2.6 The Muon Detectors

1.2.6.1 The Central Muon Detector

The Central Muon chambers (CMU) provided muon detection in the eta range $0.04 <| \eta |< .61$. Each chamber consists of four layers of 4 drift tubes filled with 50-50 Argon-Ethane. The chambers were mounted in sets of three at the ends of the central calorimeter wedges as shown in figure 1.8, and sit 3470 mm from the beam line. The three chambers in each wedge covered 12.6° in ϕ, leaving gaps of 2.4° in the ϕ coverage of the chambers. There were also 1.5° cracks at $\theta = +90°$ where the calorimeter arches met. An end-on view of the chambers is shown

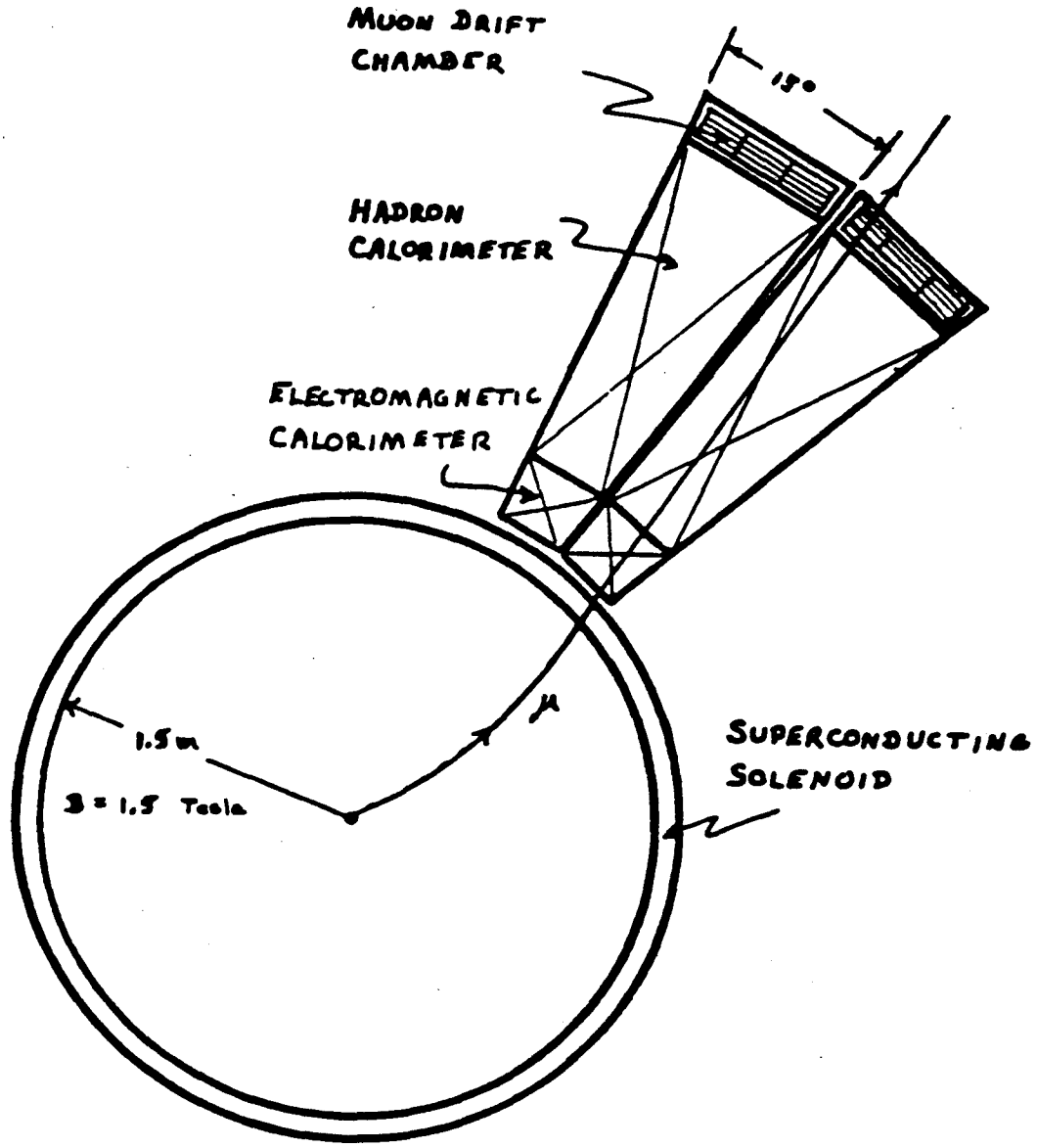

Figure 1.8: $R - \phi$ view of the contents of two central wedges, showing their position relative to the CTC and solenoid.

in figure 1.9. The drift cells were rectangular, 63.5 mm wide by 25.4 mm high by 2300 mm long. The anode wire in the center of the cell was stainless steel, 50 μm in diameter, and ran the length of the drift cell (230 cm). It was held at +3000 volts. There were aluminum field-shaping cathodes at each end of the cells which are held at −2500 volts. This makes for a drift velocity of $4.5 cm/\mu sec$ and a maximum drift time of about $700 ns$. Strips of G10 insulated the tube layers within a chamber from one another, and the cathodes from the grounded planes between the layers. From figure 1.9, one sees that the top two layers of chambers were offset by 2 mm relative to the bottom two. This arrangement was used to resolve the left-right ambiguity as to which side of the wires a particle passed. Alternate wires in a layer were ganged together to make a total of 8 anode wires per chamber. As there were 48 wedges in the detector, with 3 CMU chambers per wedges, there a total of 1152 read-out channels in the system. Streamer pulses in the gas produced by the passage of a charged particle through the chambers were collected on 1 μF blocking capacitors at each end of the anode wires. These capacitors were connected to the Rabbit muon ADC/TDC cards. These cards used the relative amounts of charge arriving at each end of the a wire (within a given time window) to perform charge division, in order to get the position, L, of the hit along the wire using

$$L = \frac{Q_L - Q_R}{Q_L + Q_R} \tag{1.10}$$

where Q_L and Q_R were the amounts of charge collected on the right and left-

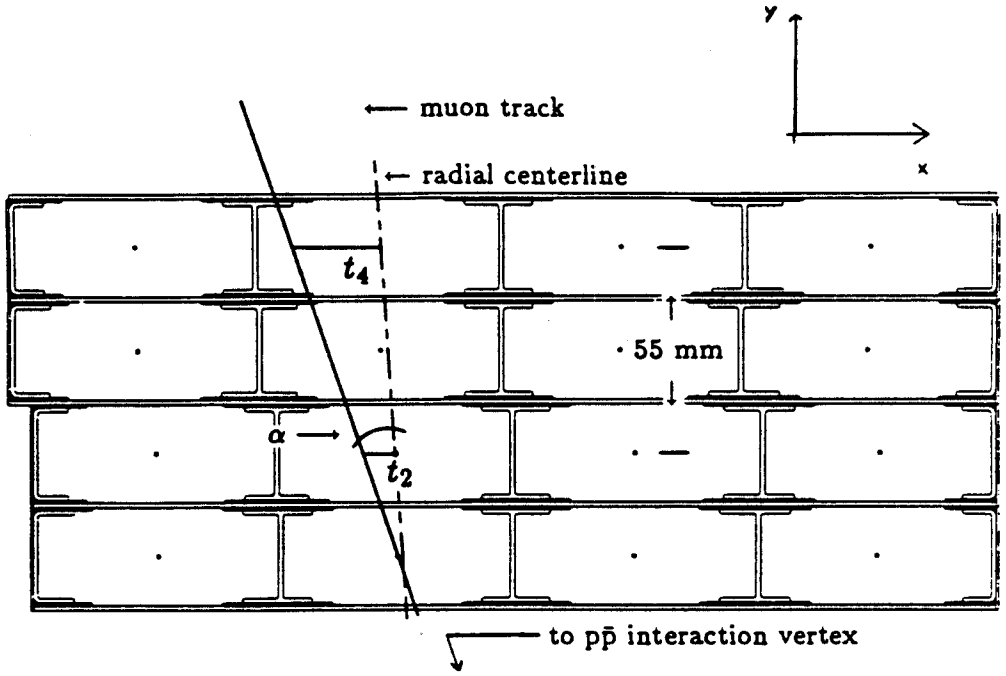

Figure 1.9: Cross-section view of one module of central muon chambers. There were three modules inside each wedge.

hand sides of the wire. To get the conversion from L to the detector coordinate z, charge division was done using hits from weak Fe^{55} sources mounted in the chambers at known z positions. This provided the $L - z$ calibration. The TDC got the drift distance in the $r - \phi$ plane to the wire from the drift velocity in the gas and time elapsed between the start of the clock at beam crossing and the arrival of the signal at the TDC. Cosmic ray studies showed the resolution of the chambers in the drift direction to be $250\mu m$, and along the wire direction to be 1.2 mm. Multiple scattering in the steel (in components prior to the CMU chambers) severely limited their momentum resolution:

$$\frac{\delta P_t}{P} \simeq 60\% \tag{1.11}$$

and so the momentum measurements for muons falling in this η range was derived from the portion of their tracks left in the Central Tracking Chambers (which were described in an earlier section).

1.2.6.2 The Forward Muon Chambers

The forward muon detector consisted of 6 planes of wire chambers and four planes of scintillators separated by steel toroids. See Figures 1.2 and 1.10. The drift chambers provided particle tracking with a possible 6 wire hits defining a track. The scintillators were intended as a fast trigger, and also give ϕ resolution of 15 degrees. The magnetic field of the toroids bent the particle trajectory for a

curvature measurement from which momentum was derived according to

$$P \cdot cos\lambda = 0.3qBR \tag{1.12}$$

where P was the particle's momentum in GeV/c, λ was the pitch angle ($\simeq$ 0 here), q was the particle's charge, B was the magnetic field in Tesla, and R was the radius of curvature in meters.

1.2.6.3 The Toroids

The forward toroids each consisted of 395 tons of steel with 4 rectangular copper coils of 28 turns apiece giving an azimuthal magnetic field. The toroids were 1 meter wide, with radius of .5 meters, and outer radius of 3.8 meters. The magnets were constructed in two halves which could be pulled apart to allow access to the detector components. A 3mm gap where the halves met at the top of the detector allowed for the insertion of a Hall probe to perform magnetic field measurements. With a current of 1000 amps in the coil, the field varied from 2.0 tesla at the inner radius to 1.6 tesla at the outer radius.

1.2.6.4 The Drift Chambers

Each plane of drift chambers consisted of 24 wedge-shaped chambers arranged radially about the beam pipe. See figure 1.10. Dead spots at wedge boundaries were eliminated by staggering each wedge relative to its neightbors to create overlap regions. Each chamber contained two layers of 96 stainless steel anode

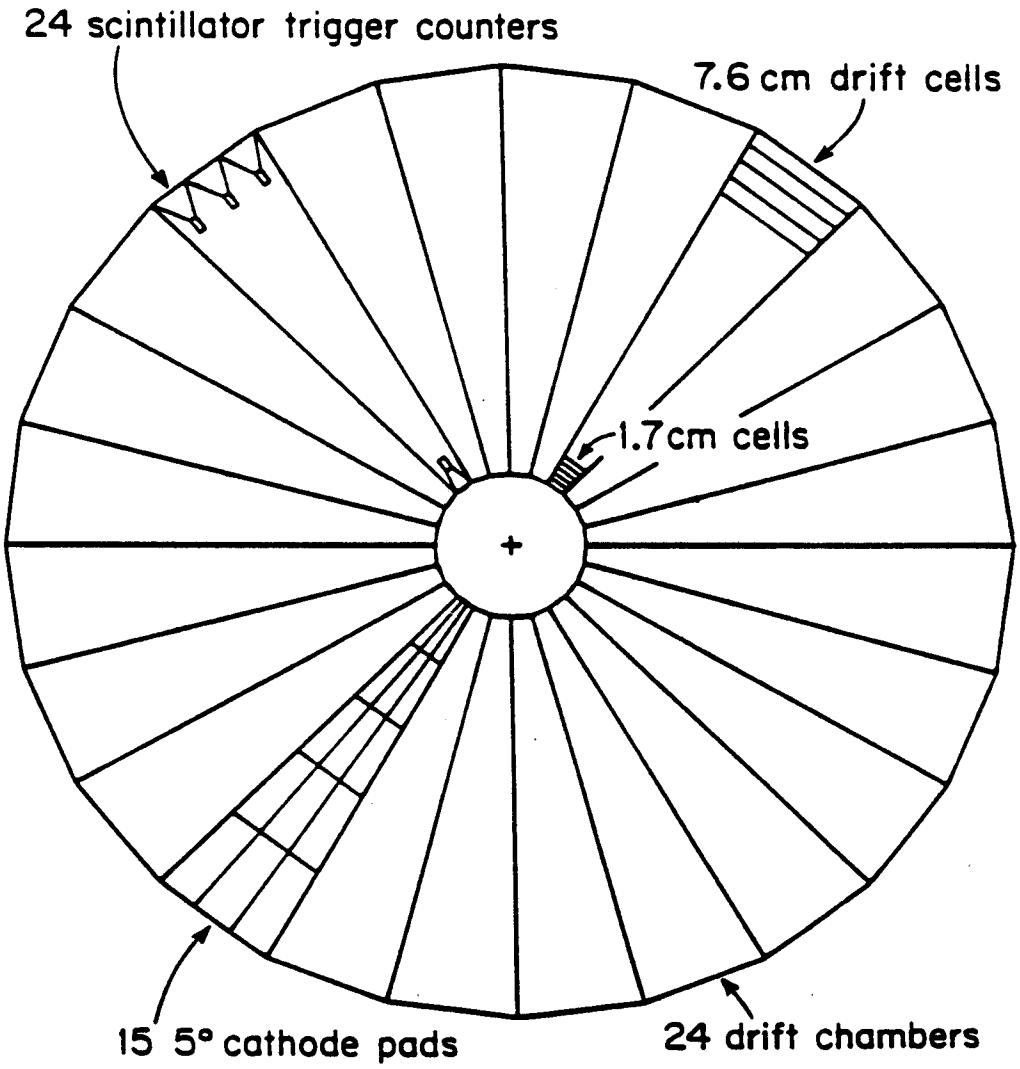

Figure 1.10: R-ϕ view of one of the forward muon detector planes showing the segmetation in ϕ and η of the chambers and pads, the scintillation counters, and the direction of the wires in the drift chambers.

wires, 63 microns in diameter. The wires ran in an azimuthal direction and were separated from each other by copper-clad G10 divider walls to form separate drift 'cells'. See Fig 1.11 The two layers shared a common copper cathode plane, divided into 15 cathode pad segments, 5° in ϕ and $\simeq$ .35 in η, which improved the ϕ segmentation of the system to 5°. The inner layer of wires (nearest in z to the interaction point) was referred to as the 'coordinate' layer, and the outer layer as the 'ambiguity'. The ambiguity layer was so called since its purpose was to resolve the left right ambiguity involved when a particle traversed a coordinate cell. Each chamber covered an area 15 degrees in azimuth, and from 1.95 to 3.65 in pseudorapidity. The wires were maintained at positive high voltage, and the cells were graded in width with polar angle in order to maintain a constant η byte of $\sim$ 0.03 per cell. This resulted 12 different cell widths per chamber, for a particular plane, and 36 different cell widths in the whole detector. See figure 1.12. In order to maintain a uniform electric field and drift velocity for all cells, 36 positive high voltage supplies, one for each cell size, were needed. The gas used was a 50-50 mixture of argon-ethane. The chambers are operated in saturation mode (i.e. the wire voltage is high enough so that drift velocity is a constant), with the drift velocity equal to 5 cm/ microsecond. The chambers relied on the build-up of positive charge on the inner surface of their cell walls for field-shaping. In this process, radiation in the collision hall (beam halo, gammas, charged particles) ionized atoms in the gas; the electrons moved towards the anode wire and the positive ions moved towards the insulating walls. The

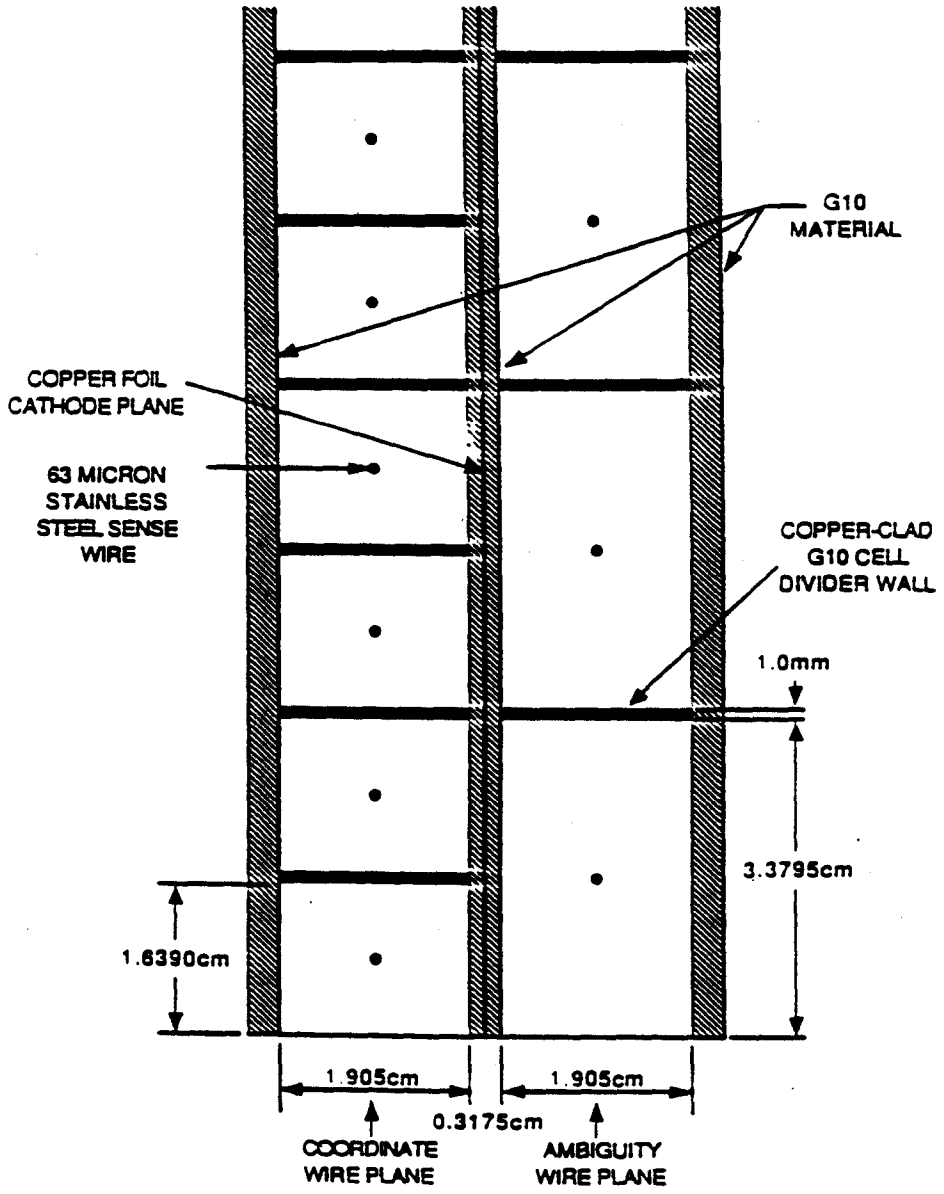

Figure 1.11: Schematic of the fmu chamber geometry and materials. The dimensions shown are for a front plane, inner radius drift cell.

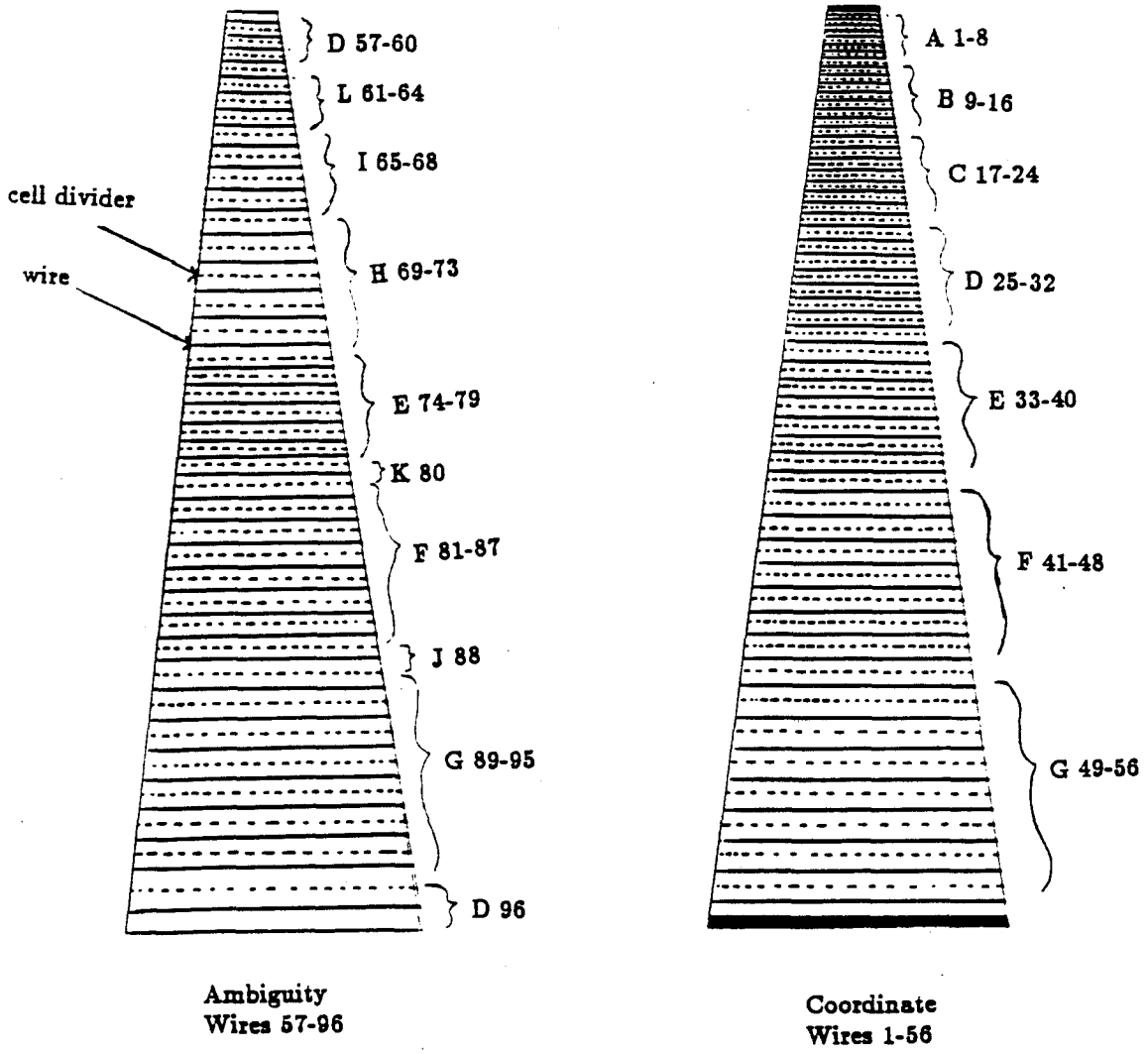

Figure 1.12: Drift cell sizes in an FMU chamber

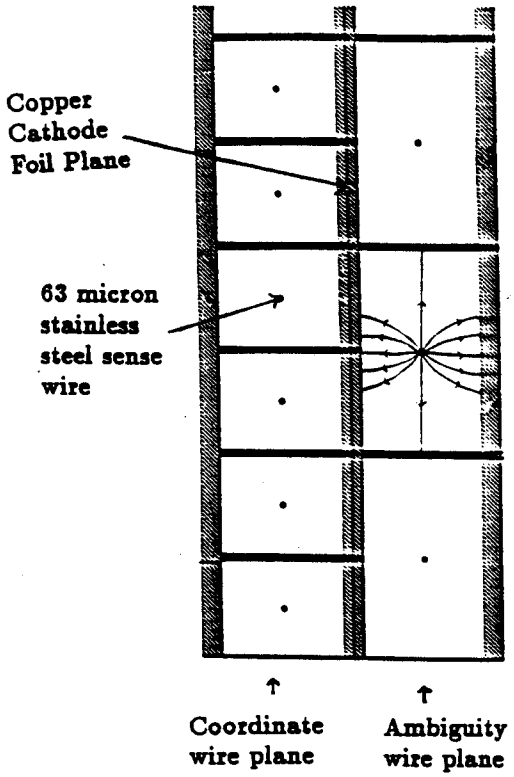

Figure 1.13: Electric Field lines inside an FMU chamber drift cell shortly after HV turn-on

electric field in the cell changed from an initial state shown Figure 1.13 to that of figure 1.14. The radiation levels in the CDF collision hall were high enough that stable gain was achieved in less than one hour of beam time. Eventually, however, enough positive space charge built up in the cell that the field lines became distorted as in figure 1.15 In this situation, areas of the cell began to 'go dead', and the response of the cell deteriorated, necessitating an increase in the anode voltage to recover a uniform field gradient. The cell gains were monitored, and the subsequent high voltage adjustments made, using a read-out

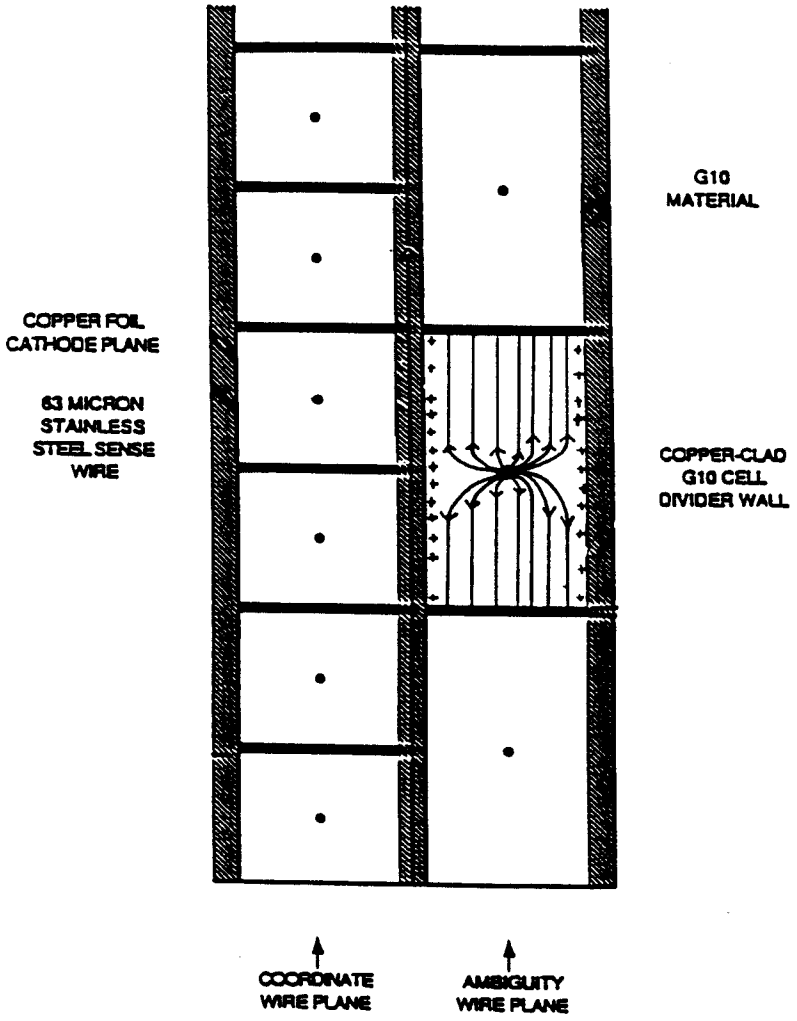

Figure 1.14: Electric field lines inside an FMU chamber drift cell after stable running conditions are achieved

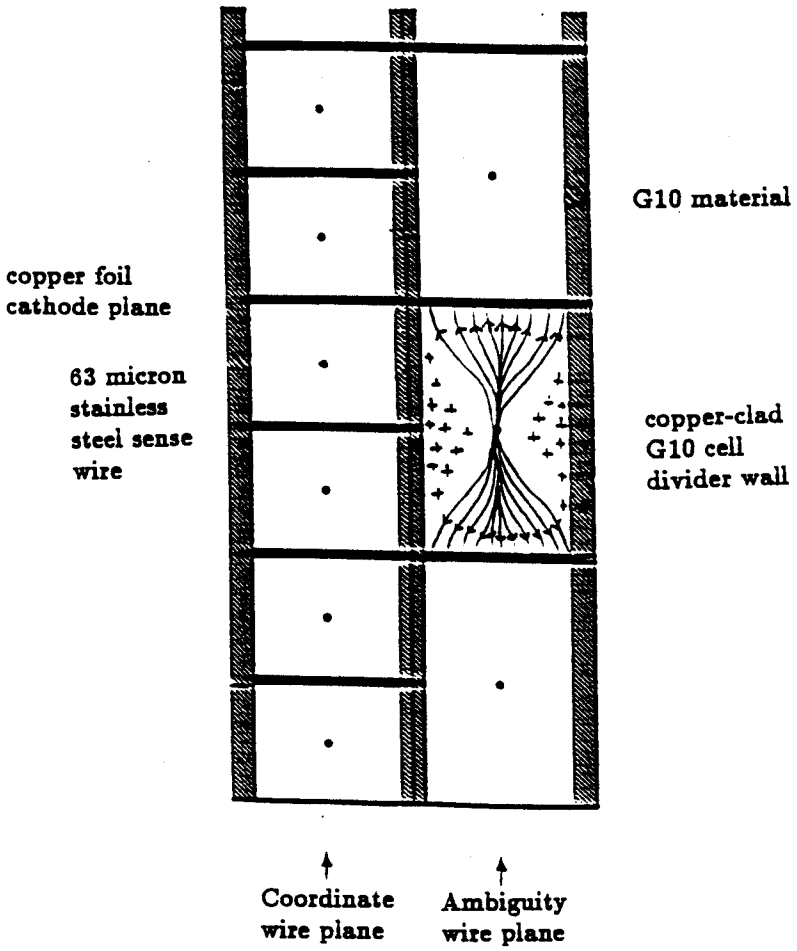

Figure 1.15: Distortion of electric Field lines inside an FMU chamber drift cell from space charge build-up

system which monitored the postion of the 6 KeV peak of Fe^{55} sources mounted directly on the inner walls of 23 of the 144 total chambers. The mechanics and read-out electronics of this system is described more fully in Appendix A. A charged particle passing thus through a total of 6 drift planes (3 coordinate and 3 ambiguity) had to leave hits on at least 5 of 6 possible wires for the track to reconstruct offline. No requirement on pad signals was made for track reconstruction. The average position resolution of the chambers was 650 microns. To save on electronics, consecutive chambers were wire-or'ed together in groups of three to form octants covering 45 degrees in azimuth each. The 8 octants in each plane were numbered 0 - 7. The system relied on the scintillators and cathode pads for finer ϕ segmentation. Signals from the wires on individual chambers entered a pre-amp with x 40 amplification, and then traveled to another amplifier/discriminator board attached to the same frame on which the chambers were mounted. It was at this point that the wire signals were OR'ed into octants. From here, the wire hits from each octant were shipped to TDC's (Time-to-Digital Converters) in the counting room above the collision hall. Each TDC received the hits from 1 chamber octant. There were 48 TDC's total in the system; 1 per octant, with 8 octants per chamber plane and 6 chamber planes (3 east, 3 west) in the whole FMU detector. Then, pattern recognition for the FMU trigger was done, and the hit information sent to the data acquisition computer where it was written to tape. The forward muon read-out electronics are described in detail in [5].

1.2.6.5 The Scintillation Counters

The scintillators were 15° wedges of 13 mm thick acrylic with 10% Napthalene-doping. There were 2 planes of scintillator on each of the east and west ends of the detector. The planes were placed just behind the front plane of drift chambers and just in front of the rear drift plane. Three clear acrylic light pipes on the large end (refer back to figure 1.10) coupled to Amperex 2202B phototubes. There was one light pipe and tube on the small ends of the wedges. The tubes were shielded from magnetic fields by 2 μ metal layers inside a 1 cm thick iron cylinder. Each tube base contained a schmitt trigger circuit which gave an ECL pulse when a counter was struck by a particle which resulted in an anode pulse greater than a 10 mV threshold. The outputs of the 4 tubes on each counter were OR'ed at the detector and sent upstairs to the counting room, where further electronics made the decision as to whether the counter signals are in-time with respect to the beam crossing time or are 'out-of-time hits', (i.e. the counters fired on beam-halo).

1.2.6.6 The Trigger

With beam crossings coming every 3.5 μsec, and an interaction rate of 4400 hz (at $\mathcal{L} = 10^{29}$) , the CDF detector could only measure a sample of the $\bar{p}p$ annihilations actually taking place. To select the events with the most interesting physics, CDF used a four level trigger system. The lowest level trigger, Level 0 (minimum bias), used only the beam-beam counters (mentioned earlier). Level 0 required

only that one counter in each of the BBC planes fire (i.e. one east hit, one west hit) within a 15 ns time window centered on the beam-crossing time. Once Level 0 fired, data-taking was inhibited for $7\mu sec$ (i.e. one beam-crossing was 'skipped' by the detector), while the higher level triggers decided whether the collision is an interesting one. The level 1 CMU trigger used prompt hits from the central muon TDC's to identify tracks in the CMU chambers passing a particular pt threshold. The level 1 trigger cut on the time difference $t_4 - t_2$ and $t_3 - t_1$ between hits on the wires in a muon tower as shown in figure 1.9. This was effectively a P_t cut, since it specifies the maximum allowed angle of a track with respect to an infinite P_t track originating at the event vertex. However, because momentum resolution in the CMU chambers is so dominated by multiple scattering, it was possible for a track with initial P_t satisfying the level 1 threshold to scatter down to a lower P_t, and fail the cut. During the 1988-1989 run, data was taken with the level 1 P_t threshold at 5 GeV/c for the first third of the run, and at 3 GeV/c for the remainder of the run. Cosmic ray studies showed that the CMU level 1 trigger was 93% efficient for tracks with $P_t > 15$ GeV/c, and independent of P_t [7]. The CMU level 2 trigger actually relied upon the Central Fast Tracker (CFT) for its effectiveness. This device was a hardware track processor which used fast timing from the CTC to find high P_t tracks. The CFT looked for 'prompt hits' on only the axial sense wires in the CTC. These were hits with small drift times ($< 80ns$), as were usually found with high P_t tracks. It found the tracks by comparing the pattern of prompt hits found to predetermined hit patterns for a range of P_t bins

extending from 2.5 to 15 GeV/c. The CFT required an average of $2.5\mu sec$ per event to find all high P_t tracks in the CTC. Its momentum resolution was 3.5%, and the efficiency for finding tracks above 9 GeV/c (the level 2 threshold for my analysis) was 98%, independent of P_t [8]. The CMU level 2 trigger took the list of high P_t tracks from the CFT, decided where in ϕ these tracks pointed, and then looked at these positions for hits in the CMU chambers. The device which did the matching was called the Muon Matchbox. The only requirement for a CMU level 2 trigger for this run was that the event had a match between a CMU stub and a CFT track with $P_t > 9$ GeV. The efficiency of CMU level 2 is plotted in figure 1.16. The CMU level 3 trigger took the tracks passing level 2, and did a fast, 2-dimensional reconstruction on them to get their P_t and ϕ. If the event had no reconstructed track with $P_t > 11$ GeV/c, it is rejected. Otherwise, level 3 went back over the level 1 stubs, and looked for the highest P_t track matching each stub. The matching was done in the x-y plane within a window of 10.5 cm about the hit wires. The track found within that window had to have $P_t > 11$ GeV/c, or it was rejected by Level 3. figure 1.17 shows the efficiency of the CMU level 3 trigger as a function of P_t.

1.2.6.7 The Forward Muon Trigger and Momentum Resolution

1.2.6.8 The FMU Level 1 Trigger

Two level one forward muon triggers were used during the 1988-89 data run. Both triggers required the track to have 6 hits. The first trigger employed pattern-

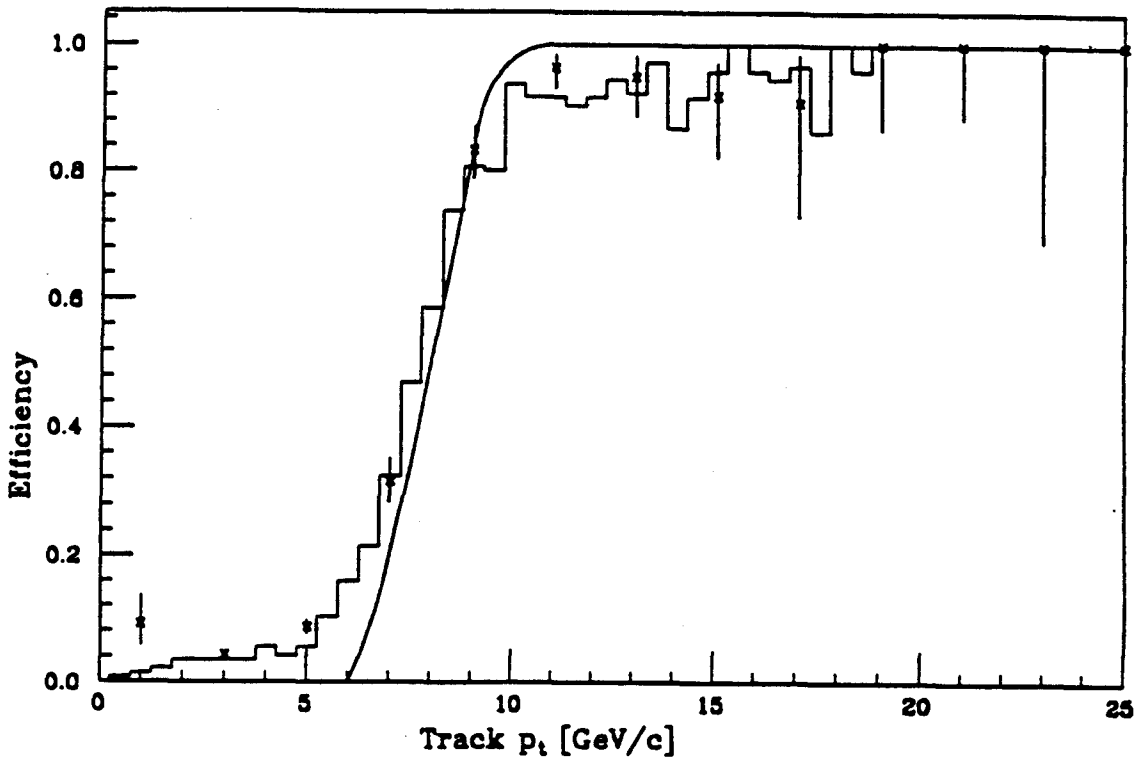

Figure 1.16: Efficiency of the Central Muon Level 2 Trigger as a function of Tranverse Momentum

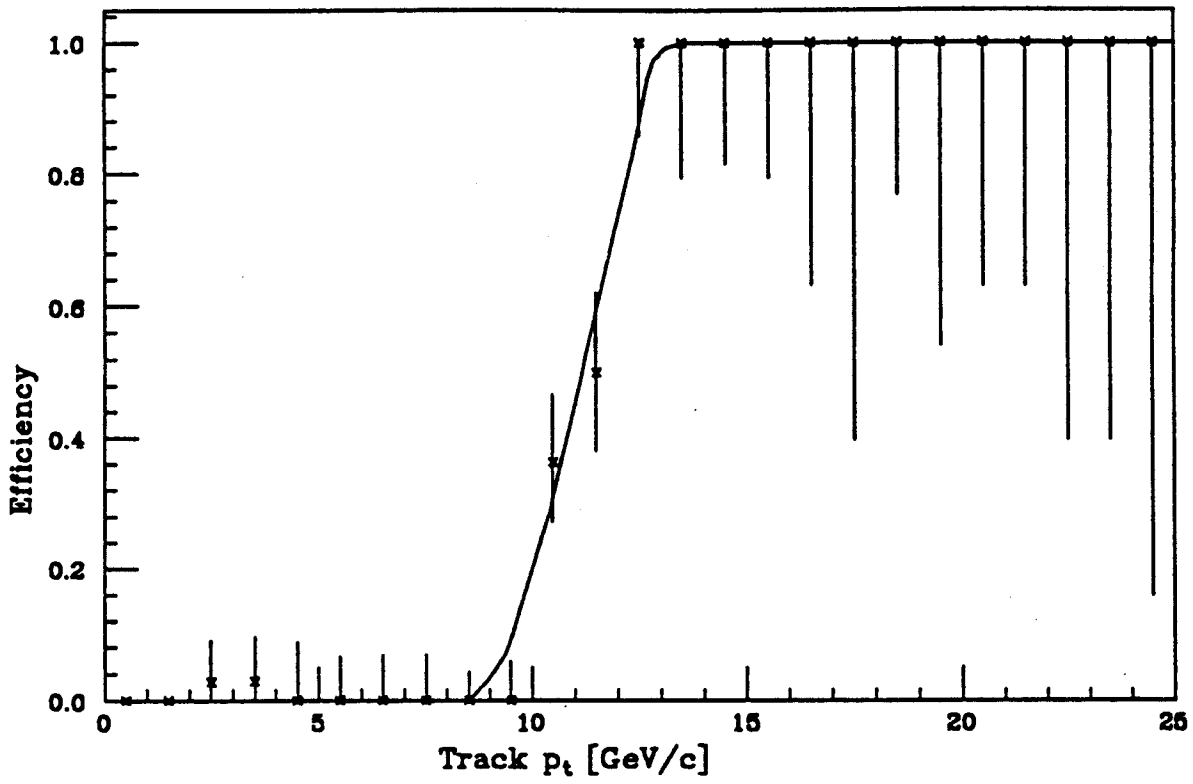

Figure 1.17: Efficiency of the Central Muon Level 3 Trigger as a function of Tranverse Momentum

recognition electronics in the data-readout called HOPU's (Half-Octant Pattern Units). Two HOPU boards took the wire pulses coming from the three TDC's associated with the front, middle, and rear plane chambers of a particular phi octant, and searched for a coincidence of three hits in the front, middle, and rear chambers within a specified road, consistent with a track originating from the vertex. One of the HOPU boards searched coordinate wires 28-55 of the octant for coincidences, while the other searched ambiguity wires 67-95. The inner wires in the chambers (coordinate 0- 27 and ambiguity 56-66) were not used in the trigger. The three possible track roads (corresponding to increasing thresholds of transverse momentum) for which the HOPU's were designed to search were

- the 300%, where the track left a hit on wire n in the front plane, and on wire n or $n \pm 1$ in each of the middle and rear planes.
- the 100%, where the track left a hit on the n^{th} wire in each of the front, middle, and rear planes.
- the 50%, where the track left a hit on the n^{th} wire in all three planes with a drift time less than or equal to a specified time window which is less than the maximum drift time of the cell. This option effectively reduced the active volume of each drift cell.

This trigger required that there be a 3-hit coordinate and a 3-hit ambiguity coincidence on the same end of the detector, though not necessarily within the same octant. It also required that there be be a pair of front and rear plane counter

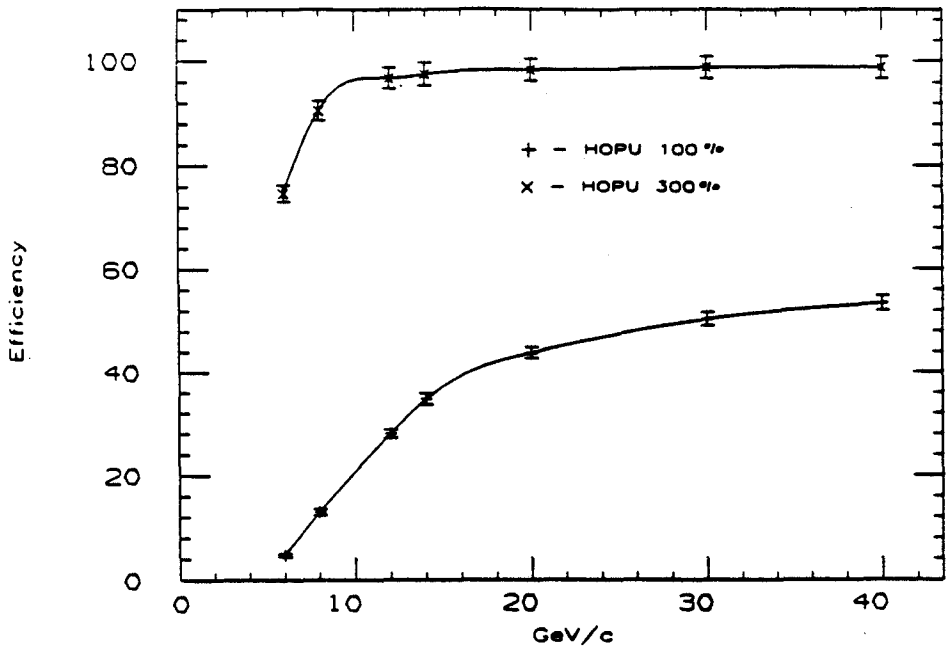

Figure 1.18: Trigger Efficiency for the Level 1 HOPU trigger showing the 300%, and 100% thresholds.

hits in in either the octant of the coordinate coincidence or of the ambiguity. For the portion of the run for which the HOPU level 1 trigger was used (June-Dec. 1988), the 100% road was selected. About 20% of the FMU triggered data was taken with the HOPU level 1 trigger. A plot of the trigger efficiencies of the HOPU trigger roads made from Monte Carlo data is shown in Figure 1.18. There were 32 HOPU boards in the FMU system (two for each octant in the detector). Once a coincidence was found, this information was sent to a Scintillator Hodoscope and Muon Pattern Unit (SHAMPU). There were two SHAMPU

units, one for each end of the detector, east and west. First, each SHAMPU read in hit information from the scintillators and formed coincidences, octant by octant, between the front and rear counter planes on that end. Next, it read wire coincidence information from the HOPU's, and decided if there was at least 1 coordinate and at least one ambiguity coincidence. If there was, the SHAMPU sent the scintillator match information back to all the HOPU's on its side, and each HOPU performed a logical AND of the counter match information with its wire coincidence, if they had one. This way, it was ensured that the counter match would be in the same octant as at least one of the coordinate or ambiguity coincidences, though there was no requirement that the coordinate and ambiguity coincidences themselves lay in the same octant. From the HOPU, the trigger information was sent up to level 3 (FMU used a two-tiered trigger scheme for the 1988-89 run. The level 2 stage was by-passed, and level 1 information sent directly to level 3). The HOPU level 1 trigger was used from June to December of 1988. After this the HOPU boards were replaced by 'NUPU' boards (New Pattern Units). The essential advantage of the NUPU trigger over the HOPU was that in the NUPU boards, the coordinant and amibguity coincidences were required to lay inside the same octant. The requirement of a scintillator coincidence was dropped. Also, the NUPU's operated with a 50% trigger road. A plot of the NUPU trigger efficiencies using monte data is shown in Figure 1.19.

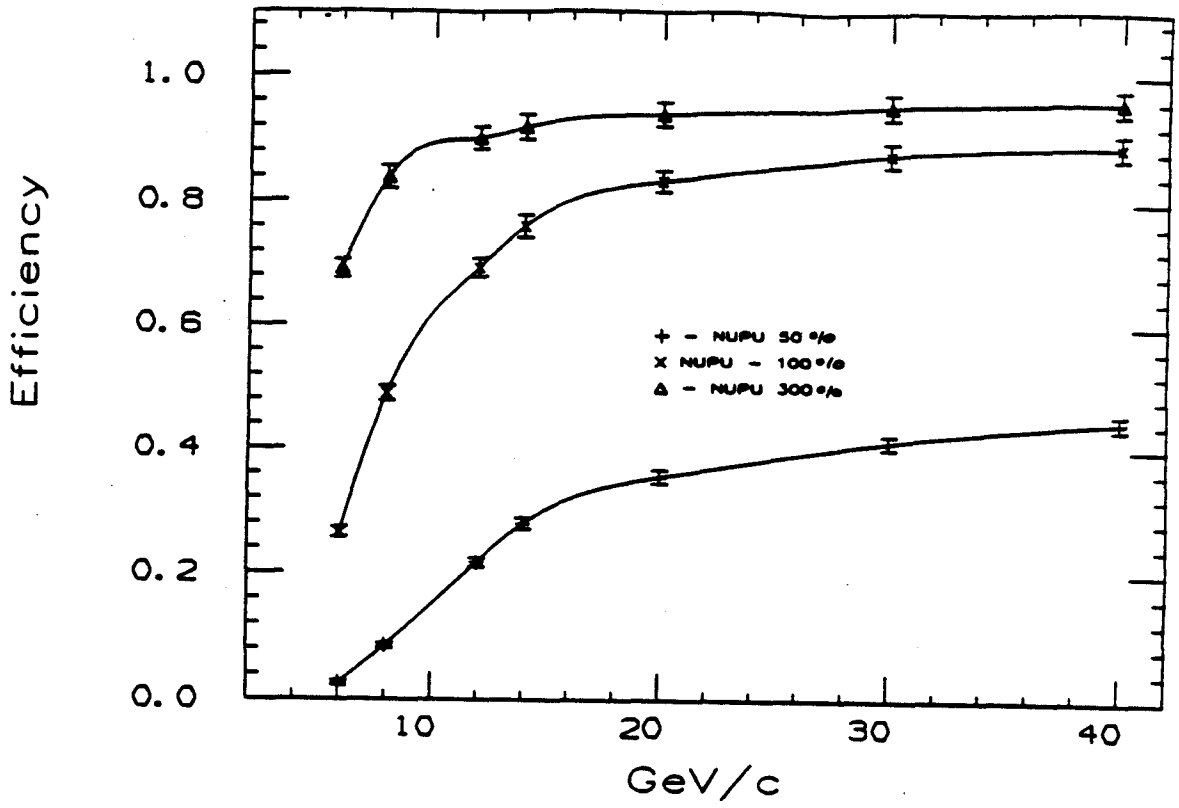

Figure 1.19: Trigger Efficiency versus P_t of the Level 1 NUPU trigger showing the 300%, 100%, and 50% thresholds.

1.2.6.9 The FMU Level 3 Trigger

Level 1 trigger information was shipped from the HOPU's to the muon matchbox. The muon matchbox was a device capable of OR'ing Forward muons with other phenomena in the detector to form triggers such as FMUO+jet(s), or FMUO+CMUO, for instance. This capability was never implemented for the 1988-89 run. Instead, the level 1 triggered FMUO's passed directly to the level 3 trigger reconstruction. The requirement here was only that the FMUO reconstruct within the 100% trigger road. Events used in this analysis were not required to satisfy either the forward muon level 1 or level 3 trigger. More detailed information on the workings of the forward muon triggers during the 1988-1989 run is available in [5].

1.2.6.10 FMU Resolution

The momentum resolution of the forward muon system is made up of four components:

- Chamber position resolution
- Multiple scattering in the iron of the toroids.
- The effects of survey errors.
- The effects of multiple hits in the forward muon chambers.

The second component of the resolution, multiple scattering, was essentially independent of the particle momentum, for the momentum range of interest in this analysis [3]. The other components, however, are momentum-dependent effects. The calculation of the contribution from multiple scattering has already been presented in detail in [4]. Briefly, the momentum resolution from multiple scattering from these effects was a function of the polar angle, α, of the track as it entered the first layer of FMU drift chambers and the bend displacement, ϵ, in the polar direction which the track underwent as it traveled through the FMU system. ϵ is itself dependent on the magnetic field in the toroids, the entrance angle α, and the momentum, p. To lowest order in momentum,

$$\epsilon = \frac{0.3qBl^2}{2p}\{4 + \frac{2(d+2t)}{l} + \alpha^2(3 + \frac{d+2t}{l})\} \tag{1.13}$$

where $l = 100cm$, the thickness of the toroids, $d = 52cm$, the separation of the toroids, $t = 42cm$, the spacing between the toroids and the front (and rear) chamber planes, α = the polar angle of the track in radians at the entrance to the front plane, q = electric charge, p = track momentum, and B is the magnetic field at the radius of the track. The mean displacement in the y direction due to multiple scattering [3] undergone by a particle passing through the entire detector is given by $\delta y = \delta\epsilon$, where

$$\delta\epsilon = \frac{30.7cm}{P} \tag{1.14}$$

Using this relation in equation 1.13, and also that

$$\frac{\delta P}{P} = \frac{\delta\epsilon}{\epsilon} \tag{1.15}$$

one arrives at the equation for the resolution of the FMU chambers taking only multiple scattering into account:

$$\frac{\delta P}{P} = \frac{0.02}{B}\{4.36\alpha^2 + 6.72\}^{-1} \tag{1.16}$$

where the polar angle α is in radians, and the magnetic field in Tesla. The resolution varies from 14.9% at the inner radius where $B = 2.0$ Tesla to 17.7% at the outer radius, where $B = 1.6$T. The effect of α^2 was small compared to that of the field, and the resolution was independent of momentum above $5GeV/c$. For a typical track at $\alpha = 10°$, the resolution was calculated to be

$$\frac{\Delta P}{P} = 16.6\% \tag{1.17}$$

1.2.6.11 The Contribution of Survey Errors

At a momentum > 200 GeV/c^2, the survey errors become significant. A study of the misalignment of the chambers [6] indicates that the error on the surveyed chamber positions is $0.5mm$ for the x-y positions, and 3 mm for the z position. The effects of this error on the momentum resolution were simulated in a Monte Carlo calculation by smearing the positions of the track hits by amounts comparable to the survey errors. Survey errors were estimated to have the following contributions to the momentum resolution:

- xy survey error $= 0.00093 \cdot P$
- z survey error $= 0.00083 \cdot P$

- error on drift time measurement $= 0.00084 \cdot P$

Adding these in quadrature with the multiple scattering/chamber resolution contribution gives for the FMU momentum resolution

$$\frac{\Delta P}{P} = \sqrt{0.166^2 + (.00093^2 + .00083^2 + .00084^2) \cdot P^2} \qquad (1.18)$$

using the nominal value of 16.6% for the multiple scattering/chamber design resolution contribution.. A plot of the forward muon momentum resolution is shown in figure 1.20

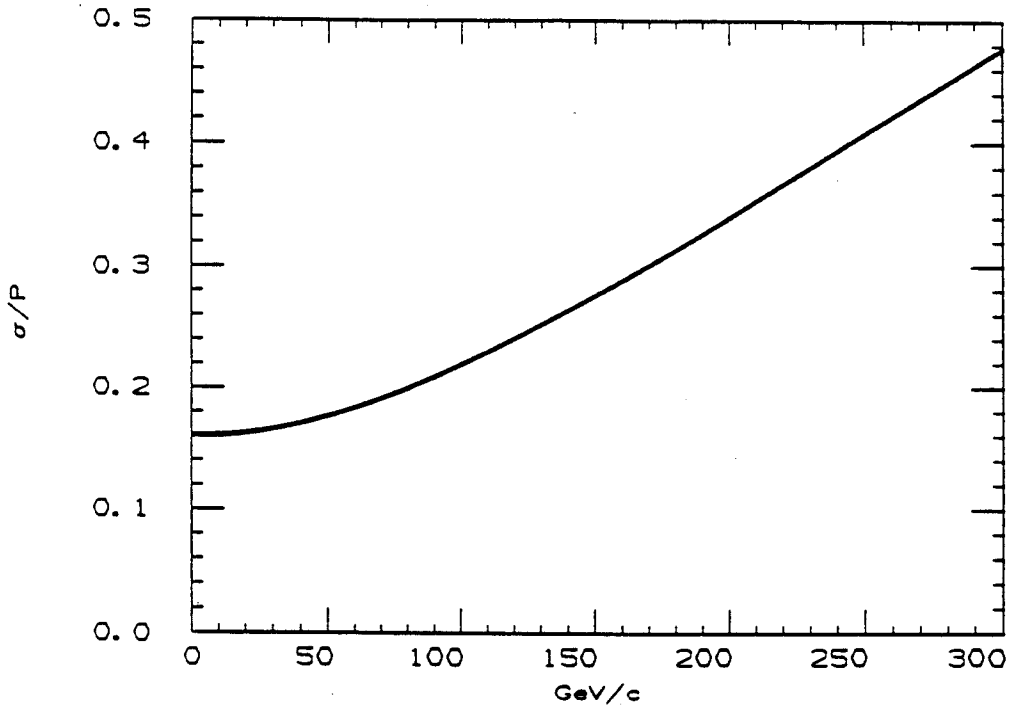

Figure 1.20: Resolution of the Forward Muon Drift Chambers as a function of track momentum

Chapter 2

Theory

2.1 Fundamental Forces and the Quark Model

Particle physics is the science which studies the fundamental constituents of matter and the forces which govern their interactions. The smallest subdivisions of matter currently known are the quarks and leptons. There are 6 types, or flavors, of quarks and three generations of leptons, the latter each having an accompanying neutrino. The quarks are the up, down, charm, strange, top, and bottom. Only top has not been verified experimentally. The three types of leptons are the electron, the muon, and the tau. Quarks and leptons have half integral spin, and for this reason are called Fermions. Particles with integral spin are called Bosons. The quarks and leptons can each be grouped into three generations of doublets based on the direction of their spin polarization, or helicity:

$$\begin{pmatrix} u_L \\ d_L \end{pmatrix} \begin{pmatrix} c_L \\ s_L \end{pmatrix} \begin{pmatrix} t_L \\ b_L \end{pmatrix}$$

$$\begin{pmatrix} \nu_{e_L} \\ e_L \end{pmatrix} \begin{pmatrix} \nu_{\mu_L} \\ \mu_L \end{pmatrix} \begin{pmatrix} \nu_{\tau_L} \\ \tau_L \end{pmatrix}$$

where the subscript L denotes the helicity of the particle as having left-handed polarization, (i.e. its internal spin direction is in the opposite sense to that of its motion). The right-handed quarks and leptons form singlets:

$$u_R, c_R, t_R, d_R, s_R, b_R, e_R, \mu_R, \tau_R$$

There are no right-handed neutrinos or left handed anti-neutrinos in the theory, and none have been observed in nature thus far.

2.1.1 Fundamental Forces

The four fundamental forces, or interactions, responsible for all known physical phenomena in the universe are the strong, weak, electromagnetic, and gravitational. In particle field theory, a force is described as being transmitted via mediating particles with integral spin called gauge bosons. The gauge particle for the strong force is the gluon, a massless, spin 1 particle so called because it binds, or 'glues', the quarks together to form nucleons (protons and neutrons), and the nucleons together to form nuclei. The weak force controls the processes by which one type or 'flavor' of lepton or quark can change into another type. The weak force has three massive gauge bosons, the W^+, W^-, and the neutral Z^0. The W and Z bosons were first observed experimentally at the CERN $\bar{p}p$ collider in the early 1980's. The mediating particle for the electromagnetic force

Fundamental Forces		
Force	Range	Gauge Boson
Strong	$\leq 10^{-15}$ m	Gluon
Weak	10^{-18} m	Z^0,$W^{\pm}$
Electromagnetic	∞	γ
Gravitational	∞	Graviton

Table 2.1: The four fundamental forces of physics, their ranges, gauge bosons.

is the photon, which is massless and has spin = 1. The last of the fundamental forces, gravity, is important only on a macroscopic level, and hence is not relevant to the physics described in this thesis. It is predicted to have a spin 2, massless mediating boson, called the graviton, but the existence of this gauge particle has not been experimentally verified. Table 2.1 lists the four forces, their ranges, and properties of their gauge particles. The leptons and W, Z bosons have no strong interactions, only weak and electromagnetic. Particles made up of various combinations of quarks, and hence which interact strongly, are collectively called hadrons. Hadrons are divided into two categories, baryons and mesons. Baryons are bound states of 3 quarks, and hence have half integral spin, making them fermions. Mesons consist of quark and anti-quark pairs. Thus, they have integral spin and are bosons. The quantum numbers of the quarks and leptons are baryon number ($= \frac{1}{3}$ for all the quarks,$\frac{-1}{3}$ for anti-quarks), lepton number (= 1

for the leptons, -1 for anti-leptons), charm, strangeness, topness, bottomness, electric charge, and the z-component of isospin. All of these quantum numbers are conserved absolutely for the strong interaction. The electromagnetic interaction does not conserve isospin absolutely, and the weak interaction conserves only electromagnetic charge, and lepton and baryon number. The concept of isospin was introduced when it was noticed that nuclear (strong) interactions appeared to treat the proton and neutron in virtually identical ways. This suggested a further degree of freedom existed, to which the strong force was blind, and hence, another conserved quantum number. This was termed isospin, with value $\frac{1}{2}$, and two substates in which the third component, I_3 , was equal to $\frac{+1}{2}$ for the proton and $\frac{-1}{2}$ for the neutron. The model of Gell-Mann–Nishijima relates electromagnetic charge, isospin, baryon number, and strangeness according to the formula

$$Q = I_3 + \frac{Y}{2} \tag{2.1}$$

where the quantity Y is defined as equal $B + S$ (baryon number+strangeness) is called 'hypercharge'.

2.1.2 Interaction Currents and the Electroweak Lagrangian

One can consider the action of a force between interacting particles via boson exchange also as the transmission of a charged or neutral 'current' between the particles. The photon couples to the electromagnetic current; the W^+ and W^- are responsible for the 'charged current'-type of weak interaction, in which one

member of a doublet is transformed into the other member, and also for interactions where mixing between generations occur (flavor-changing currents). The Z^0 is responsible for the 'neutral current' weak interactions in which singlets and the upper and lower members of doublets can be transformed into themselves (and thus preserving flavor). The relative strengths of the electromagnetic, weak, and strong interactions are described in terms of the coupling constants. The gauge boson for a force is said to 'couple' to the fields of the interacting particles with amplitude equal to the coupling constant for the particular type of interaction. The photon for the electromagnetic force couples to the electric charge; for the strong interaction, gluons couple to the color charge, and the $W^{\pm}$ and Z^0 bosons couple to weak isospin and weak hypercharge. Experimental data from deep-inelastic neutrino scattering experiments show that the weak current couples only to left-handed particles and right-handed anti-particles. The weak interaction is thus said to be vector–axial vector. Using the notation of the Dirac γ matrices, the weak interaction current is written

$$J^{\mu}_{weak} = \bar{\psi}\gamma^{\mu}\frac{1}{2}(1-\gamma^5)\psi \tag{2.2}$$

and the electromagnetic as

$$J^{\mu}_{em} = -e\bar{\psi}\gamma^{\mu}\psi \tag{2.3}$$

Where e is the electromagnetic charge. The vector–axial nature of the weak current comes from the $1-\gamma^5$ factor, which automatically selects the left handed particles and right handed anti-particles.

2.1.3 Color

The quark model was a great success in accounting for the observed separation of hadrons into particles of integral and half integral spin. However, experiment also observed baryons like the Δ^{++}, a bound state of three up quarks all with spin $\frac{+1}{2}$, apparently violating the quantum mechanical principle that identical fermions cannot occupy the same quantum mechanical state. To resolve this problem, a new degree of freedom, or quantum number, designated color, had to be postulated. The theory of color interactions, which are strong interactions is called Quantum Chromodynamics (QCD). Quarks are said to come in three possible colors, red, blue, and green, and the anti-quarks in complementary anti-red, anti-blue, and anti-green. Color is considered to be a hidden quantum number, i.e. all particles observed in nature are asserted to be color-less, i.e. the different colors cancel each other out, as does color with anti-color. Thus, baryons contain a red, a green, and a blue quark, while mesons and gluons consist of a color plus anti- color pair. Otherwise, there would exist many different color states of the same particle, and this is not observed by experiment. Moreover, attempts to observe colored particle states by splitting 1 quark off from a meson or baryon fail. The potential energy required to separate a pair of quarks goes as r for distances greater than about 1 Fermi (1 Fermi = 10^{-15} m). Injecting energy into the systems simply causes the original hadron to fragment into showers or jets of colorless hadrons. See figure 2.1 [13].

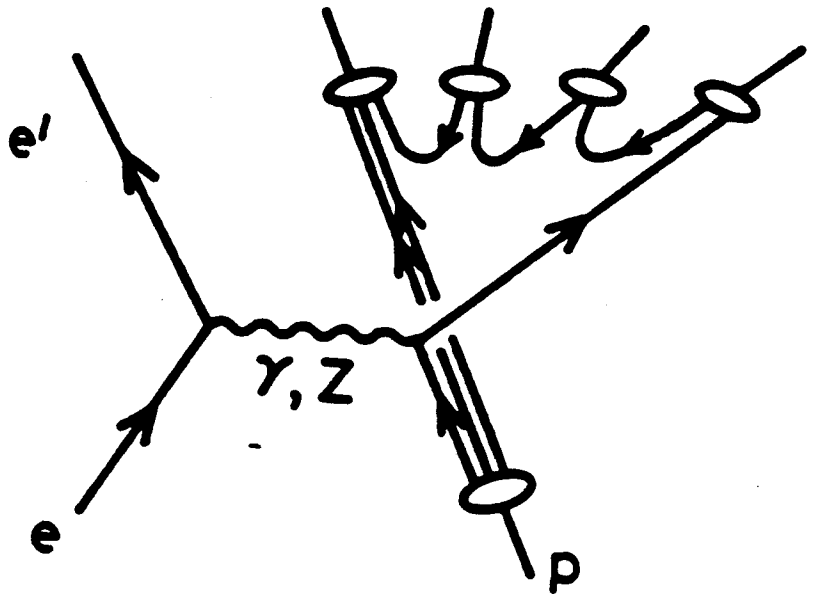

Figure 2.1: Hadronization of quarks in a proton by the color force field in *ep* inelastic scattering.

Quarks are thus said to obey 'color confinement'. Models of confinement attribute this property of quarks to polarization of the QCD vacuum as the quarks in a bound state are pulled apart. As the bound quarks are separated, $q\bar{q}$ pairs appear from the vacuum. The coupling constant for the strong interaction, α_s, is a function of the momentum transfer in the interaction, q^2, and is hence described as a 'running' coupling. α_s has the form

$$\alpha_s = \frac{1}{B \cdot \ln(q^2/\Lambda^2)} \tag{2.4}$$

where B is given in terms of the number of quark flavors, f, as

$$B = (33 - 2 \cdot f)/12\pi \tag{2.5}$$

and Λ is the QCD scale parameter determined by experiment. This equation shows that as $q^2 \longrightarrow \Lambda^2$, the strong coupling constant $\alpha_s \longrightarrow \infty$, implying quark confinement, and also that as $q^2 \longrightarrow \infty$, $\alpha_s \longrightarrow 0$, a condition known as 'asymptotic freedom' (i.e. at small r the quarks behave as if free).

2.1.4 The Standard Model of Weak and Electromagnetic Interactions

The standard model of electroweak and strong interactions [9] is based on the combined symmetry groups SU(3) x SU(2) x U(1). U(1) is the group of unitary, Abelian transformations in 1 dimension (1 x 1 unitary matrices) which have the form of a simple phase change:

$$U(\alpha) = e^{i\alpha} \tag{2.6}$$

where α varies freely over all real numbers. 'Abelian' means that sucessive transformations commute. The field theory of the electromagnetic interactions is called quantum electrodynamics (QED), and its actions are described by the U(1) group. The transformations of this group are 'gauge invariant'. Here, invariance implies that the physics of the interaction does not change under the transformations of the group. The term 'gauge' refers to an initial condition placed on the field mediating the interaction. Selecting such a condition is called selecting a 'gauge', and the mediating field is called a 'gauge field'. In QED, the gauge field $A^\mu = (V, \mathbf{A})$, is chosen so that

$$\partial_\mu A^\mu = 0 \tag{2.7}$$

and the gauge transformations are of the form

$$A^\mu \longrightarrow A'^\mu = A^\mu + \partial^\mu \alpha \tag{2.8}$$

The local gauge invariance of QED has two direct consequences: (1) the quantum of the gauge field A, the photon, is massless. Masslessness of the mediating particles is true for all gauge invariant theories. The introduction of terms to the Lagrangian describing the interactions between the gauge field and the initial and final state particles does not result in mass terms for the gauge particles. (2) the current of the electromagnetic interaction is conserved, implying that the observable, electric charge is also conserved. In general, every type of symmetry transformation which leaves the Lagrangian invariant also leads to a law governing the conservation of an observable. SU(2) is the symmetry group of unitary

transformations consisting of 2 x 2 matrices with determinant equal to unity, and which describe the weak interaction. Its fundamental representation is the isospin doublet. Gauge invariance of the Lagrangian for this interaction leads to the introduction of a triplet of massless gauge fields, W^0, W^1, and W^2. The strong interaction is described by the symmetry group SU(3) of transformations in three dimensions (since each quark can be any of three colors). Local gauge invariance requires 8 massless bosons called gluons. Since the physics covered by this thesis involves electromagnetic and weak (electroweak) interactions, I will not delve further into this area of the Standard Model. Electroweak interactions are governed by the combined group of local gauge symmetries SU(2) x U(1). SU(2) of the weak interaction is usually written as $SU(2)_L$, to denote its left handed nature. The gauge bosons of the unified group are the massless W^1, W^2, and W^3 of SU(2), plus a massless boson B from the U(1) group. The charged weak interaction is mediated by linear combinations of the the W^1 and W^2:

$$W_\mu^\pm = \frac{1}{\sqrt{2}}(W_{1\mu} \pm iW_{2\mu}) \tag{2.9}$$

while the photon and Z^0 fields which mediate the electromagnetic and weak neutral current interactions are linear combinations of W^3 and B:

$$\begin{pmatrix} W_3 \\ B \end{pmatrix} = \begin{pmatrix} \cos\theta_W & \sin\theta_W \\ -\sin\theta_W & \cos\theta_W \end{pmatrix} \begin{pmatrix} Z \\ A \end{pmatrix}$$

[11] where θ_W is the electroweak weak mixing angle, a parameter of the Standard Model which must be determined by experiment. In this theory, intermediate

bosons are all massless, however, the short range of the weak force found by experiment requires massive gauge particles. This difficulty was resolved by the introduction of a doublet of Higgs scalar fields, which spontaneously break the symmetry of SU(2)×U(1) to U(1) giving mass to the W^+, W^-, Z^0, leaving the photon massless. The masses of the bosons are determined by the coupling constants g, and g', for weak isospin and weak hypercharge, respectively, and v, the vacuum expectation value of the Higgs field, Φ. The coupling constants are related by θ_W

$$g = \frac{e}{sin\theta_W} \tag{2.10}$$

$$g' = \frac{e}{cos\theta_W} \tag{2.11}$$

[12], and the boson masses are given by:

$$\begin{aligned} M_W &= \frac{g \cdot v}{2} \\ M_Z &= \frac{M_W}{\cos\theta_W} \end{aligned} \tag{2.12}$$

To first order in the couplings, the Lagrangian for the electroweak interaction can be written

$$\mathcal{L} = -\mathrm{g}\mathbf{J}_\mu \cdot \mathbf{W}_\mu - \frac{1}{2}\mathrm{g}'\mathrm{J}^{\mathrm{Y}}_\mu \mathrm{B}_\mu \tag{2.13}$$

where J^μ and $(J^Y)^\mu$ are the isospin and hypercharge currents of the fermions. Referring to the Gell-Mann–Nishijima formula of equation 2.1, the weak hypercharge current can be written in the form

$$J^Y_\mu = 2 \cdot (J^{em}_\mu - J^3_\mu) \tag{2.14}$$

where J_μ^{em} is the electromagnetic current, and J_μ^3 is the 3rd component of the isospin current. Using the forms for the fields above, we can group the terms of the Langrangian into electromagnetic, weak neutral current, and weak charged-current contributions.

$$\begin{aligned}\mathcal{L} &= \frac{g}{\sqrt{2}}(J_\mu^+ W_\mu^+ + J_\mu^- W_\mu^-) + \frac{g}{cos\theta_W}(J_\mu^3 - sin^2\theta_w J_\mu^{em})Z_\mu \\ &\quad + g sin\theta_W J_\mu^{em} A_\mu \end{aligned} \tag{2.15}$$

where the first term is from the weak charged current interaction, the second term from the weak neutral current interaction, and the last from the electromagnetic interaction.

2.1.5 Angular Asymmetries and the Standard Model

In hadronic collisions, intermediate vector bosons (W^+, W^-, Z^0, or virtual photons) are produced when $q\bar{q}$ pairs contained within the hadrons annihilate. In the case of neutral currents, the Z^0 or virtual γ may then decay via the Drell-Yan process to charged lepton pairs. The lowest order diagrams for this process are shown in figure 2.2. It is the vector minus axial vector nature of the weak current which leads to parity violating interactions and to the angular asymmetries observed in weak boson decays. The Z^0 current, as it appears in equation 2.15, has weak and electromagnetic components:

$$J_\mu^Z = J_\mu^3 - sin^2\theta_W J_\mu^{em} \tag{2.16}$$

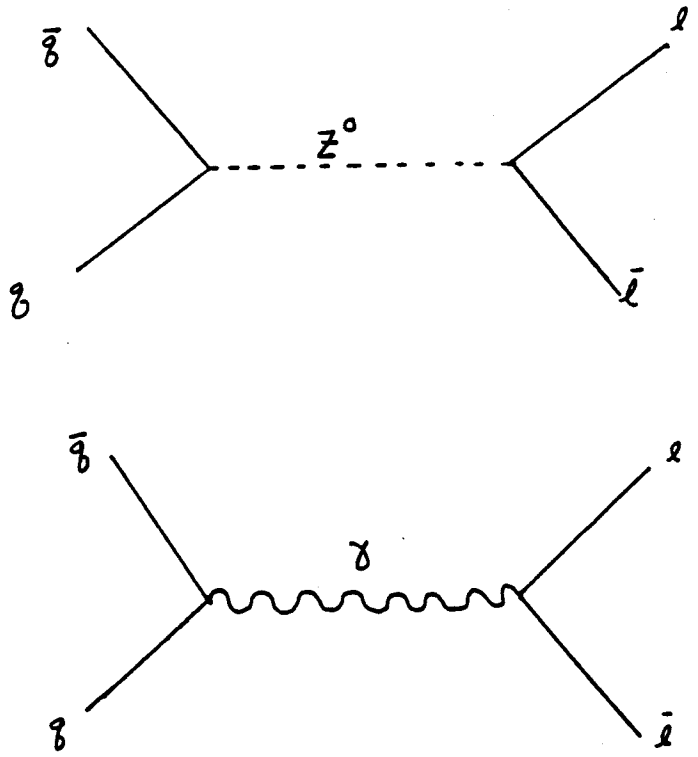

Figure 2.2: Feynman diagrams of the lowest order processes in the dilepton pair production cross-section.

Inserting the forms for the weak and electromagnetic currents, we have

$$J_\mu^Z = \gamma_\mu[\frac{1}{2}(1-\gamma^5)I^3 - sin^2\theta_W Q] \tag{2.17}$$

The $\gamma_\mu[\frac{1}{2}(1-\gamma^5)I^3$ term describes the weak neutral current, which, being left-handed, couples to left-handed fermions, and right-handed anti-fermions. The weak current component of the Z^0 current thus establishes a preferred direction for the particles spins. Also, conservation of angular momentum requires that the spin of the Z^0 be aligned with those of the quarks, and that the spins of the outgoing leptons be aligned with that of the Z^0. This means that the negative lepton preferentially travels along the same direction as the incoming quark. The result is a measurable asymmetry in the angular distribution of the decay products of the Z^0. However, it is a preferred, rather than a required direction, since the Z^0 current, unlike the weak charged current of the $W^\pm$, also has an electromagnetic term, $-sin^2\theta_W\gamma_\mu Q$. The electromagnetic current is parity-conserving, and thus this term modifies the parity-violating effect of the weak current, and the resulting asymmetry is not as great as in the case of W decay (in which parity is violated maximally). This thesis investigates the forward-backward asymmetry present in the process $q\bar{q} \longrightarrow Z^0 \longrightarrow \mu^+\mu^-$. 'Forward' refers to the direction of the negative muon when it travels in the $+\hat{z}$ direction, and 'backward' when it travels in the $-\hat{z}$ direction. The magnitude of this asymmetry (i.e. the proportion of parity-violating to parity-conserving contributions in the Z^0 current) is determined by the size of the vector and axial vector couplings in the cross-section, which are

themselves functions of the Weinberg angle, $\sin^2\theta_W$, and the charge and isospin of the fermions. Thus, from a measurement of the forward-backward asymmetry in lepton pair production, one can extract a value for the Weinberg angle, one of the parameters of the Standard Model. The equation for the neutral current interaction in which the Z^0 couples to the fermion fields, Ψ_f, is written as

$$-i\frac{g}{cos\theta_W}\bar{\Psi}_f\gamma^\mu[\frac{1}{2}(1-\gamma^5)I^3 - sin^2\theta_W Q]\Psi_f \tag{2.18}$$

The vertex factor for the interaction can be written in terms of the vector and axial vector couplings of the Z^0 to its decay fermions as

$$-i\frac{g}{cos\theta_W}\gamma^\mu(g_V^f - g_A^f\gamma^5) \tag{2.19}$$

where

$$g_V^f = 2I_3^f - 4Q^f sin^2\theta_W \tag{2.20}$$

and

$$g_A^f = 2I_3^f \tag{2.21}$$

$I^f = +\frac{1}{2}$ for ν_e,ν_μ,ν_τ, u, c, and t, and $= -\frac{1}{2}$ for e^-,μ^-,τ^-, d, s, and b [10]. The differential cross-section for charged lepton pair production, based on the two lowest order diagrams of fig. 2.2, and written in term of the couplings and the angle θ between the negative lepton and the incoming quark is

$$\begin{aligned}\frac{d\sigma}{d\cos\theta} &= \frac{1}{3}\int_0^1 dx_a \int_0^1 dx_b \sum_q q(x_a,\hat{s})\bar{q}(x_b,\hat{s})\left(\frac{\pi\alpha^2}{2\hat{s}}\right)\{Q_q^2Q_l^2(1+\cos^2\theta) \\ &\quad +2Q_qQ_l\mathrm{Re}\chi(\hat{s})[g_V^lg_V^q(1+\cos^2\theta)+2g_A^lg_A^q\cos\theta]\end{aligned}$$

$$+|\chi(\hat{s})|^2[((g_V^l)^2+(g_A^l)^2)((g_V^q)^2+(g_A^q)^2)(1+\cos^2\theta)$$
$$+8g_V^l g_A^l g_V^q g_A^q \cos\theta]\} \qquad (2.22)$$

The angle $\cos\theta$ is defined as the cosine of the angle between the outgoing negative lepton and incoming quark in the rest frame of the lepton pair. The summation in equation 2.22 is over 6 quark flavors, and the factor of 1/3 is a color factor from averaging over the 3 quark colors. $\hat{s}$ is the square of the collision energy in the center of mass frame. $q(x_a,\hat{s})$ and $\bar{q}(x_b,\hat{s})$ are the quark momentum distribution functions in the proton and anti-proton, and x_a and x_b are the momentum fractions carried by the quark and antiquark. Q_q and Q_l are the quark and lepton charges. The Z^0 propagator, χ, is written in terms of $\hat{s}$, and the mass of the Z^0, and its width, Γ_Z, as

$$\chi(\hat{s}) = \frac{1}{16\sin^2\theta_W\cos^2\theta_W}\cdot\frac{\hat{s}((\hat{s}-M_Z^2)-iM_Z\Gamma_Z)}{(\hat{s}-M_Z^2)^2+M_Z^2\Gamma_Z^2} \qquad (2.23)$$

The forward backward asymmetry, A_{fb}, is defined as the number of events with $\cos\theta > 0$ minus the number with $\cos\theta < 0$, divided by the total number of events.

$$A_{fb} = \frac{N_{\cos\theta>0}-N_{\cos\theta<0}}{N_{\cos\theta>0}+N_{\cos\theta<0}} \qquad (2.24)$$

A_{fb} is related to the differential cross-section of eq. 2.22 by

$$A_{fb} = \frac{\int_0^1 \frac{d\sigma}{d\cos\theta}d(\cos\theta)-\int_{-1}^0 \frac{d\sigma}{d\cos\theta}d(\cos\theta)}{\int_{-1}^1 \frac{d\sigma}{d\cos\theta}d(\cos\theta)} \qquad (2.25)$$

The first term in the equation for the cross section, eq. 2.22 is the contribution from photon exchange, the third from Z^0 exchange, and the second from the

interference between the two. Notice that the first term in the cross-section (photon exchange) is symmetric in $\cos\theta$ (i.e. producing no angular asymmetry), while the second and third terms have both symmetric ($\sim \cos^2\theta$) and anti-symmetric ($\sim \cos\theta$) components. Since the interference term vanishes on the Z^0 resonance ($\mathrm{Re}\chi(\hat{s}) = 0$, at $\hat{s} = M_Z^2$), the asymmetric component of this term only contributes to angular aymmetries seen away from the resonance. The asymmetric component of the Z^0 term, which appears on the Z^0 resonance, arises from the interference between the vector and axial vector couplings of the Z to the fermions. See Figure 2.3, which shows the asymmetry as a function of $\sin^2\theta_W$ evaluated at $\hat{s} = M_Z^2$ (i.e. the contribution from Z^0 exchange only vs. $\sin^2\theta_W$). From equation 2.20, one sees that for a value of $\sin^2\theta_W = \frac{1}{4}$, the vector coupling to the leptons, $g_V^l = 0$, and the vector contribution from Z^0 exchange to the cross-section vanishes, and the asymmetry comes only from the $\gamma - Z$ interfence term. Figure 2.4 shows the contribution of the interference term versus the mass of the dilepton, when $\sin^2\theta_W = \frac{1}{4}$. One can use the cross-section formula of equation 2.22 in 2.25 to write A_{fb} explicitly as a function of the parton distribution functions, M_Z, Γ_Z, and the Weinberg angle, θ_W. Because x_a and x_b are not independent variables, it is usual to transform to $\hat{s} - y$ space, where y is the rapidity of the Z^0. x_a and x_b transform as

$$x_a = \sqrt{\frac{\hat{s}}{s}} \cdot e^{-y} \tag{2.26}$$

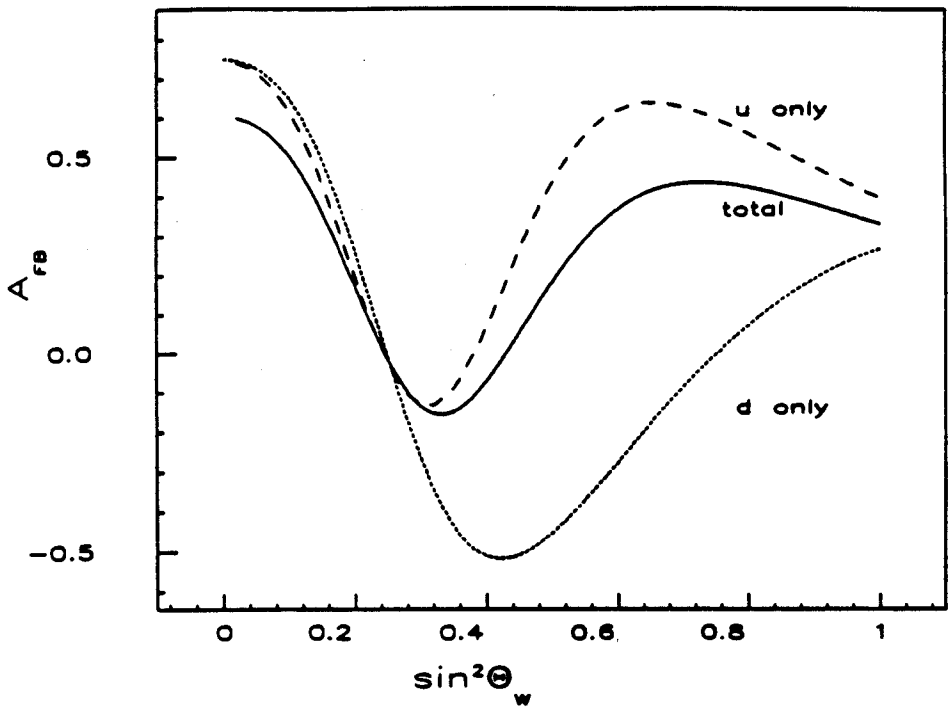

Figure 2.3: The Forward-Backward Asymmetry versus $\sin^2\theta_W$. The individual contributions of the u and d quarks are shown in dashed and dotted lines.

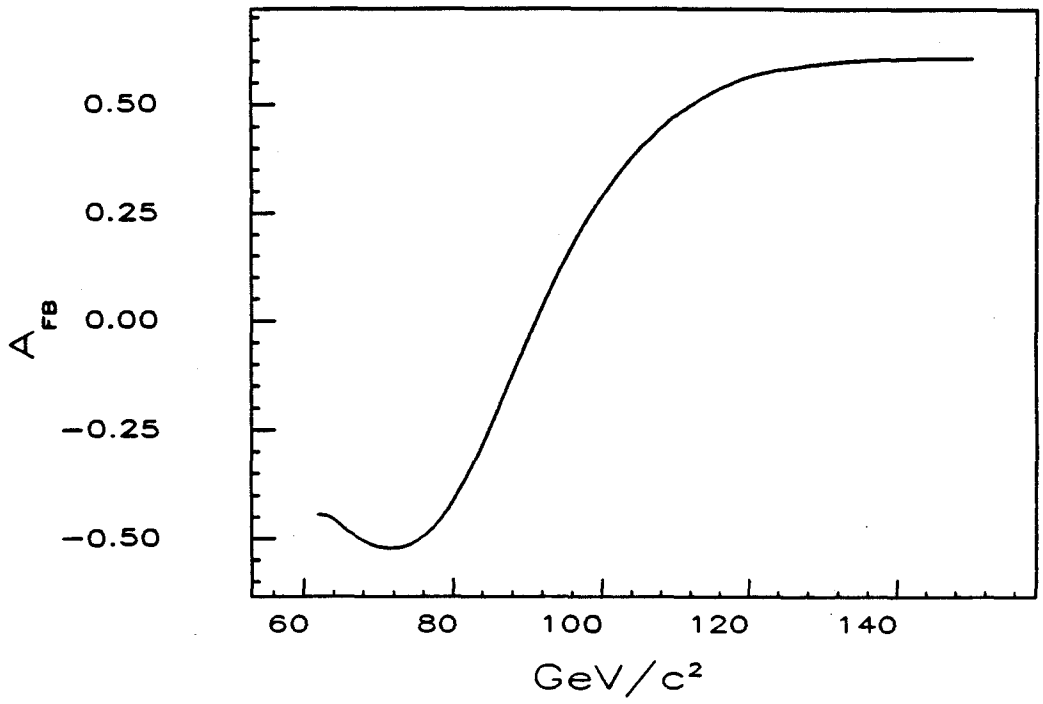

Figure 2.4: The Forward-Backward Asymmetry versus Mass of the dilepton.

and

$$x_b = \sqrt{\frac{\hat{s}}{s}} \cdot e^{y} \tag{2.27}$$

Also,

$$dx_a dx_b = \frac{d\hat{s}dy}{s} \tag{2.28}$$

So, one can substitute $\hat{s}$ and y in for x_a and x_b in 2.22, and then integrate twice: first, over $\hat{s}$ across the Breit-Wigner resonance (assuming the structure functions are essentially constant over the resonance), and second, over $\cos\theta$. Then, eq. 2.25 can be written as

$$A_{fb} = \frac{\int_{-y_0}^{y_0} \sum_q q(x_a, M_Z^2)\bar{q}(x_b, M_Z^2) \cdot 3 g_V^l g_A^l g_V^q g_A^q dy}{\int_{-y_0}^{y_0} \sum_q q(x_a, M_Z^2)\bar{q}(x_b, M_Z^2) \cdot [(g_V^l)^2 + (g_A^l)^2][(g_V^q)^2 + (g_A^q)^2] dy} \tag{2.29}$$

where

$$\pm\, y_0 = \pm \ln\left(\frac{\sqrt{s}}{M_z}\right) \tag{2.30}$$

After substituting in equations 2.20 and 2.21 for the vector and axial couplings in 2.29, and writing the summation explicitly in terms of the u and d valence and sea quark, and the s sea quark structure functions, the numerator of 2.29 becomes

$$\begin{aligned}
& 3\int_{-y_0}^{y_0} dy [u_{val}(x_a, M_Z^2)\bar{u}_{val}(x_b, M_Z^2) + u_{val}(x_a, M_Z^2)\bar{u}_{sea}(x_b, M_Z^2) \\
+ \;& u_{sea}(x_a, M_Z^2)\bar{u}_{val}(x_b, M_Z^2)] \cdot \left(1 - \frac{8}{3}\sin^2\theta_W\right)\left(1 - 4\sin^2\theta_W\right) \\
+ \;& [d_{val}(x_a, M_Z^2)\bar{d}_{val}(x_b, M_Z^2) + d_{val}(x_a, M_Z^2)\bar{d}_{sea}(x_b, M_Z^2) \\
+ \;& d_{sea}(x_a, M_Z^2)\bar{d}_{val}(x_b, M_Z^2)] \cdot \left(1 - \frac{4}{3}\sin^2\theta_W\right)\left(-1 + 4\sin^2\theta_W\right)
\end{aligned} \tag{2.31}$$

and the denominator becomes

$$\begin{aligned}
&\int_{-y_0}^{y_0} dy[u_{val}(x_a, M_Z^2)\bar{u}_{val}(x_b, M_Z^2) + u_{val}(x_a, M_Z^2)\bar{u}_{sea}(x_b, M_Z^2) \\
+ \;& u_{sea}(x_a, M_Z^2)\bar{u}_{val}(x_b, M_Z^2) + 2u_{sea}(x_a, M_Z^2)\bar{u}_{sea}(x_b, M_Z^2)] \\
&\cdot 4\left(1 - 4\sin^2\theta_W + 8\sin^4\theta_W\right)\left(1 - \frac{8}{3}\sin^2\theta_W + \frac{32}{9}\sin^2\theta_W\right) \\
+ \;& [d_{val}(x_a, M_Z^2)\bar{d}_{val}(x_b, M_Z^2) + d_{val}(x_a, M_Z^2)\bar{d}_{sea}(x_b, M_Z^2) \\
+ \;& d_{sea}(x_a, M_Z^2)\bar{d}_{val}(x_b, M_Z^2) + 2d_{sea}(x_a, M_Z^2)\bar{d}_{sea}(x_b, M_Z^2)] \\
&\cdot 4\left(1 - 4\sin^2\theta_W + 8\sin^4\theta_W\right)\left(1 - \frac{4}{3}\sin^2\theta_W + \frac{8}{9}\sin^2\theta_W\right) \\
+ \;& 2 \cdot s_{sea}(x_a, M_Z^2)\bar{s}_{sea}(x_b, M_Z^2) \\
&\cdot 4\left(1 - 4\sin^2\theta_W + 8\sin^4\theta_W\right)\left(1 - \frac{4}{3}\sin^2\theta_W + \frac{8}{9}\sin^4\theta_W\right)
\end{aligned} \tag{2.32}$$

$u_{val}(x_a, M_Z^2)$ and $\bar{u}_{sea}(x_b, M_Z^2)$ are the structure functions for the valence u quark in the proton and anti-proton, respectively, and similarly for the d and s valence and sea quarks. Sea quark contributions heavier than s are very small, and are neglected here. The cross-section of equation 2.22 describes only the lowest order diagrams contributing to dilepton production (figure 2.2). There are a number of higher order (order α^3 and higher) effects which also contribute. One of these, initial state gluon radiation, results in the production of Z^0's with non-zero transverse momentum. In this situation, the directions of the proton and anti-proton are not collinear in the rest frame of the dilepton, and as the P_t increases, the directions of the quark and anti-quark with respect to the hadrons

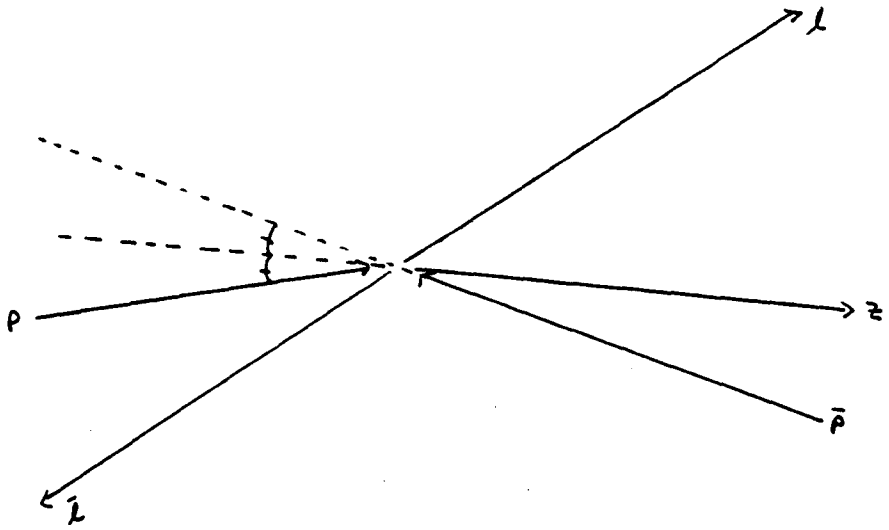

Figure 2.5: $q\bar{q} \longrightarrow Z^0 \longrightarrow \mu^+\mu^-$ in the Collins-Soper frame

become less certain. Thus, for Z^0's with finite P_t, the angle $\cos\theta$ is not well-defined. To avoid this problem, this analysis adopts the angular convention of Collins and Soper [14], which the z axis becomes the bisector of quark and anti-quark directions in the rest frame of the leptons, and $\cos\hat{\theta}$, is defined as the cosine of the angle between the outgoing negative lepton and this new z axis. See figure 2.5. According to Collins and Soper, $\cos\hat{\theta}$ has the Lorentz invariant form

$$\cos\hat{\theta} = \frac{(P_0^- + P_3^-)(P_0^+ - P_3^+) - (P_0^+ + P_3^+)(P_0^- - P_3^-)}{M_{ll} \cdot (M_{ll}^2 + (P_t^{ll})^2)^{1/2}} \qquad (2.33)$$

where $P_0^{\pm}$ and $P_3^{\pm}$ are the energy and z component of momentum of the positive

and negative leptons, $M_{l\bar{l}}$ is the mass of the dilepton, defined in terms of the leptons' energies and momenta as

$$M_{l\bar{l}}^2 = \left(P_0^- + P_0^+\right)^2 - \left(P_1^- + P_1^+\right)^2 - \left(P_2^- + P_2^+\right)^2 - \left(P_3^- + P_3^+\right)^2 \qquad (2.34)$$

and $P_t^{l\bar{l}}$ is the transverse momentum of the dilepton,

$$(P_t^{l\bar{l}})^2 = \left(P_1^- + P_1^+\right)^2 + \left(P_2^- + P_2^+\right)^2 \qquad (2.35)$$

In this frame, the contributions to the P_t of the Z^0 are divided equally between the quark and anti-quark. Moreover, while this formulation does not eliminate the uncertainty in $\cos\hat{\theta}$ at high P_t, it does have the feature that as $P_t^{l\bar{l}} \longrightarrow 0$, the z axis becomes the quark direction. The smearing effects on $\cos\hat{\theta}$ from the P_t of the Z^0 are further discussed in chapter 4.

Chapter 3

Event Selection

3.1 Event Selection

The events used in this analysis were selected from $3.54 pb^{-1}$ of data gathered during the Tevatron collider run which lasted from June of 1988 through May of 1989. The initial selection process required that the event contain at least two high momentum tracks, at least one of which was required to trigger the central muon drift chambers, registering hits in at least two of the four drift layers of that detector. Such a track, or 'stub', in the central muon chambers is called a Central Muon Object, or CMUO. (Hereafter, Central muon stubs will be referred to as CMUO's, for convenience). The second track was required to either

1. register a track in the forward muon detector, i.e., a forward muon object(FMUO)

2. fall anywhere in the in the pseudo-rapidity region from -1.4 to 1.4.

Since the CMU chambers cover only rapidities between $-.61$ to $-.04$ and 0.04 to $+.61$, and, moreover, contain 24 gaps in the ϕ coverage each 3° wide and spaced at regular intervals of 12.5°, this implies that the second leg may be neither a CMUO nor an FMUO, but may miss the muon coverage entirely, and leave only a high P_t track in the central tracking chambers. Such tracks are called CMIO's, for Central Minimum Ionizing Objects. The term CMIO is somewhat confusing, since the only requirements for the identification of a track as such is that it recontruct in the CTC with a P_t of 10 GeV/c or greater, and that there be no associated stub in the CMUO chamber. In fact, these tracks need be neither 'central' (where 'central' is generally understood to describe the eta range of the CTC and central calorimeters, i.e $-1.1 < \eta < 1.1$), nor deposit energy in the calorimeters consistent with that of minimum ionizing radiation. The CTC reconstructs tracks out to $\eta \sim 2.2$, well into the forward region, and beyond the range of the CMU chamber, for instance, and all of these tracks with $P_t > 10$ GeV/c are called CMIO's. The user must place the η, P_t, and calorimetry cuts on energy depostion and energy isolation in the calorimeters to reliably identify CMIO's as muons from Z^0 decay. The name CMIO is, thus, primarily historical, but will be used from here on out for convenience, to describe high P_t CTC tracks which lie in the pseudo-rapidity region $-1.4 < \eta < 1.4$, and which do NOT have an associated CMUO stub.

3.1.1 Central Muon Identification

3.1.1.1 CMUO-CTC Track Matching

The signature for a central muon from vector boson decay at CDF is an isolated, high pt track in the CTC accompanied by a small calorimeter signal. For events in which there is also a central muon stub present, the match in the $r-\phi$ plane between the CTC track and the stub is required to be $< 10cm$. This match is referred to as DIX. Figure 3.1 shows the matching distribution between muon stubs and their CTC tracks in $J/\psi \longrightarrow \mu^+\mu^-$ events gathered at CDF during the 1988-89 run. For high P_t muons, the distribution of DIX is gaussian with a width of $\sigma \simeq 12cm/P_t$. For 18 GeV/c muons, then, $\sigma \simeq 0.7$, and the requirement that $|DIX| < 10$ cm is actually a 15σ cut. The efficiency of DIX <10 cm cut is 100% for muons with $P_t > 6$ GeV/c [15].

3.1.1.2 Calorimetry Requirements

Muons are also minimum-ionizing particles. The amount of energy they deposit in the calorimeters is small. Plots of the energy deposited in the central electromagnetic and central hadronic calorimeters by muons from a 57 GeV/c testbeam are shown in Figure 3.2 and Figure 3.3 Muons from Z^0 decay are also independent of any other activity in the event and thus should appear isolated in the tracking detectors and calorimeters. Energy deposition in the calorimeters in a cone with radius defined in $\eta-\phi$ space about the muon should be small, and reflect only

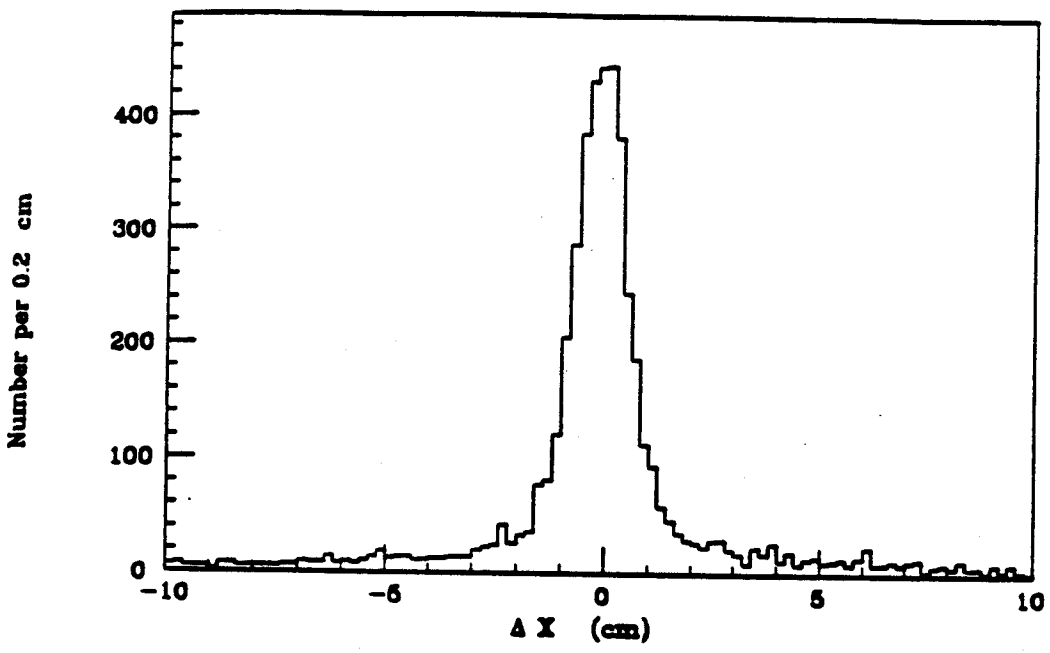

Figure 3.1: CTC-CMUO stub match in the x-y plane for $J/\psi \longrightarrow \mu^+\mu^-$ events.

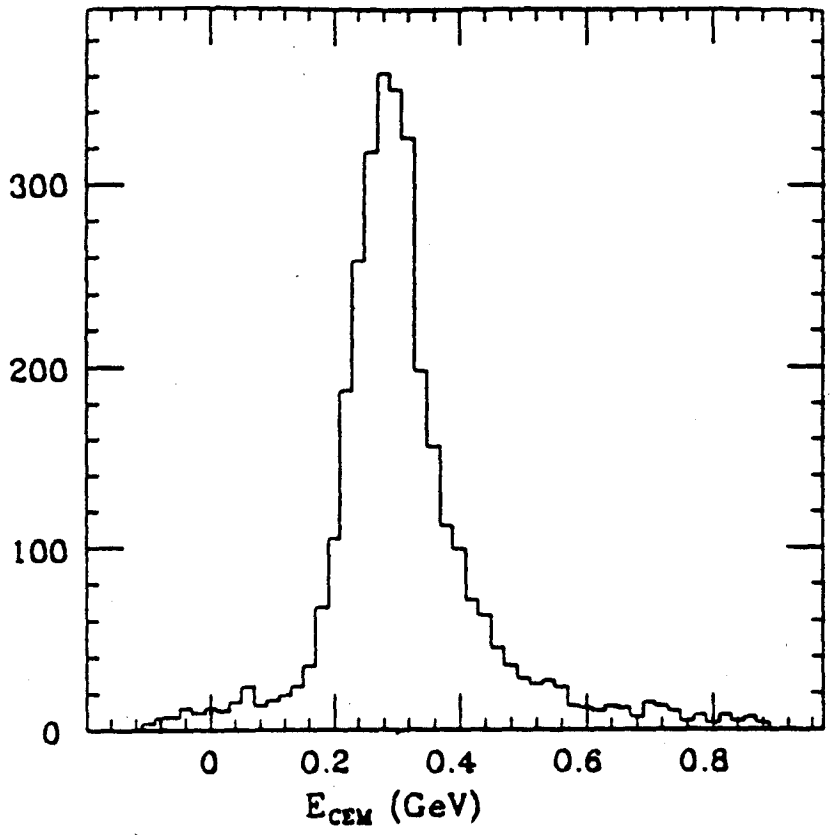

Figure 3.2: CEM energy deposition for 57 GeV/c test beam muons.

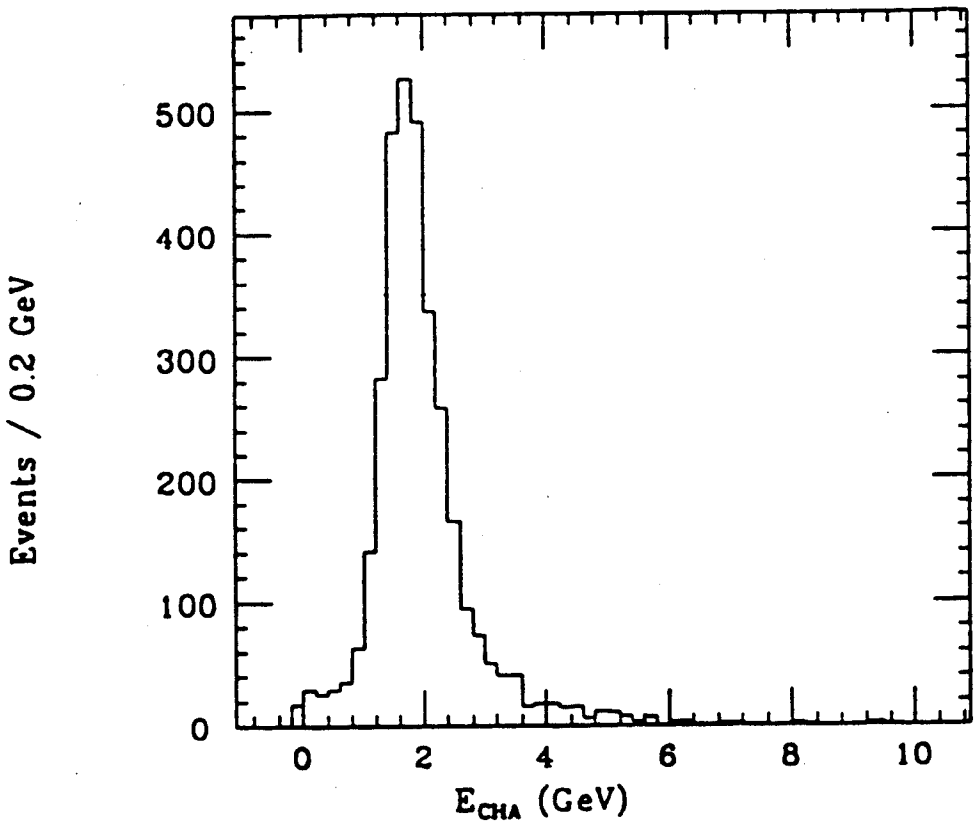

Figure 3.3: CHA energy deposition for 57 GeV/c test beam muons.

the underlying event. The mean energy deposition in the central electromagnetic calorimeter for test beam muons was 0.3 GeV, in the central hadronic calorimeter, 2.14 GeV, for a cone of radius = 0.13. The 'standard' requirements energy deposition for muons in most CDF analyses are that $E_{had} < 6$ GeV and $E_{em} < 2$ GeV. These are 12 and 30 σ cuts, respectively. The efficiencies of these cuts were determined using known muons from J/ψ decays, cosmic rays, and from the second leg of Z^0 events. The efficiency of the combined hadronic and electromagnetic energy cuts was determined to be $98.7\% \pm 0.3\%(stat.) \pm 0.2\%(sys.)$ [16], and Table 3.1.

3.1.1.3 Muon Isolation Requirement

A calorimetry isolation cut, ISO, is used to remove QCD background in the form of jets from the sample. ISO is defined as the total energy deposited in a $\eta - \phi$ cone with radius = 0.4 about the muon minus the energy of the muon tower itself, and normalized by the P_t of the muon:

$$ISO = \frac{E(R = .4) - E(R = .13)}{P_t} \tag{3.1}$$

For the Z^0 sample, a cut of $ISO < 0.1$ was used on CMUO in FMUO-CMUO and CMUO-CMIO events, and on the first CMUO in CMUO-CMUO events. The CMIO and second CMUO were required to satisfy $ISO < 0.2$. No isolation cut was necessary for the FMUO's. The efficiency of the 0.1 cut was determined by studying the energy deposition from the underlying event in cones of $R = 0.4$

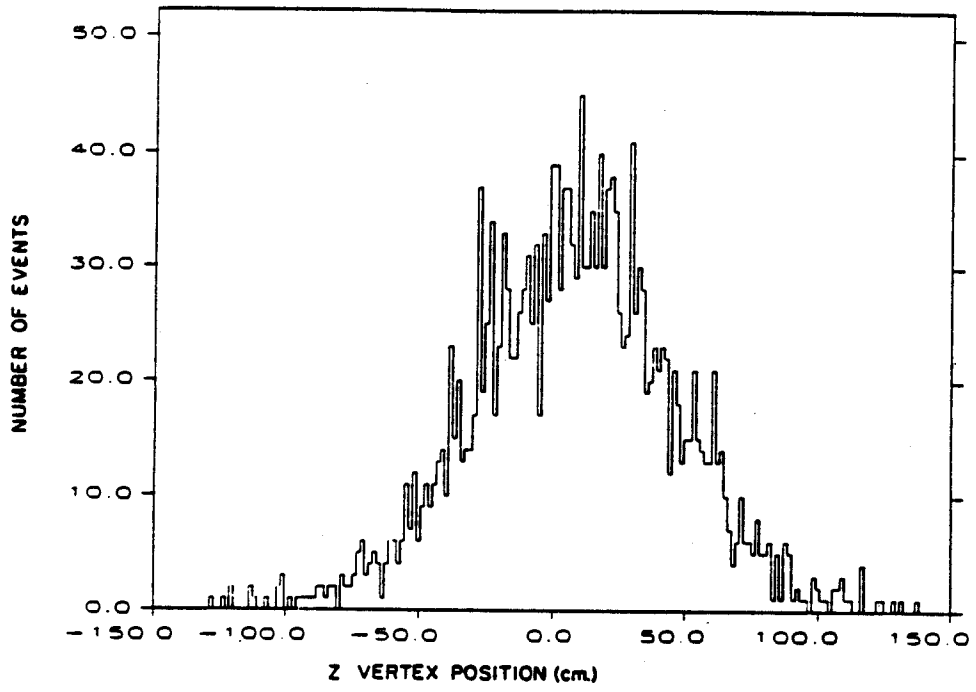

Figure 3.4: Distribution of vertices along the beam axis for a typical CDF run

away from the muon in $W \longrightarrow \mu\nu$ events, using a variety of muon selection criteria, and constraints on jets in the event. This procedure is described more fully in [17]. The efficiency of the $ISO > 0.1$ cut was found to be $0.98 \pm 0.01\%$, and is included in Table 3.1.

3.1.1.4 Vertex Requirement

Muons in the sample were required to originate from a primary vertex (i.e. associated with a $p\bar{p}$ collision) within ± 60 cm along the beam axis (the z axis) of $z = 0$. This is a 2 σ cut. See Figure 3.4.

3.1.1.5 Cosmic Ray Background

Cosmic rays which leave high P_t, isolated tracks in the tracking chambers are a major background to di-lepton events, and are removed from the sample with a software filter. This filter, which is fully described in [21], uses a number of criteria to identify cosmics: a large impact parameter of the track with respect to the beam position, an anomalously large vertex position, two stiff tracks which are almost exactly 180° back-to-back in $\theta - \phi$ space, timing of the tracks relative to beam crossing, and time of flight between pairs of CTC tracks consistent with the pair actually originating from a single particle crossing the whole detector, rather than from two particles from a $p\bar{p}$ collision arriving at the muon counters at the same time. The efficiency of this filter was studied with 4521 events from the 1988-1989 data run containing high P_t central muon candidates, and scanning those which failed the filter. It was concluded that the cosmic filter was better than 99.8% efficient for the removal of cosmic rays[21].

3.1.1.6 Fiducial Requirements on the CMUO

All dimuon pairs in this analysis were required to have at least one of the muons fall within the fiducial region of the central muon drift chambers where the acceptance and trigger efficiency were well-understood (i.e. away the chamber edges where the electric field is distorted by the endplates and wire feed-throughs). The 'good' fiducial region of the chambers begins actually several centimeters inside the chamber walls, both in phi and eta. Figures 3.5 and 3.6 show the

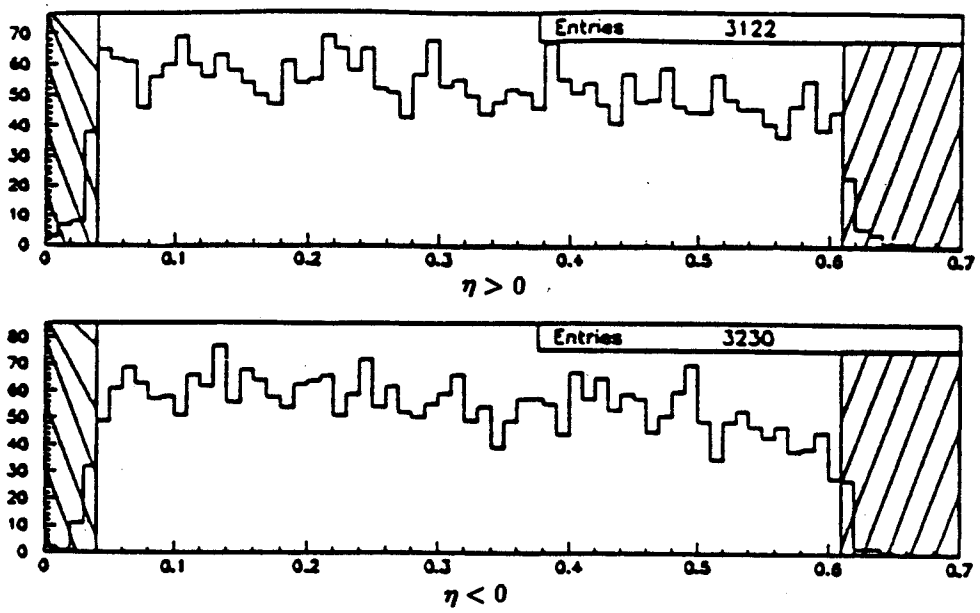

Figure 3.5: Fiducial boundaries in η for CMUO's

fiducial cut-offs in η and ϕ for tracks pointing to the central muon chambers. To determine whether a CMUO stub falls into the good fiducial region, a software routine described in [20] was used to propagate the track, using the event vertex and the track's momentum vector, through the CTC, calorimeters, and accompanying magnetic fields to the radius of the central muon chambers. The fiducial cuts were made on the propagated values of ϕ and η.

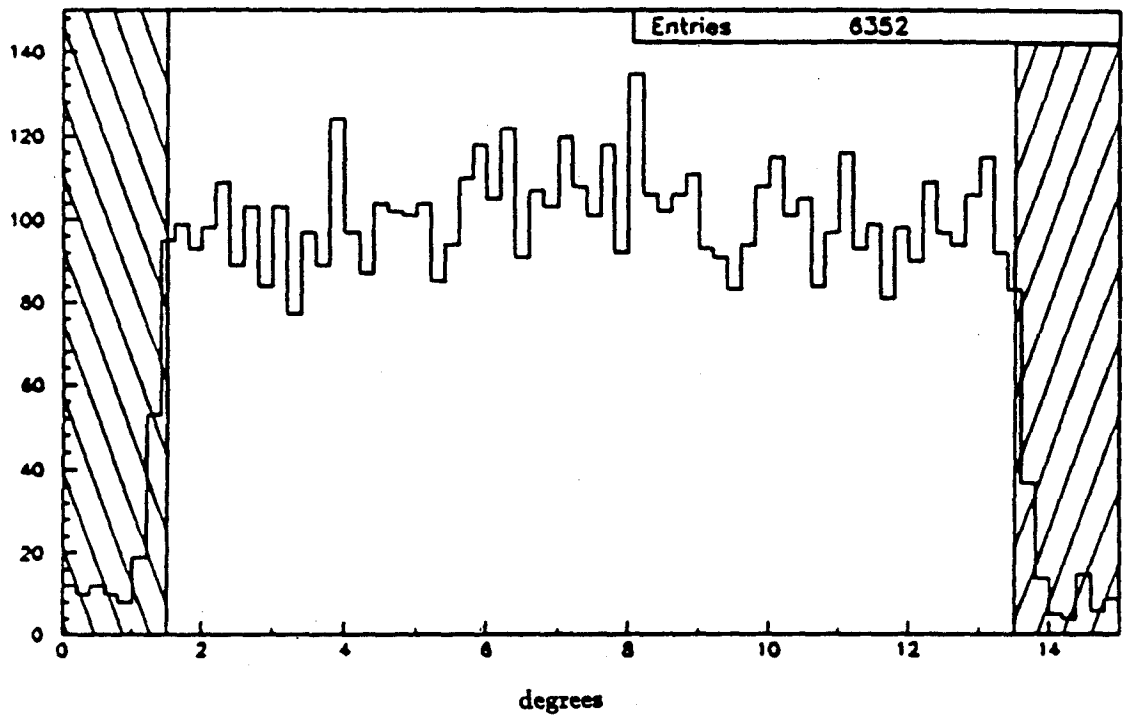

Figure 3.6: Fiducial boundaries in ϕ for CMUO's.

3.1.2 Selection of the Z^0 Samples

The event selection for the $Z \longrightarrow \mu^+\mu^-$ samples proceeded as follows: From $3.54pb^{-1}$ of data, all events were selected which contained:

- at least 1 CMUO having :
  1. $P_t \geq 20$ GeV/c.
  2. $DIX < 10$ cm.
  3. energy deposition in the hadronic calorimeters, $E_{\rm had} < 6$ GeV.
  4. energy deposition in the electromagnetic calorimeters, $E_{em} < 2$ GeV.
- AND that there exist at least one other CMUO, CMIO, or FMUO in the event.

At this point, there were no requirements placed on the second track other than existence. This yielded 11,485 events.

Next, all of these events had their CTC tracks were re-fit with tracking code which constrained each track to intersect the beam position. This reduced the sample to 3295 dimuon events where 138 were FMUO-CMUO pairs and 3157 were CMUO-CMUO or CMUO-CMIO pairs. The difference in numbers before and after the re-fit is due to the loss of non-primary tracks (i.e. ones not originating from the primary $p\bar{p}$ interaction vertex) in the initial sample which could not be re-fit to point to the beam. Such tracks consist largely of kaons decaying-in-flight to leptons, cosmic rays and pions. At this point, due to the differing momentum

resolutions of the CTC and FMU chambers, it is appropriate to consider the FMUO-CMUO pairs as a distinct sample from the CMUO-CMUO and CMUO-CMIO pairs. To select CMUO-CMUO and CMUO-CMIO Z candidates, it was next required required that:

- the first leg of the pair be a CMUO with :
  - $P_t \geq 20$ GeV/c.
  - $DIX < 10$ cm.
  - $E_{had} < 6$ GeV.
  - $E_{em} < 2$ GeV.
  - $ISO < 0.1$
  - z vertex $-60 < z < 60$ cm.
  - the track is not flagged as a cosmic by the cosmic ray filter.
- and that the second leg of the pair have :
  - $P_t \geq 20$ GeV/c.
  - $DIX < 10$ cm, if track has a CMUO stub associated with it.
  - $E_{had} < 6$ GeV.
  - $E_{em} < 2$ GeV.
  - $ISO < 0.2$

- also passed the cosmic ray filter as non-cosmic
- pseudo-rapidity $| \eta | < 1.4$
- z vertex $-60 < z < 60$ cm, AND
- z vertex within 3 cm of the z vertex of leg 1, i.e. $| z_1 - z_2 | < 3$ cm.

- At least one of the two legs must fall in the good CMUO fiducial region described above.
- the event have run number ≥ 17265 and $\neq 17278$.

The last quality cut, on the CDF run number, elimenates data taken at a time when the Central Muon Level 2 trigger hardware was malfunctioning. The level 2 trigger efficiency for these runs is unknown. In order to calculate the acceptance for central muon events correctly, only events in which their trigger efficiency was well-understood were used. Thus, these events were eliminated from the sample. These cuts reduce the sample to 158 central-central dimuons, with 146 Z^0 candidates lying in the mass range $75 - 115$ GeV/c^2. These events are shown in Fig. 3.7 fitted with a gaussian over the range $75 - 115$ GeV/c^2.

The selection efficiencies of the individual central muon cuts and the overall selection efficency of central muons are listed in Table 3.1 and described in [17].

Plots of the various muon quality parameters are shown in figure 3.8. The absence of like sign pairs in figure 3.7 strongly indicates this sample is free of background, as do the small number of events eliminated by the isolation cuts.

Central Muon Selection Efficiencies	
Selection Cut	Efficiency
$E_{had} < 6$ GeV and $E_{em} < 2$ GeV	$98.7 \pm 0.2 \pm 0.2\%$
ISO< 0.1	$98 \pm 1\%$
Cosmic filter	$99.7 \pm 0.2\%$
DIX < 10 cm	100%
Central Muon Trigger	$91 \pm 2\%$
Stub-finding	$98.6 + 1.2 - 3.3\%$
Combined Efficiency	86.5

Table 3.1: Central Muon Selection Efficiencies

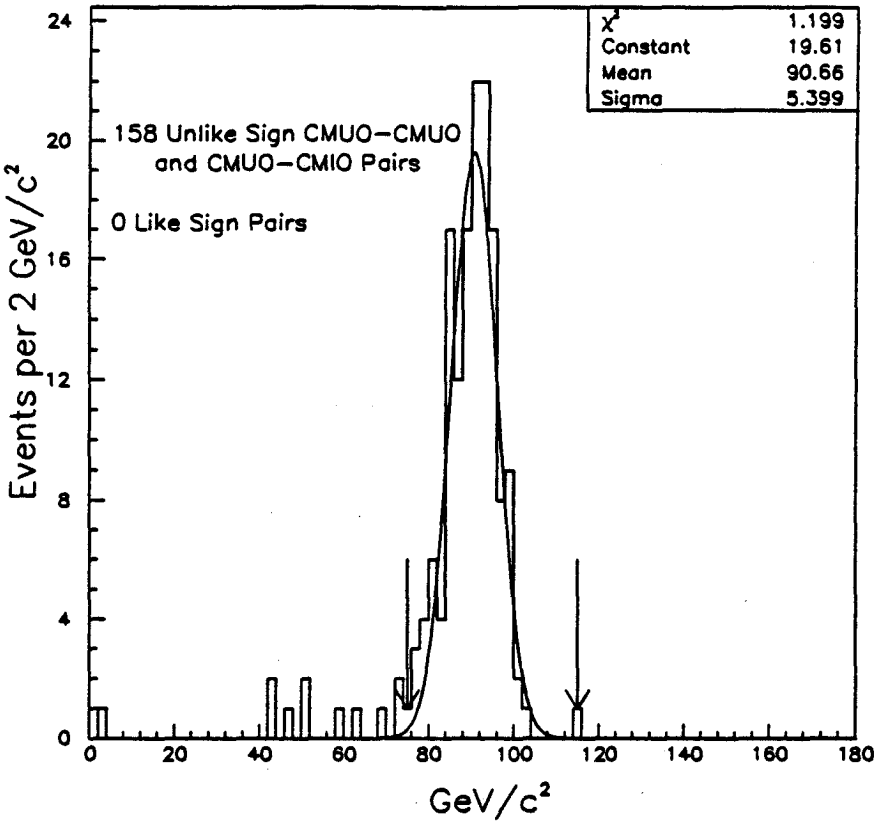

Figure 3.7: CMUO-CMUO and CMUO-CMIO mass spectrum after bad trigger runs were eliminated. Arrows indicate the mass range used in the asymmetry analysis.

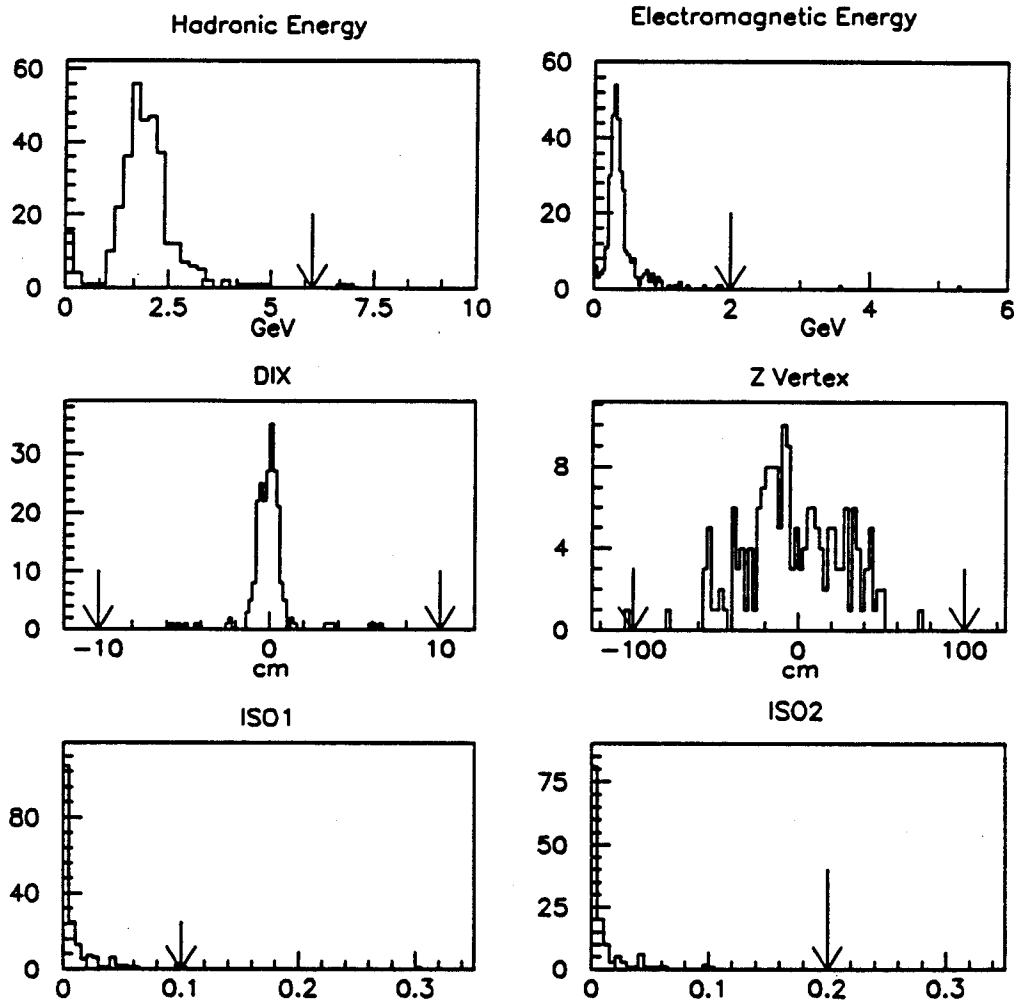

Figure 3.8: Central Muon quality parameters for the 188 central-central and central-forward Z^0 candidates. Arrows indicate the cut requirement.

The η cut on the second leg of the pair was chosen to eliminate like sign events. Figure 3.9 shows plots of $|\eta|$ of the second leg of CMUO–CMUO and CMUO–CMIO pairs when cut on η for that leg is eliminated. The top plot shows the unlike sign pairs, while the bottom plot shows the like sign. The five like sign events are possibly Z^0 decays in which the high η muon has had its curvature, and hence its charge mismeasured. Tracks which fall beyond η of 1.0 do not traverse all of the superlayers of the CTC. Refer to Table 3.2 [22] showing the correspondences between detector η, axial or stereo layer wire number,and superlayer in the CTC. As η increases, the reduced number of CTC wires available to the track degrades the quality of the curvature measurement, and the probability of mismeasurement of the sign of the track increases. Given that there are no known high mass objects which decay to like sign lepton pairs, Figure 3.9 indicates that above $\eta = 1.4$ charge measurement becomes unreliable for CTC tracks.

3.1.2.1 Track-Finding Efficiency of the Central Tracking Chambers

The track-finding efficiency of the CTC as a function of η was studied using a sample of $Z \longrightarrow e^+e^-$ events. The energy resolution of the electromagnetic calorimeters at CDF is such that these events can be reliably identified using energy information from these detectors, and without using any tracking information whatsoever. However, as charged particles, the electrons from Z^0 decays leave stiff tracks in the central tracker, which also can be used to identify these events. In order to study the fall-off of CTC track-finding efficiency with in-

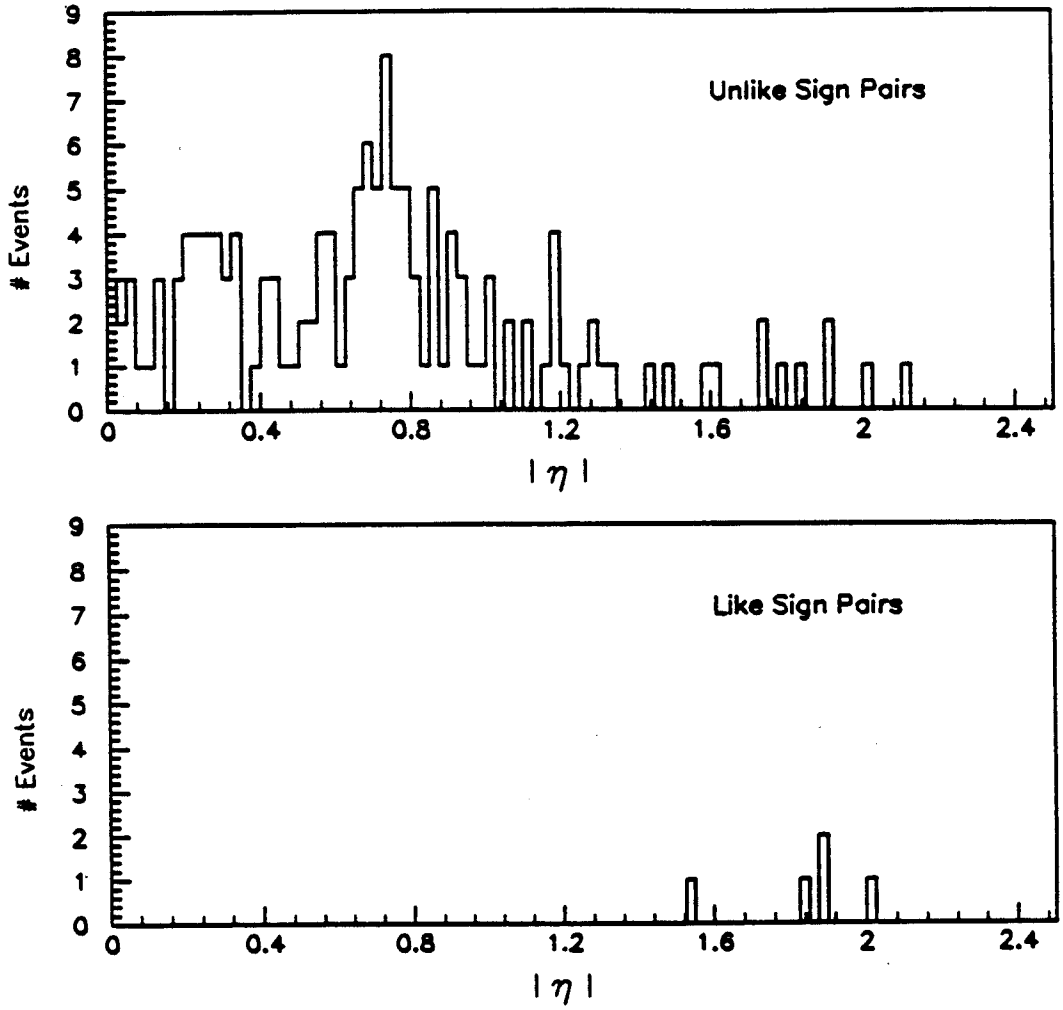

Figure 3.9: $|\eta|$ for like and unlike sign CMUO-CMUO and CMUO-CMIO pairs.

Wire Layers in CTC	$\mid \eta_{det} \mid$	Superlayer
$0 - 11$	$2.35 - 2.13$	0
$12 - 17$	$1.99 - 1.92$	1
$18 - 29$	$1.80 - 1.68$	2
$30 - 35$	$1.59 - 1.55$	3
$36 - 47$	$1.47 - 1.39$	4
$48 - 53$	$1.33 - 1.30$	5
$54 - 65$	$1.24 - 1.18$	6
$66 - 71$	$1.14 - 1.11$	7
$72 - 83$	$1.07 - 1.03$	8

Table 3.2: CTC wire numbers broken down by $\mid \eta \mid$ region and superlayer.

creasing η, a sample of $Z \longrightarrow e^+e^-$ events was gathered in which one electron went into the central electromagnetic calorimeter, and the second went either into the CEM as well, or into the plug electromagnetic calorimeter anywhere up to a pseudo-rapidity of 1.4. The approach used in this study was to identify these events solely on the basis of the calorimeter cluster information, then to check how often the cluster had associated with it a track in the central tracking chambers satisfying the transverse momentum requirement for muons from Z^0 decays. $Z^0 \longrightarrow e^+e^-$ events were gathered from an inclusive electron sample comprising $4.05 \pm 0.28 pb^{-1}$. The events were selected using the following quality cuts for the central (CEM) and plug (PEM) electrons [25], [27]:

- For the first CEM electron in a CEM-CEM or CEM-PEM pair:
  - E_t (from calorimetry)> 20 GeV/c.
  - CES $\chi^2 < 15$. This χ^2 is a comparison of the consistency of the EM shower profile measured by the CES strip chambers compared to those measured for test beam electrons.
  - $E/P < 1.5$. E/P is the ratio of electron energy measured by the calorimeters to the momentum of the associated CTC track. So, for this study, one CEM electron was always required to have a CTC track match.
  - $\mid \Delta x \mid < 1.5$ cm. This is matching cut in the x-direction between the electron position measured by the calorimeters, and the extrapolated

CTC track. If no match is found, $\Delta x = 0$, and the event is still kept.

- $|\Delta z| < 3$ cm. Analogous to Δx, but in the z-direction.
- LSHR < 0.20. LSHR stands for 'lateral energy-sharing profile' which is a measure of the consistency of energy sharing among the CEM towers in an EM cluster with the sharing observed in clusters made by test beam electrons.
- $ISO < 0.1$, where isolation is defined in terms of the transverse energy of the electron, E_t, and of the transverse energy in a cone about the electron of radius = 0.4 as

$$\frac{E_t^{Cone} - E_t}{E_t}. \tag{3.2}$$

- For the second electron in a CEM–CEM pair:
- E_t (from calorimetry) > 20 GeV/c.
- $ISO < 0.2$.
- For the PEM electrons:
  - E_t (from calorimetry) > 20 GeV/c.
  - $ISO < 0.2$.
  - $\chi^2_{3\times3} < 20$. This χ^2 compares the energy distribution in the PEM in a 3x3 region about the electron with that for test beam electrons.

  - VTPC hit occupancy > 0.5. The electron must have a matching VTPC track and this track must have at least 50% of its total possible hits.
  - $|\eta| < 1.4$.

- Runs which had problems with the missing E_t measurements, luminosity measurements, or large numbers of dead PEM channels where also removed (runs 16785, 17469, 17475, 18869-18947, and 17512-17516).

- The tracks in the event were re-fit by constraining them to pass through the beam, in the same manner as CTC tracks in the $Z^0 \longrightarrow \mu^+\mu^-$ sample.

These cuts resulted in 126 CEM-CEM and 53 CEM-PEM di-electrons with masses reconstructed using momentum information derived from the calorimeters in the range $75-115$ GeV/c^2. These events are shown in figures 3.10 and 3.11. Next, it was required that both electrons in the event have an associated CTC track of $P_t > 20$ GeV/c^2, and that the mass of the di-electron from tracking lie in the range $75 < mass_{ee} < 115$ GeV/c^2 also. These requirements were satisfied by 124 CEM-CEM and 34 CEM-PEM pairs. This implies, therefore, an overall CTC track-finding efficiency of

$$124 \div 126 = 98 \pm 1\% \tag{3.3}$$

in the pseudo-rapidity region covered by the CEM calorimeter $|\eta| < 1.1$, and

$$34 \div 53 = 64 \pm 14\% \tag{3.4}$$

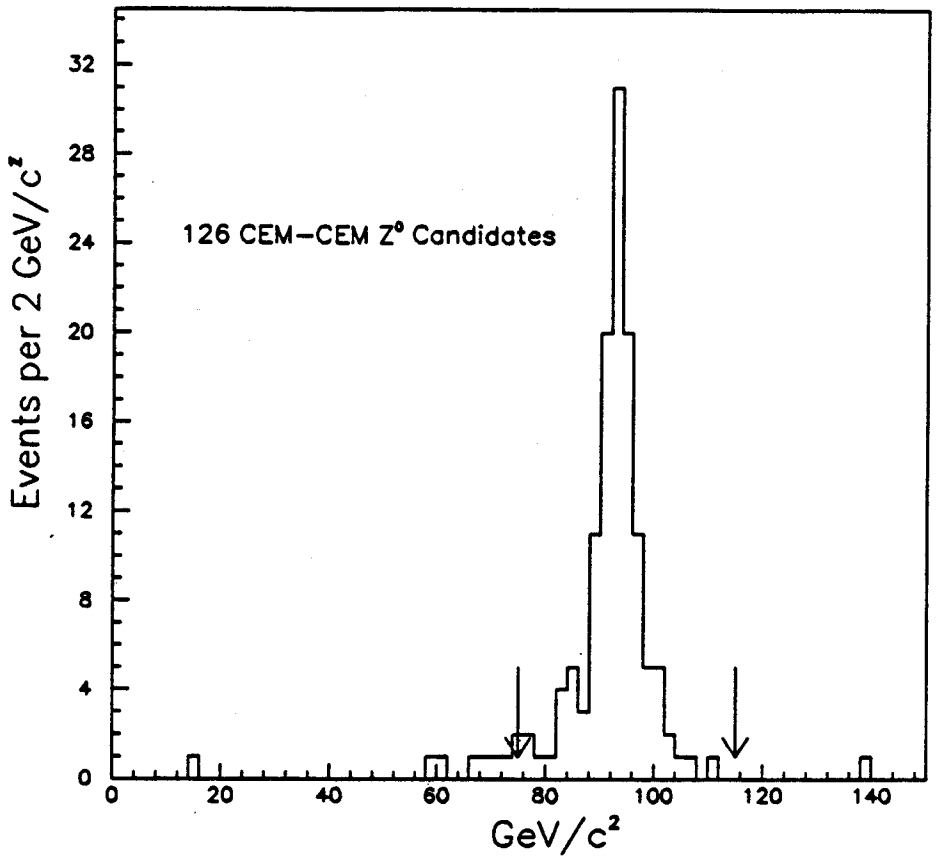

Figure 3.10: Invariant Masses of CEM-CEM $Z^0 \longrightarrow e^+e^-$ events, reconstructed from calorimeter information.

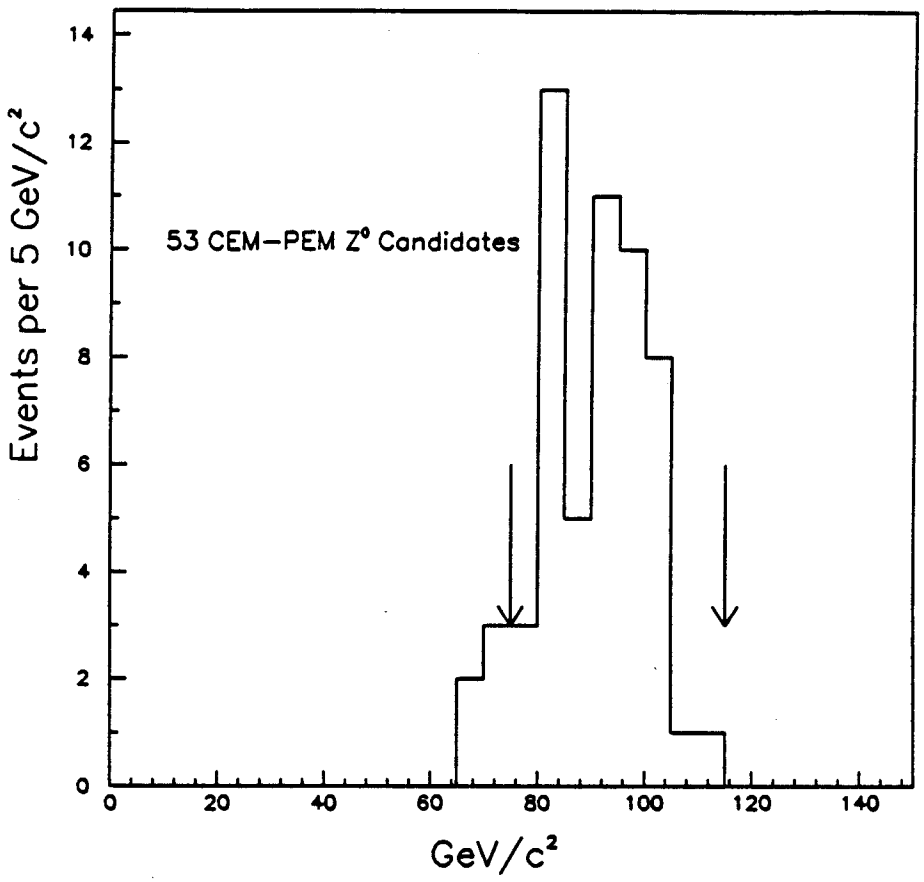

Figure 3.11: Invariant Masses of CEM-PEM $Z^0 \longrightarrow e^+e^-$ events, reconstructed from calorimeter information.

in the pseudo-rapidity region $1.0 < |\eta| < 1.4$.

These efficiencies were inserted into the monte carlo which was used to calculate the acceptance of the Z^0 sample used in the asymmetry analysis.

3.1.3 QCD Background in the Central-Central Sample

Background from QCD processes enter the Z^0 sample through events in which a jet fragmented in such a way as to fake a high P_t, isolated muon. Such events include $W^{\pm}$+ jet and di–jet events. Since such a fake muon would be uncorrelated with any other charged particle in the event, these processes would be as likely to contribute like sign as opposite sign muon pairs. However, as was shown above, there are no like sign pairs in the central-central Z^0 sample over the entire mass range. This strongly indicates that there is no QCD background in this sample. One can also estimate the QCD background to the central-central Z^0 sample by plotting the maximum isolation variable of the pair, ISO, versus the dimuon invariant mass, and examining the side bands in mass and isolation of the resulting scatter plot [30]. See Figure 3.12 If one assumes that the QCD background is uniformly distributed, and that the regions (a) and (c) (i.e. the regions above the isolation cut and above and below the mass cut used in the analysis) are all background, then the number of background events one would expect in the Z^0 region would be equal to the number of events in regions $(a)+(c)$. From Figure 3.12, one sees that there are no events in either region (a) or (c). Alternatively, one can consider the number of background events to be the number

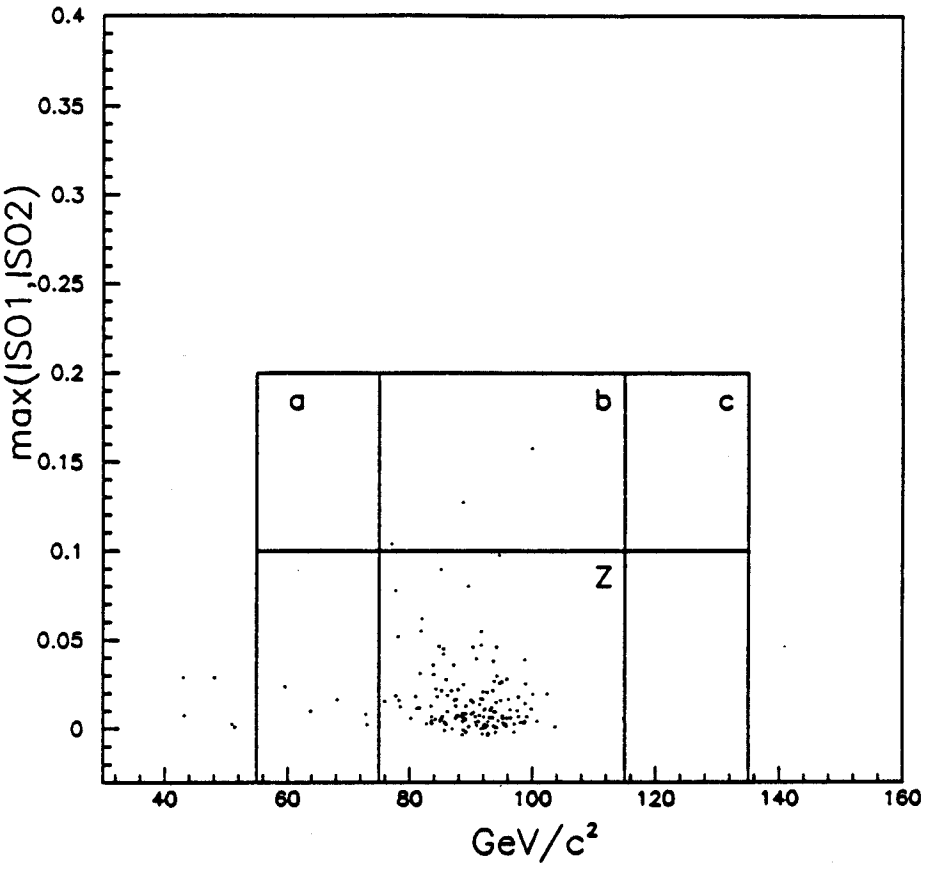

Figure 3.12: Maximum isolation vs. Invariant Mass for Central-Central Dimuons.

of events in region (b) minus the number in the Z^0 region (true Z^0's) which one could expect on a statistical basis to have fluctuated into region (b). There are 143 events in the Z^0 region, and 3 in region (b). The efficiency of the isolation cut, $ISO < 0.1$, is .973. So, the probability for a Z^0 to have $ISOMAX < .1$ (i.e. both legs satisfy $ISO < 0.1$) is $(.973)^2$, or .947. Therefore, the probability for a Z^0 to have $ISOMAX > 0.1$ (i.e. one or both legs in region (b)) is 0.053. $0.053 \times 143 \simeq 8$ events. However, since there are only 3 events in region (b) to begin with, this implies that essentially all of these are real Z^0's which have fluctuated into (b), and hence the QCD background to the central-central sample is 0 ± 1 event.

3.1.3.1 The Forward-Central Dimuon Sample

$Z^0 \longrightarrow \mu^+\mu^-$ events in which one muon traveled through the forward muon chambers and the other through the central muon chambers were selected from the same $3.54pb^{-1}$ sample as the central-central pairs. These events were tagged by making the following requirements:

- For the central muon:
  - $P_t \geq 18$ GeV/c.
  - $DIX < 10$ cm.
  - $E_{had} < 6$ GeV.
  - $E_{em} < 2$ GeV.

- $ISO < 0.1$
- z vertex $-100 < z < 100$cm.
- CMUO was not flagged as a cosmic by the cosmic ray filter.
- the associated CTC track pointed into the good CMUO fiducial region.
- the run number of the event was ≥ 17265.

- For the FMU track it was required that:
- the sum of the electromagnetic and hadronic energies deposited in the calorimeters satisfied $E_{had}^{fmu} + E_{em}^{fmu} < 20$ GeV.
- there were No jets of $E_t > 10$ GeV within a cone of 10° in 3-space about the forward muon.
- the fmu track had pseudo-rapidity in the range $1.96 <| \eta |< 3.37$, which excluded the first nine FMU chamber wires.

Distributions of FMUO quality parameters are shown in Figure 3.13. These distributions, which show the energy deposition of the FMUO in the Plug and Forward calorimeters, the high % of events which have a VTPC track match to the FMUO track, the opening angle in ϕ with the CMUO, all indicate that FMUO–CMUO Z^0 events are well-tagged by requiring a high quality CMUO and the existence of a $P_t > 10$ GeV/c FMUO in the event. As one can see from the spectrum of invariant masses in Figure 3.14 of the 57 resultant forward-central

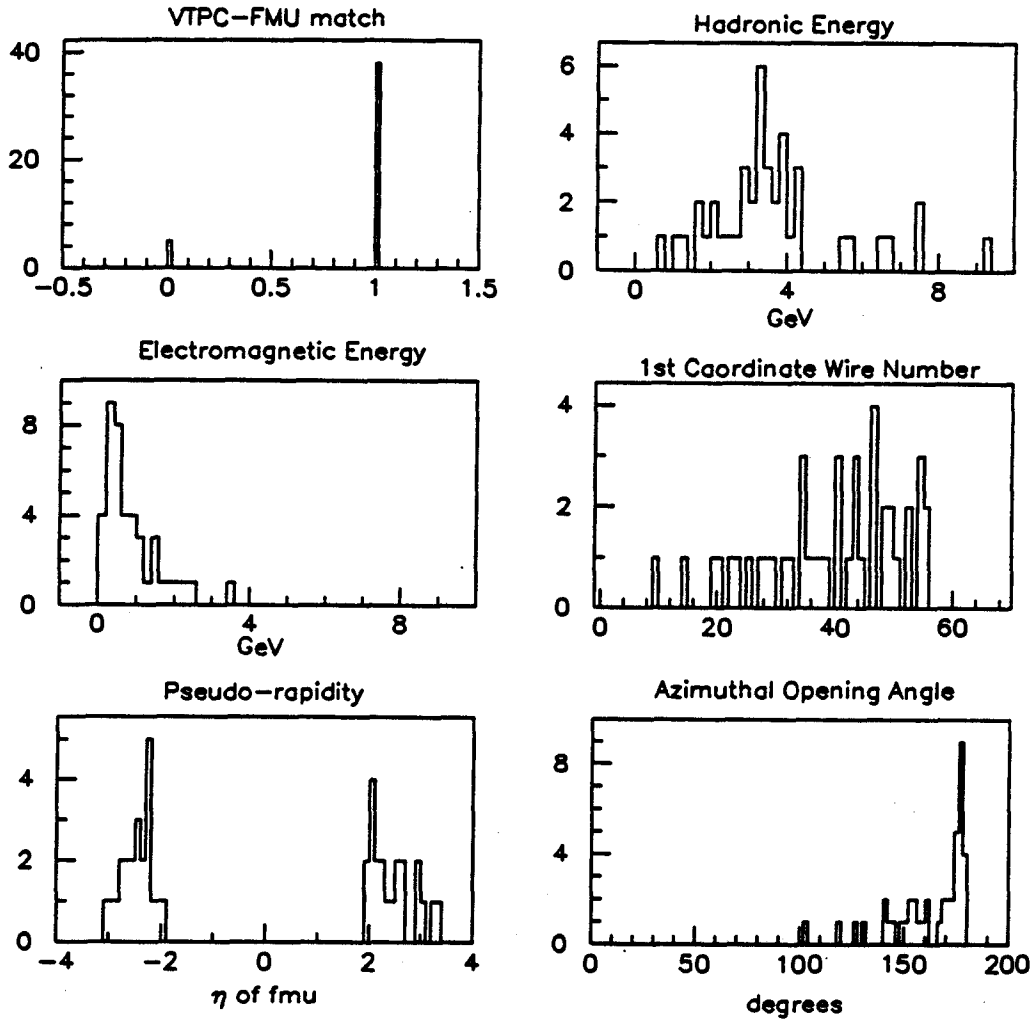

Figure 3.13: Forward Muon quality parameters in FMUO-CMUO dimuons.

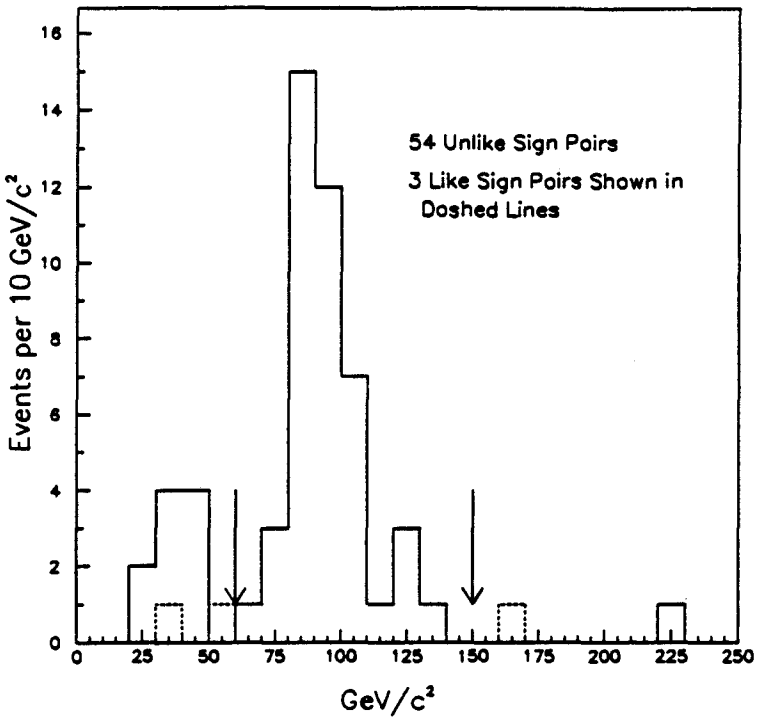

Figure 3.14: Invariant Masses of 57 Forward-Central Dimuons after all central muon cuts, and FMUO isolation, are applied.

pairs, once the central muon is tagged with the above described cuts, one needed only to require the existence of an isolated stub in the Forward Muon chambers to bring out a well defined Z^0 signal. Also, the absence of like sign pairs in the region of the Z^0 peak is one indication that there is very little background in the signal region. The FMU P_t spectrum of these muons is shown in figure 3.15. This figure shows a low P_t pile-up consisting of 12 dimuons in which the FMU P_t is less than 10 GeV/c.

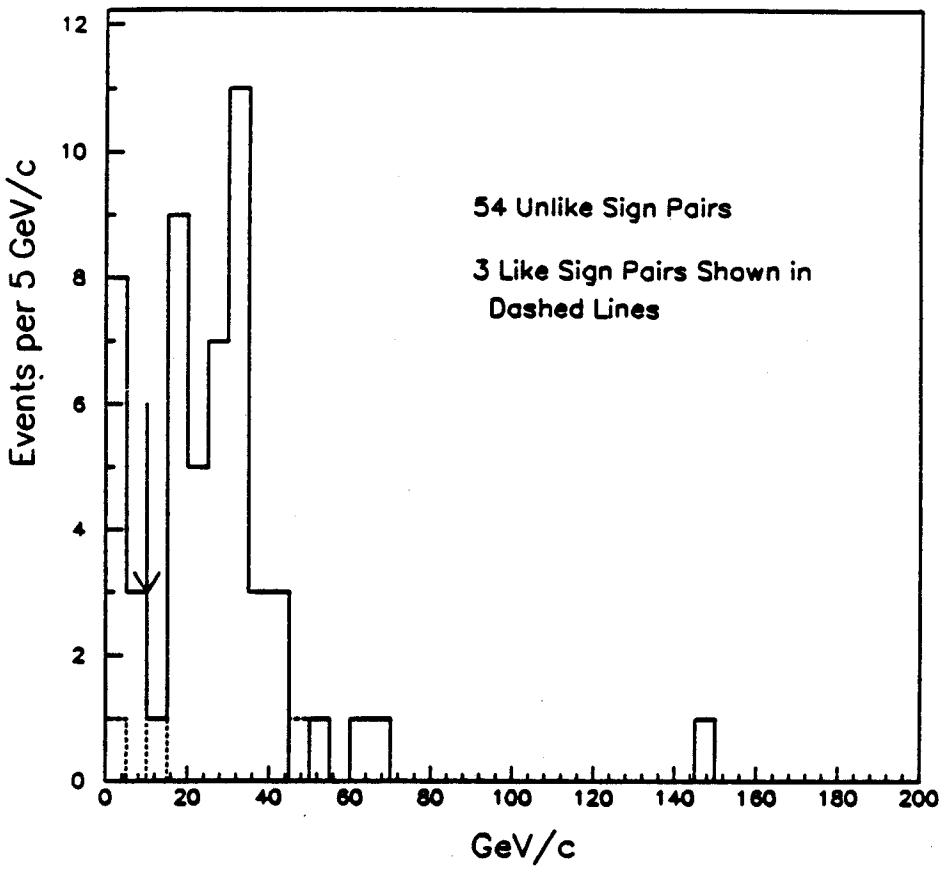

Figure 3.15: P_t **spectrum of the Forward muon in 57 Forward-Central pairs after all central muon cuts, and the FMU isolation and wire cuts, are applied.**

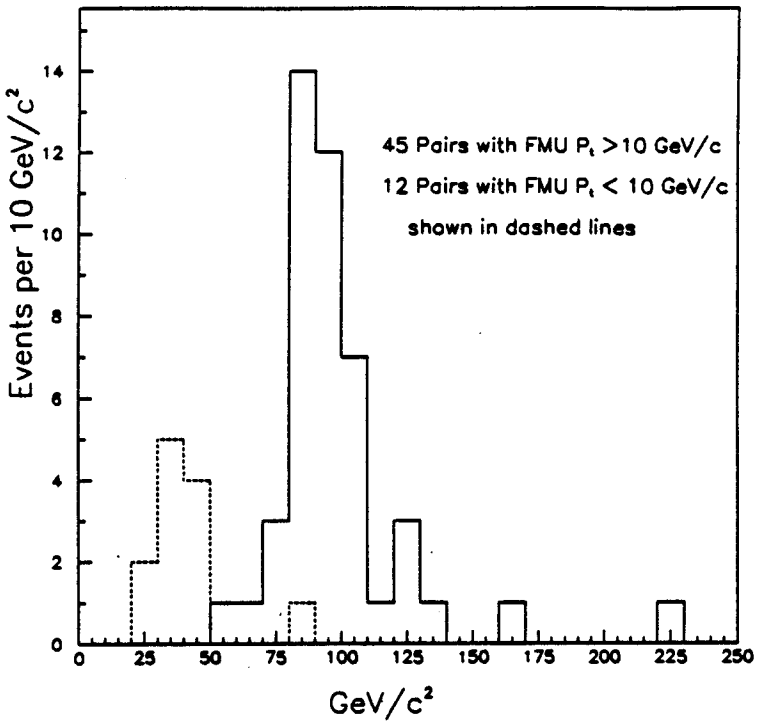

Figure 3.16: Contributions to FMUO-CMUO mass spectrum from $P_t^{fmu} < 10$ GeV/c and $P_t^{fmu} > 10$ GeV/c events.

These events also form a distinct peak visible in the mass spectrum below the Z^0 resonance in figure 3.14. Figure 3.16 shows the contribution to the mass spectrum from pairs with $P_t^{fmu} < 10$ GeV/c superimposed on that from pairs with $P_t^{fmu} > 10$ GeV/c.

3.1.3.2 P_t Mismeasurement in the Forward Muon Drift Chambers

It is believed that there are three sources which contribute to the low end structure of these two plots:

1. Low mass $\mu^+\mu^-$ pairs produced by the Drell–Yan mechanism. jet events.
2. Low mass $\mu^+\mu^-$ from Z^0 decay in which the momentum of the FMU has been mismeasured within the known resolution errors of the FMU system.
3. Low mass $\mu^+\mu^-$ from Z^0 decay in the momentum of the FMU has been mismeasured by effects not included in the simulation.
4. High P_t central muons from $W^\pm$ or b decay, with a background FMU track. The forward muon may be any of the following:
   - a $\pi - K$ decay-in-flight muon.
   - a prompt muon from decay of a b or c quark.
   - a fake track reconstructed from spurious hits in the FMU chambers.

It is possible to estimate the number of events falling into the category #4 by counting the number of like sign pairs in the sample, and also by counting the number of forward muons which appear in the $W \longrightarrow e\nu$ events. (The number of events in category #4 in which the central muon is from b rather than W decay is essentially zero, given the tight isolation cut. Events in this category feature central muons from W decay). There are 3 like sign pairs in figure 3.14. This implies that

$$3 \pm 1.7 \times 2 = 6 \pm 3.5 \tag{3.5}$$

of the 57 events shown in 3.14 are background. Since two of the like sign pairs have $P_t^{fmu} < 10$, this would lead one to estimate that 4 ± 3 of the 12 events

with $P_t^{fmu} < 10$ are background, and that 1 ± 1 of the high P_t^{fmu} events are background.

Independent determination of the number of events in category #3, in which the Z^0 is lost due to mismeasurement of the FMU P_t is difficult, however, since all of the mechanisms which produce this mismeasurement are not completely understood. It is believed that two of the contributing effects are

- random errors in the survey of the chamber positions.
- the fitting of spurious hits caused by delta rays surrounding the true track hits.

As described in chapter 2, a reconstructed track in the FMU chambers should have 5 or six wire hits, one on each wire within a 300% wire road. In practice, there were often more hits than this arriving within the TDC clock window. A typical track with 'extra' hits is shown in figure 3.17. It is believed that these 'extra' hits originate from $\delta-$rays created by the passage of the muon through the chamber walls and in the last half centimeter of toroid iron. Such extraneous hits are characteristic of most tracks in the forward muon system. 37 of the 57 forward muons in the above described FMUO–CMUO pairs have at least 1 extra hit, where an 'extra hit' is defined as a hit on the same wire or on one immediately adjacent to the one used in the fit. See fig. 3.18. It was often difficult to distinguish 'extra' from 'primary' hits on the basis of timing, hit residual, or any other criteria [5]. The FMU track-finding code selected whichever 5 or 6

(A)

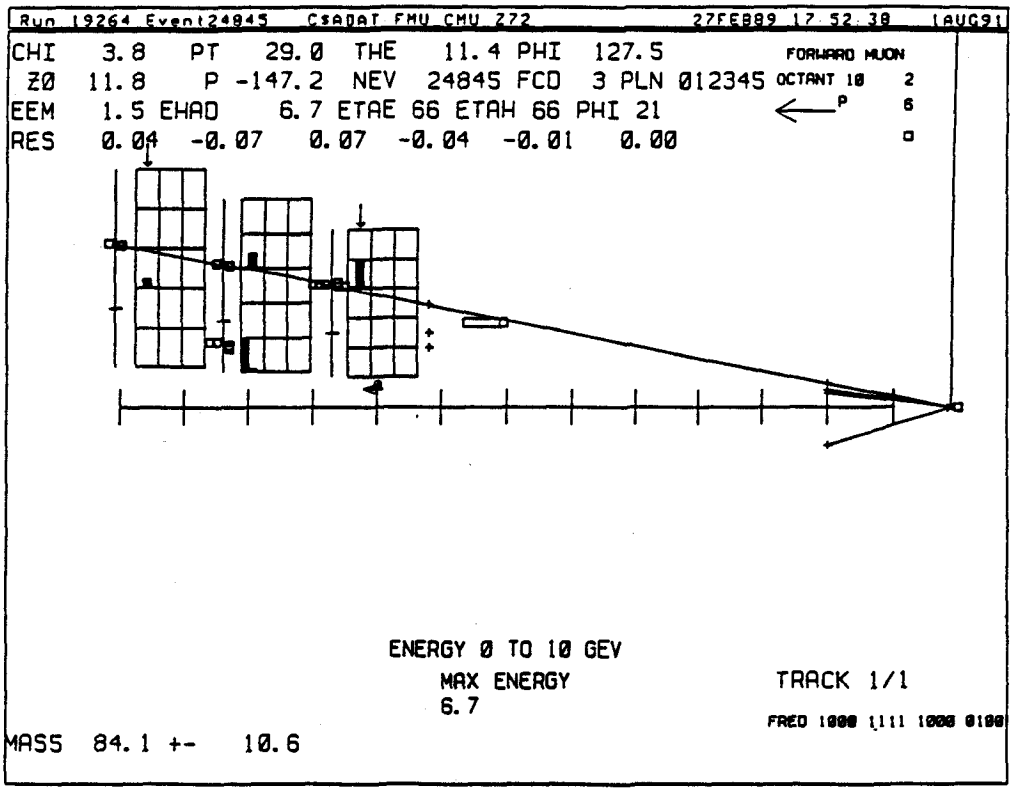

(B)

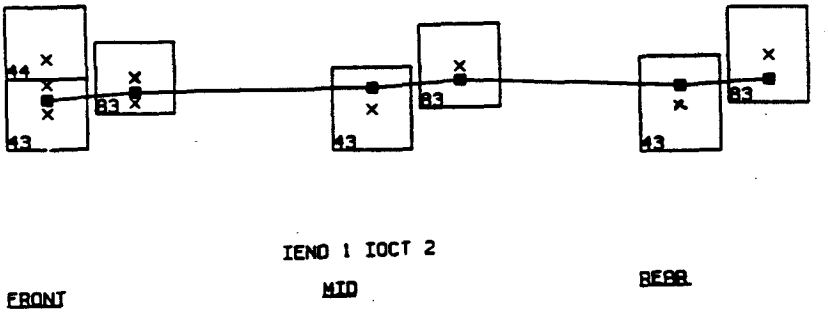

Figure 3.17: (A) A Track in the Forward Muon Drift chambers showing 4 extra hits from Delta rays. (B) enlarged view of the drift cells crossed by track.

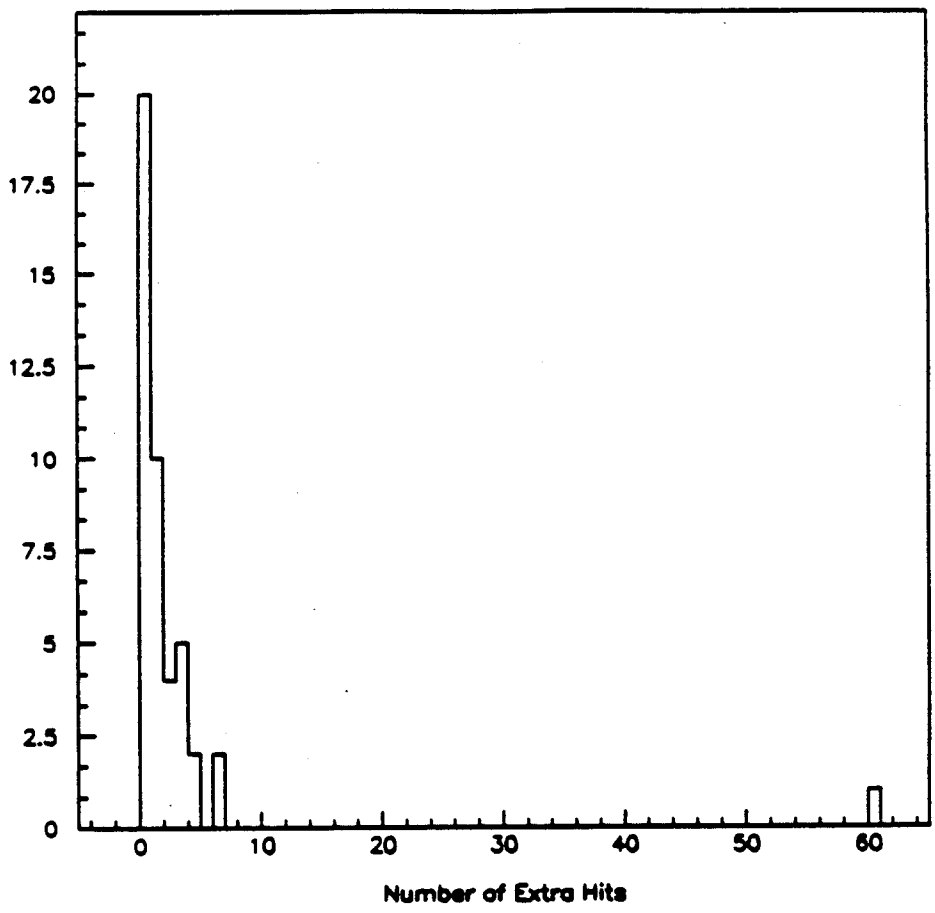

Figure 3.18: Extra Hit Multplicity for the FMU tracks in 57 FMUO–CMUO Dimuons.

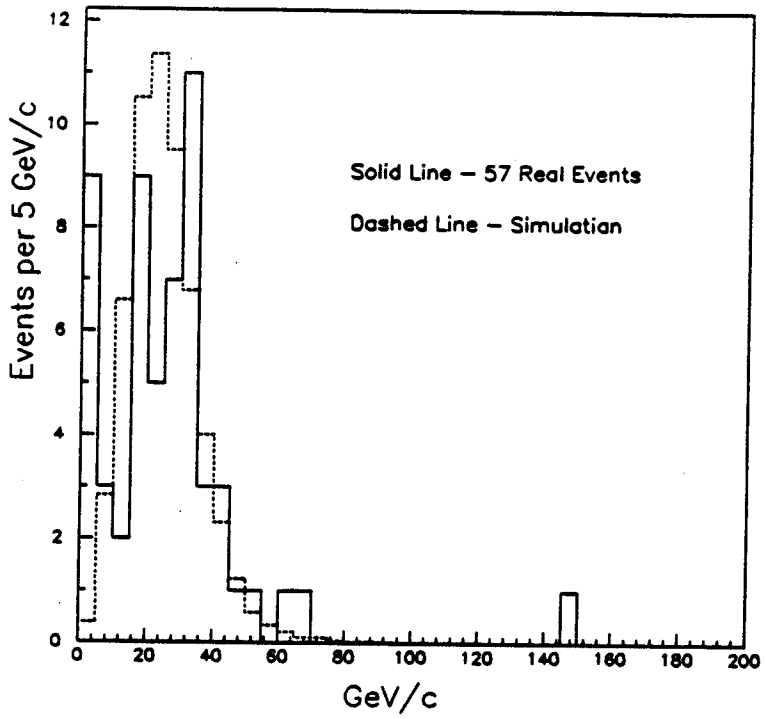

Figure 3.19: P_t spectrum of forward muons in monte carlo without extra hits simulation compared to real data.

hit combination within a 300% road gave the lowest χ^2. The simple detector simulation used in this analysis did incorporate the FMU chamber resolution and survey errors, but it did not simulate the δ–ray effect. Figures 3.19 and 3.20 show that while the mass and P_t^{fmu} spectra produced by this simulation agree well with those of the data in the peaks, there are considerable discrepancies in the low end tails.

These figures show that the number of mismeasured Z^0's is difficult to predict with this simualtion. However, one can try independently to obtain estimates of

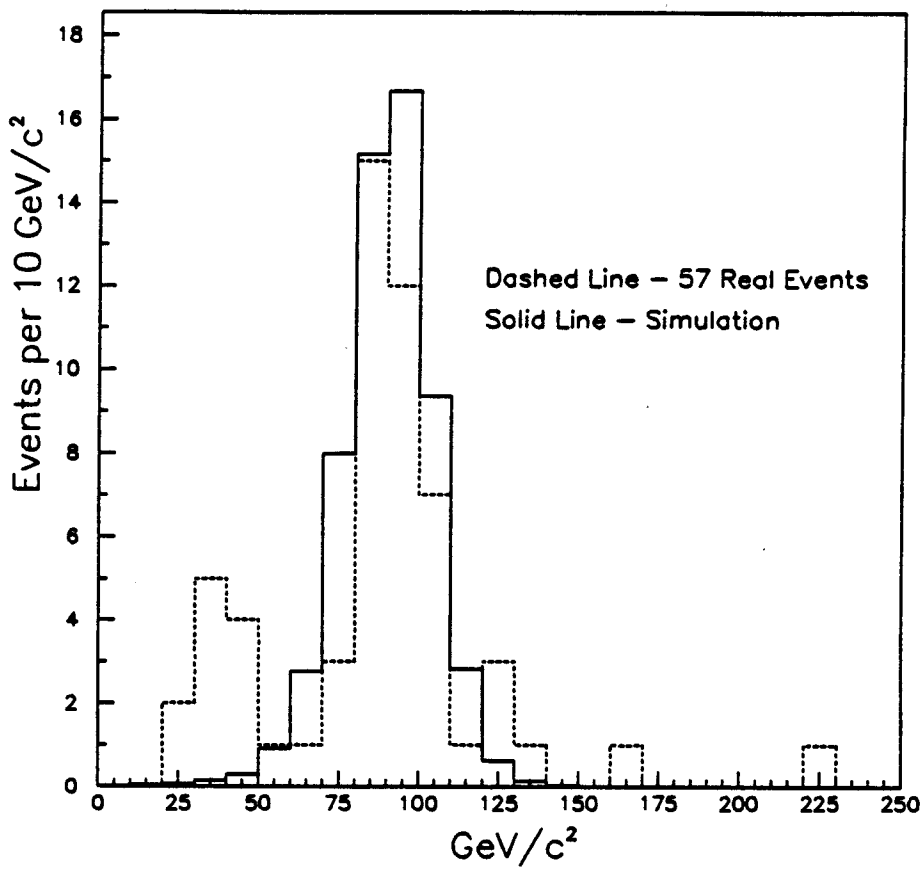

Figure 3.20: Invariant Masses of forward-central dimuons from monte carlo compared to real data.

the number of events in categories 2 and 3. The total events in category #1 must be the excess of events remaining when those expected in categories 2 and 3 are subtracted. The approach taken to estimating the number of mismeasured Z^0's in the mass range $20 - 60 GeV/c^2$ was therefore to estimate the number of events expected in this mass and P_t range due to known measurement effects, such as survey errors and chamber resolution, and the number of events which are muon W's with a spurious or background fmu tagging along. The difference between the number of events in these two categories and the total number of events in that mass range is the number of Z^0's lost by mismeasurement of the forward muon P_t. Monte carlo data was used to obtain an estimate of the number of Z^0 and Drell-Yan pairs one would legitimately expect to have FMU $P_t < 10$ GeV/c and mass< 60 GeV/c^2. The simulated sample consisted 21,899 Monte Carlo forward–central Z^0 and Drell–Yan events generated in the mass range 20 to 150 GeV/c^2 and put through the same simulation used in the acceptance calculation. The muons momenta were smeared by amounts consistent with detector resolution and propagated to the detectors. One muon in the pair was required to satisfy all requirements for a good CMUO, described above, and the other to point into forward muon chambers in the pseudo-rapidity range $1.96 <| \eta |< 3.37$. The forward muon had no P_t requirement. Of the 21,809 events passing the simulation requirements,

- 19,781 had $P_t^{fmu} > 10$ GeV/c and mass> 60 GeV/c^2 (90.7%).

- 796 had $P_t^{fmu} < 10$ GeV/c and mass> 60 GeV/c^2 (3.6%).
- 440 had $P_t^{fmu} > 10$ GeV/c and 20 <mass< 60 GeV/c^2 (2.0%).
- 792 had $P_t^{fmu} < 10$ GeV/c and 20 <mass< 60 GeV/c^2 (3.6%).

In comparison, the 57 real data events break down as

- 44 had $P_t^{fmu} > 10$ GeV/c and mass> 60 GeV/c^2 ($77 \pm 6\%$).
- 1 had $P_t^{fmu} < 10$ GeV/c and mass> 60 GeV/c^2 ($2 \pm 2\%$).
- 1 had $P_t^{fmu} > 10$ GeV/c and 20 <mass< 60 GeV/c^2 ($2 \pm 2\%$).
- 11 had $P_t^{fmu} < 10$ GeV/c and 20 <mass< 60 GeV/c^2 ($19 \pm 5\%$).

The first and fourth categories show disagreement between the simulation and real data at the 2 and 3 σ level, respectively. This implies

1. there is some effect in the real data, particularly in the events in the mass range $20 - 60$ GeV/c^2, which is not accounted for in the simulation, and
2. that of the 57 FMUO-CMUO events

$$.036 \times 57 = 2.1 + / - 0.3 \tag{3.6}$$

is the number of legitimate Drell-Yan and Z^0 events one would expect to find in the data, with an isolated, high quality CMUO and an FMU of $P_t < 10$ forming a dimuon of mass< 60 GeV/c^2.

The other 9 events in this mass range must be coming from a background which is not simulated by the monte carlo ($W^{\pm}$ + jet, $b\bar{b}$ decay, or $Z^0 \longrightarrow cmu + fmu$ in which the forward muon momentum has been badly mismeasured. One can estimate the level of $W^{\pm}$ + jet background by looking at $W \longrightarrow e\nu + fmu$ events. In a sample of $4.05 \pm .21 pb^{-1}$, there were 25 such events. The distribution of forward muon P_t's, e+FMU invariant mass, 1^{st} coordinate wire number of the forward muon, and the opening angle in ϕ between the FMU and the electron are shown in figure 3.21.

Eight of the twenty-five events satisfied the requirements for the central electrons (described in the section on CTC tracking efficiency) that

- $P_t^e \geq 18$ GeV/c
- $ISO < 0.1$,
- LSHR $< .20$
- E/P < 1.5
- $| \Delta x | < 1.5$ cm.
- $| \Delta z | < 3.0$ cm.
- $\chi^2_{strip} < 15$.

The eight also satisfied the FMU requirements:

- $E^{fmu}_{had} + E^{fmu}_{em} < 20$ GeV.

- first forward muon coordinate wire> 9.

- No jet of $E_t \geq 10$ GeV with a 10° cone of the forward muon.

Seven of the eight had $P_t^{fmu} < 10$ GeV/c. Also, the elctron acceptance at CDF is 1.9 times that of the muons. Correcting for the different acceptances and luminosities of the muons and electrons, one would then expect

$$7 \div 1.9 = 3.7 \pm 1.4 \tag{3.7}$$

spurious or background FMUO's among the 12 FMUO-CMUO events which have $P_t^{fmu} < 10$ GeV/c, and also 1 ± 1 background event among the 45 high P_t^{fmu} events. These numbers agree well with the 4 ± 3 and 1 ± 1 events predicted by the like sign pairs in two P_t^{fmu} regions. If one combines the two independent background estimates, one obtains as an estimate for the background 4 ± 1.6 events in the 12 low P_t pairs, and 1 ± 1 for the high P_t region.

3.1.3.3 Fitting Events to the Z Hypothesis

It is also possible to distinguish $W^{\pm}$+ background FMU events from true FMU-CMU Z^0's by a method in which one assumes that the measured azimuthal and polar angles of the forward muon are correct, but that its momentum is unknown. One then writes two equations for FMU momentum in terms of the central muon momentum, the missing transverse energy in the event (corrected for the calorimeter energies of both muons), the FMU and CMU azimuths and polar angles, and the mass of the Z^0 (constrained to 91 GeV/c^2. These two

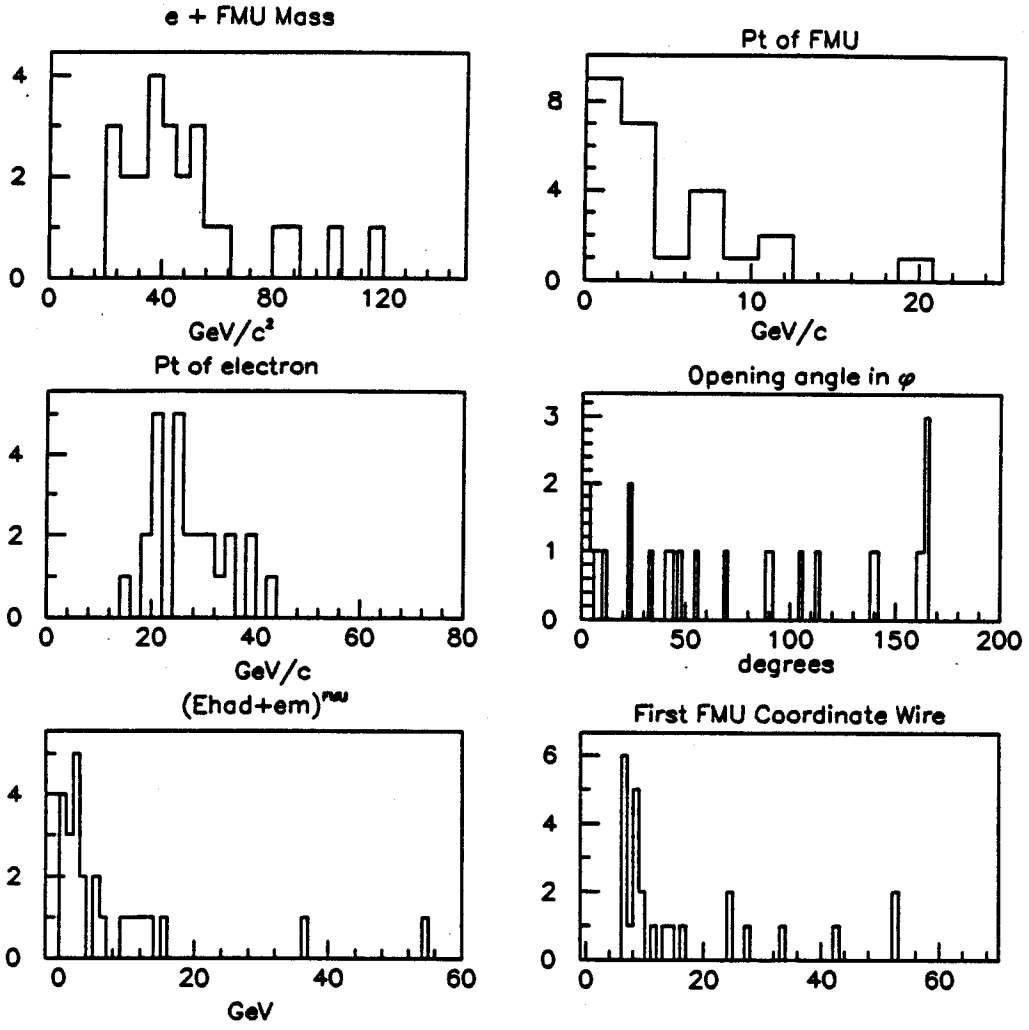

Figure 3.21: Various forward muon and electron parameters for 25 e+FMU events found in the central electron $W^{\pm} \longrightarrow e\nu$ sample.

equations, and their associated errors can be used to fit the events to the Z hypothesis. One calculates a most probable value of the true FMU momentum, and a χ^2 describing the goodness of the fit. Events which are actually central muon $W^{\pm}$+ background FMU can be distinguished from mismeasured Z^0's on the basis of this χ^2. Appendix B contains the explicit calculations of the equations used in this method. For 3 variables with gaussian distributed errors, 99% of the events should have $\chi^2 < 10$. This technique was applied to the 57 FMUO-CMUO dimuons, the central–central Z^0 sample, and to the e+FMU sample. All 42 of the events inside the Z^0 peak (between 60 and 150 GeV/c^2, with $P_t^{fmu} > 10$ GeV/c), can be considered to have their momenta well-measured by the FMU chambers. Eleven of the remaining 15 of the pairs had $\chi^2 < 10$. Calculating the values of the most probable FMU momentum and the corresponding χ^2's (see Appendix B) for the 42 FMUO-CMUO Z^0 candidates yielded the distributions of figures 3.22 and 3.23. Also shown is the distribution of measured momenta for these events. Figure 3.22 shows that the predicted values of momenta for the 42 FMUO-CMUO Z^0 candidates are quite consistent with those measured. Next, the same technique was applied to the 15 FMUO-CMUO events rejected by the forward muon P_t cut and the $60-150$ GeV/c^2 mass window, and to the 25 e+FMUO events. The same jet and calorimetry isolation, and coordinate wire requirements were made on the FMUO in the e+FMU pairs as in the 15 low mass and/or low P_t^{fmu} FMU-CMU's. This reduced the number of e+FMU's to eight. Eleven of the fifteen FMU-CMU's and two of the eight e+FMU events

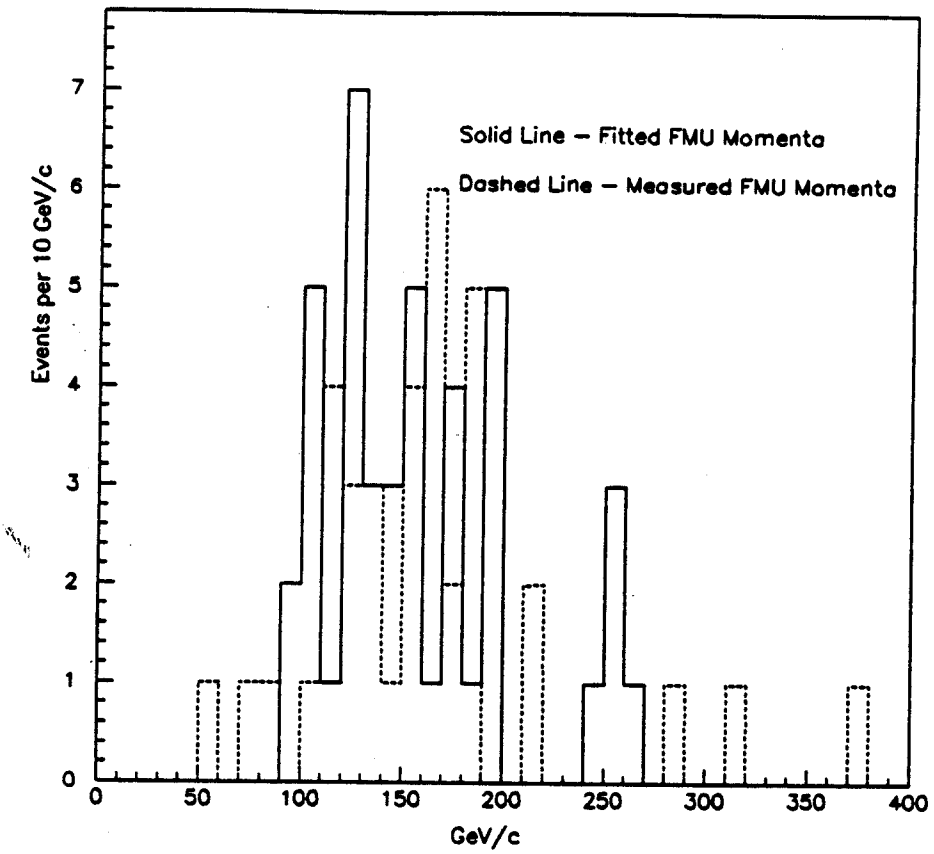

Figure 3.22: Momenta of the forward muon predicted by fitting 42 FMUO-CMUO Z^0 Candidates to the Z^0 hypothesis. Dashed lines show the measured values of FMU momentum.

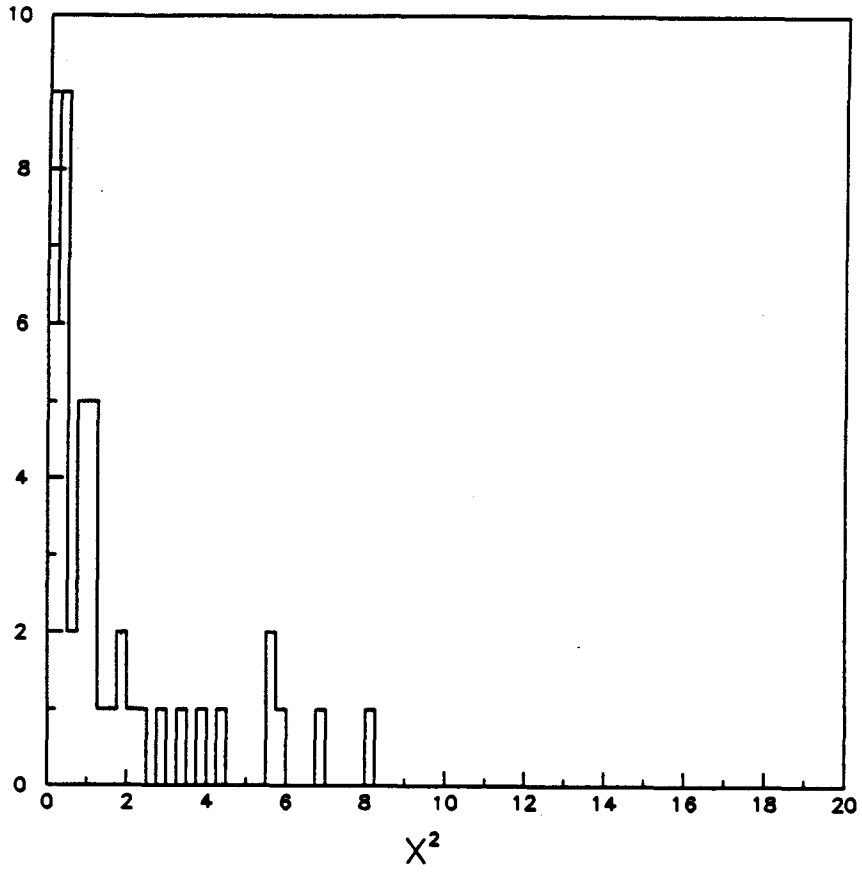

Figure 3.23: χ^2 distribution of 42 FMUO-CMUO Z^0 candidates fitted to the Z^0 hypothesis.

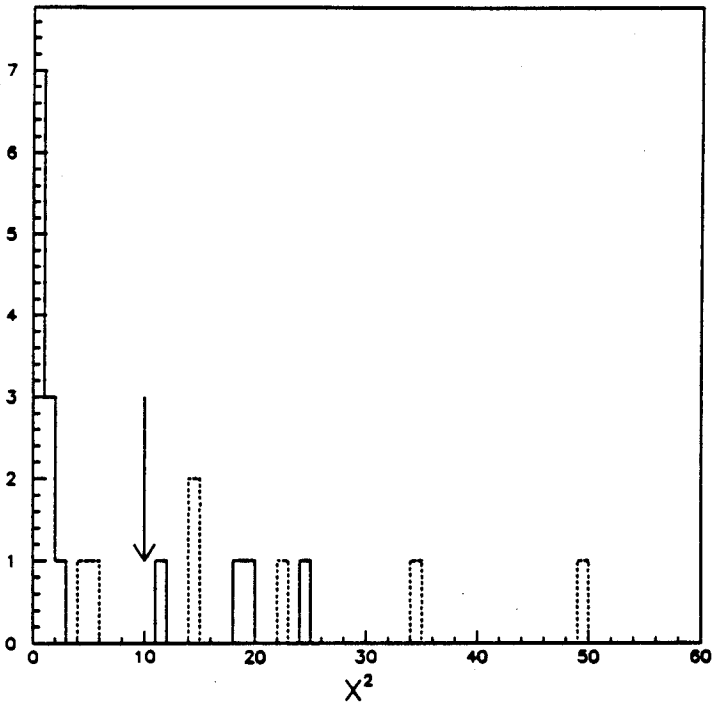

Figure 3.24: χ^2 distributions for 15 FMUO-CMUO dimuons and 8 e+FMU pairs fitted to the Z^0 hypothesis. Arrows indicate the χ^2 cut. The e+FMU pairs are shown in dashed lines.

had $\chi^2_{zfit} < 10$. These distributions are shown in figure 3.24. There is one event among the eight e+FMU's with $\chi^2_{zfit} \sim 500$, which not shown in figure 3.24. Figure 3.25 shows the opening angles in ϕ between the FMU and the other leg of the lepton pair for the eleven FMU-CMU and two e+FMU events surviving the χ^2 cut. Notice that the FMU-CMU distribution is strongly peaked at 180°, while neither e+FMU event is near 180. Figure 3.26 shows the distribution of missing E_t for these same events.

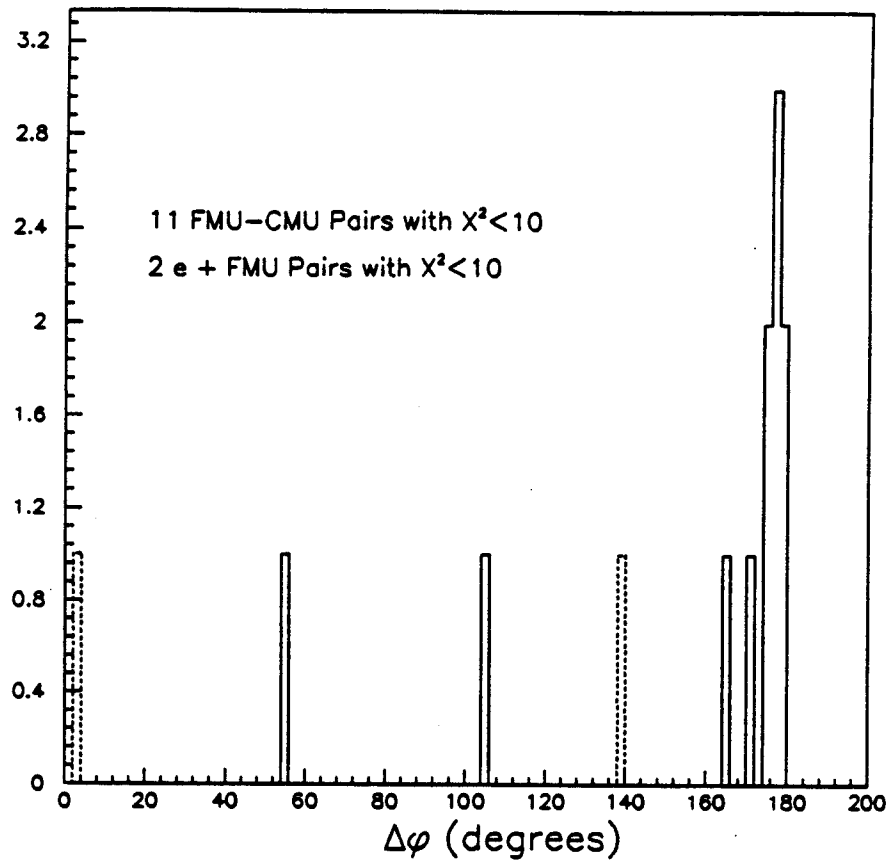

Figure 3.25: Opening angles in ϕ between the leptons in the 11 FMU-CMU and 2 e+FMU events having $\chi^2 < 10$. The two e+FMU events are shown in dashed lines.

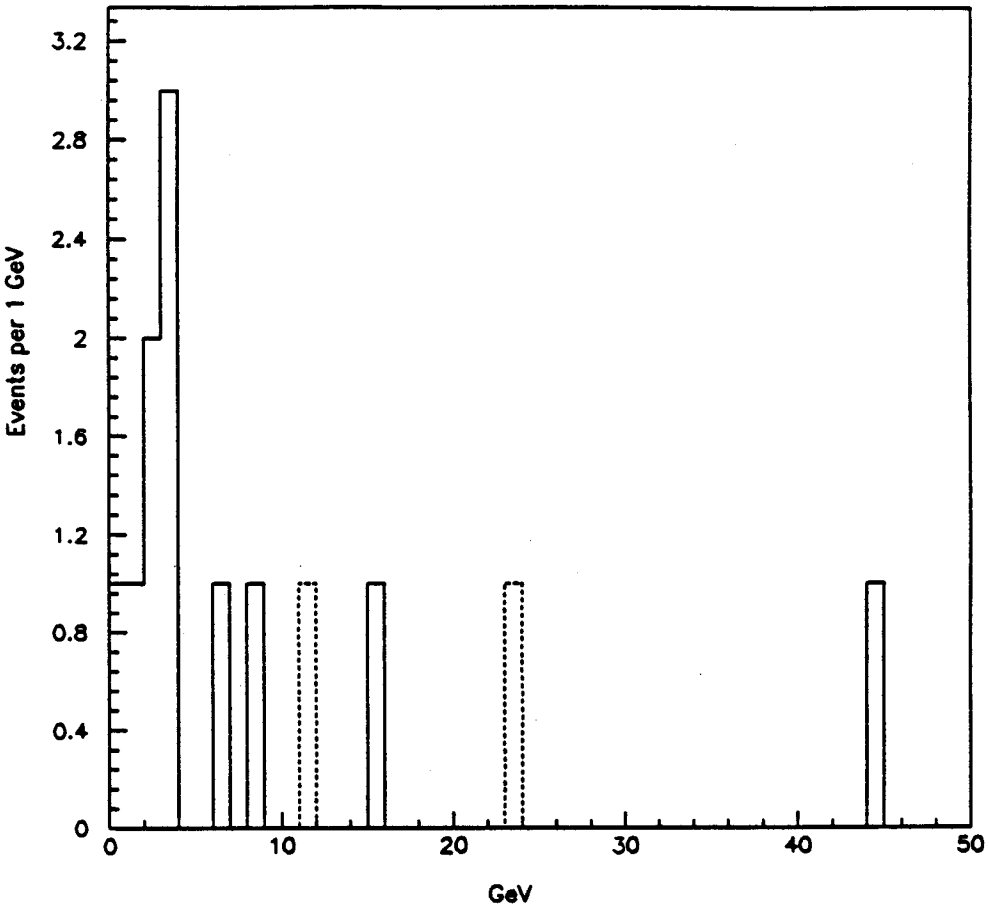

Figure 3.26: Event missing E_t for the 11 FMU-CMU and 2 e+FMU events having $\chi^2 < 10$. The two e+FMU events are shown in dashed lines.

Moreover, both surviving e+FMU events have $P_t^{fmu} < 10$ GeV/c. In terms of the background to the FMU-CMU samples, these results imply that there are:

- 0 background events among the 42 Z^0 candidates in the mass range 60−150 GeV/c^2, with $P_t^{fmu} > 10$ GeV/c.
- $2 \div 2 = 1 \pm 0.75$ background events among the 11 FMUO-CMUO events failing the P_t^{fmu} cut and/or outside the $60 - 1$ GeV/c^2 mass window, and with $\chi^2_{z fit} < 10$.

The eleven potential mismeasured Z^0's were hand-scanned. Two events were rejected as having fake forward muons recontructed using spurious hits. These two events are the same two FMU-CMU's in figures 3.26 and 3.25 which have the largest missing E_t and smallest opening angles in ϕ with the central muon, which strongly inplies that they are both background FMU's in W decay events. These two events fail a cut on the azimuthal opening angle between the CMUO and FMUO of 105°. Two background events are consistent with the estimate of 1 ± 1 event given by fitting procedure using the e+FMU data. To test the robustness of the method, it was also applied to the 146 central-central Z^0 candidates. The distributions of fitted χ^2's and predicted versus measured momenta for these pairs are shown in figures 3.28 and 3.27.

Agreement between the predicted momenta and the measured is quite close, as expected from the high resolution of the Central tracking chambers. Five events fail the $\chi^2 < 10$ requirement, or 3% of the total central-central sample.

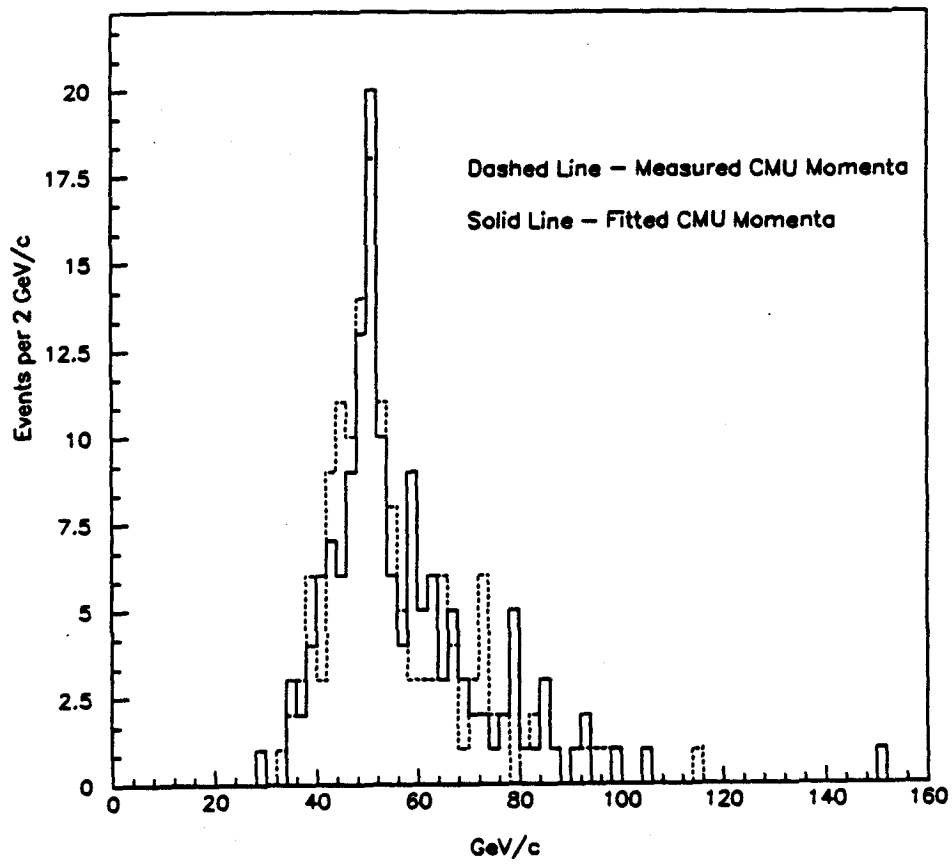

Figure 3.27: Momenta of the central muon (or CMIO) predicted by fitting 146 CMUO-CMUO and CMUO-CMIO Z^0 Candidates to the Z^0 hypothesis. Dashed lines show the measured values of CMU momentum.

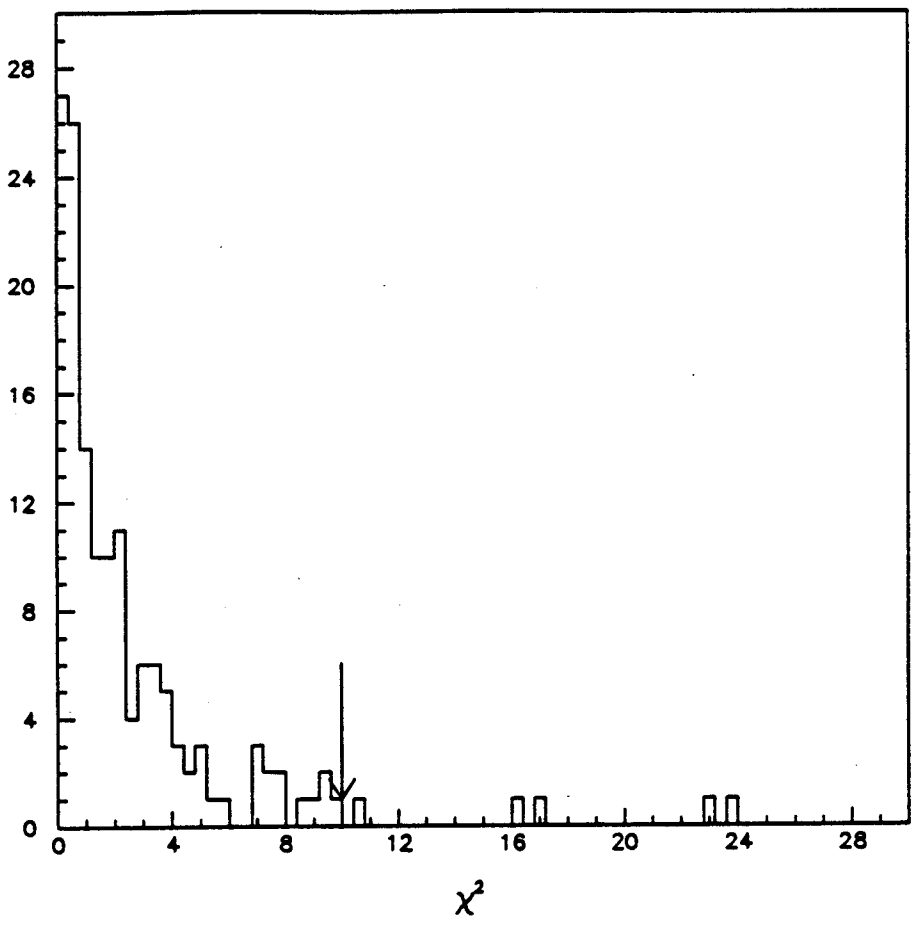

Figure 3.28: Distribution of χ^2 resulting from fitting 146 CMUO-CMUO and CMUO-CMIO Z^0 Candidates to the Z^0 hypothesis.

	Like Sign	$W \longrightarrow e\nu$	Fitted $W \longrightarrow e\nu$	Average
42 Z^0 Candidates	0 ± 1	0 ± 1	0 ± 1	0 ± 1
15 low mass and/or low P_t dimuons	6.0 ± 3.5	4.2 ± 1.5	—	5.1 ± 2.7
11 low mass, and/or low P_t fitted dimuons	4 ± 2	—	1 ± 1	2.5 ± 2.2

Table 3.3: Summary of FMU-CMU background results.

Since the errors in the tracking are quite small, uncertainties in the errors on the calorimeter energies dominate the χ^2 calculation. It is believed that flucutuations in the size of these errors over the whole detector are responsible for the five events (3% of the total sample vs 1% predicted) which fail the $\chi^2 < 10$ cut. Table 3.3 summarizes the results of the various background calculations: It was decided to proceed with the asymmetry analysis, using two forward central data samples:

1. 146 central central Z^0 candidates + 42 well-measured FMUO-CMUO candidates with 0 ± 1 background events.

2. 146 central central Z^0's +42 well-measured FMUO-CMUO's using the fitted momenta for the forward muon, +9 mismeasured FMUO-CMUO Z^0 candidates satisfying $\chi^2_{Zfit} < 10$ and $\mid \phi_{CMUO} - \phi_{FMUO} \mid > 105°$.

Sample #1 was used to obtain the final results for the asymmetry and $\sin^2\theta_W$

which are quoted at the end of this thesis.

3.1.3.4 Multiple Hits in the FMU Chambers

Given the frequency of the phenomenon of delta rays in the FMU chambers, and its potential for affecting the yields of FMUO–CMUO Z^0's, it is important to understand the extent to which it affected the measurement of the momentum and charge of tracks in the FMU system. The presence of like sign pairs in a sample of Z^0 candidates would normally be an indication of background. However, this is no longer true if there is a detector effect which can result in charge mismeasurement for one of the tracks. The background in the 42 FMUO–CMUO Z^0 candidates with $P_t^{fmu} > 10$ GeV/c and $60 < mass < 150$ GeV/c^2 has already been estimated to be 0 ± 1 event using the $W \longrightarrow e\nu$ sample. The absence of like sign pairs is consistent with this estimate, and is, for these events, also a good predictor of the background. There is, however, as has been shown in previous sections, an excess of low P_t^{fmu} events in the FMU-CMU dimuon sample, which is not reproduced by the simulation. Nine events have been identified in section 1.1.3.3 as likely Z^0's whose forward muon momentum has been drastically mismeasured due to some effect in the FMU system. Among these are two like sign pairs, implying that, in some cases, the charge may be mismeasured by the FMU system. As mentioned in section 1.1.3.2, there are several phenomena which could affect the reconstruction, and which are not modelled by the simulation. Among these are random background, multiple hits in the FMU chambers from either

δ-rays or radiation processes accompanying the muon itself, or missing hits, since the reconstruction code allows 5/6 as well as 6/6 hit tracks. This section will describe the results of a study aimed at determining the extent to which extra hits in the FMU chambers result in either charge mismeasurement, or in a drastic mismeasurement in FMU momenta. As stated previously, the forward muon track-finding code fits all possible 5 or 6 hit combinations of hits within a 300% road and selects as the 'correct' one that which gives the lowest χ^2. To investigate the possibility that fitting extra hits resulted in charge and/or momentum mismeasurement, all of the possible fits considered by the FMU tracking code for each of the forward muons in the sample of 57 FMUO–CMUO dimuons were searched for alternate tracks which used hits different from those used in the lowest χ^2 fit, OR which changed sign. The possibility that mismeasurement could have been the result of 'missing' hits, (i.e. fitting a 5/6 hit rather than a 6/6 hit track) was also examined in this way. Of the 57 forward muons in these events, the FMU tracking code was able to fit 52 of them with one or more alternate segments (of higher χ^2). The events which were interesting were the ones which had alternate solutions, and which, for a small change in χ^2, either

- changed charge sign, or
- had a large change in P_t, particularly if such a change pushed it across the 10 GeV/c cut for the forward muons.

3.1.3.5 Momentum Mismeasurement Due to Multiple Hits

Figure 3.29 shows the distribution of P_t change for all the alternate segments for which the χ^2 change was less than 10. The are 30 events in the plot, most of which contributed more than one alternate segment. There is a strong peak near 0, and a few events scattered out to large δP_t. Since the final forward-central dimuon sample has a cut at $P_t^{fmu} > 10$ GeV/c, the interesting alternate segments are the ones which move the event across this line, either into, or out of, the final set. There are eight such events in the plot, three which move below 10 GeV/c, and five which move above. These events are listed in table 3.4, with the χ^2 and P_t of the chosen fit, the χ^2 and P_t of the next lowest χ^2 track which crosses the 10 GeV/c cut, the number of extra hits along the track, and the number of hits used in the chosen fit. Five events flagged by the ZFIT routine as potential Z^0's are in this table. There is only one 6 hit track in the table, event 31017, which has 5 extra hits and a dramatic change in P_t: $\chi^2 = 22.3$ for $P_t = 145$ GeV/c, and $\chi^2 = 25.6$ for $P_t = 1.9$ GeV/c. The other 7 events are all 5/6 hit tracks, two of which (30707 and 1471) have no extra hits, and three (3885, 3798, and 10410) which use the same 5 hits for all the alternate solutions. The hit position ambiguity inherent in a 5 hit track can lead to several possible solutions. The remaining three events (54825, 1604, and 31017) do use extra hits in producing the alternate fit. Events 1604 and 54825 are also 5/6 hit tracks. Thus, in the 57 FMU-CMU dimuon event, there are only 3 cases in which the P_t of the forward

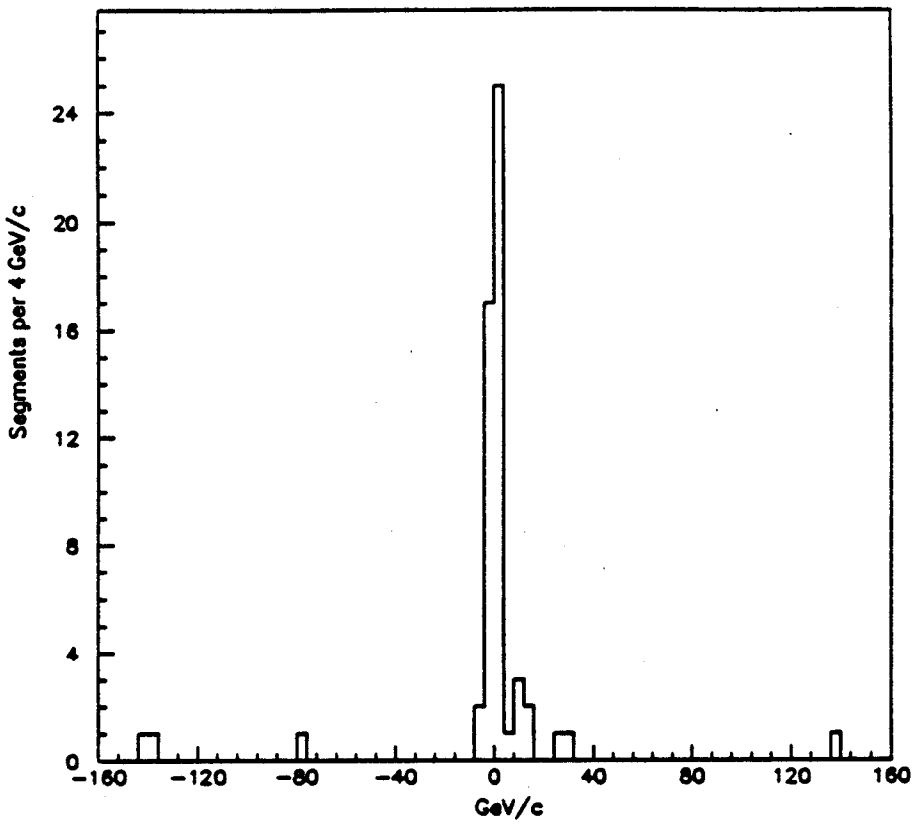

Figure 3.29: $\Delta P_t = P_t^{chosen} - P_t^{alt}$.

Run	Event	P_t	P_t^{alt}	χ^2	χ^2_{alt}	N_{extra}	N_{hits}
19199	54825	4.04	12.57	43.98	46.11	4	5
18055	3798	4.39	12.06	11.12	12.95	1	5
18114	10410	3.23	15.73	9.39	9.63	1	5
19441	1604	61.87	4.89	0.54	3.34	2	5
19103	30707	26.75	7.79	28.38	37.37	0	5
19404	31017	145.54	1.89	22.32	25.64	5	6
17546	3885	10.13	6.39	15.79	16.18	3	5
17798	1471	26.84	8.77	2.97	3.73	0	5

Table 3.4: Comparison of FMU track P_t, and χ^2 with those of the next lowest χ^2 segment.

muon may be mismeasured due to the presence of extra hits along the track. This is a 5% effect.

3.1.3.6 Charge Mismeasurement Due to Multiple Hits

In 13 of the 52 alternate solutions, the alternate fit had a different charge sign than the chosen solution. The momenta, χ^2, P_t, number of hits used and the number of extra hits for the thirteen are shown in table 3.5. Seven events are marked with an *, indicating that the alternate segment used a different set of hits in its fit than did the segment producing the lowest χ^2. Six of these events either have no extra hits, or use the same set of hits for all its fits, so multiple hits are not responsible for any change in charge sign. The 7 remaining events do use different hits in their opposite sign fits, but 5 of these also show increases in χ^2 from 17 through 450(!) over the χ^2 of the chosen fit. It is likely, then, that these five events which fit extra hits in their alternate segments actually used the correct hits to produce the lowest χ^2 track, and that their charge is correctly assigned. If $\chi^2 < 10$ is required as a measure of a likely sign error, then only two events (3885 and 1604) could possibly have had their charge sign mismeasured from the selection of an extra hit. The alternate segments which change sign for these events do use a different set of hits. 3885 and 1604 also appear in 3.4. Moreover, event 3885 was also one of the 9 events identified by the ZFIT procedure as a likely Z^0 candidate. In 57 total events, two potential charge mismeasurements is a $3-4\%$ effect. The results of the studies of alternate segments suggest

Run	Event	P_t	P_t^{alt}	χ^2	χ^2_{alt}	N_{extra}	N_{hits}
19441	1604	61.87	4.89	0.54	3.36	2*	5
19238	57722	41.06	1.82	6.07	23.70	6*	6
19264	24845	29.03	10.88	3.38	94.66	4*	6
19173	9373	16.45	7.96	4.86	113.18	0	5
19199	54825	4.04	37.87	43.98	323.93	4	5
20175	11197	26.13	39.54	5.62	192.84	1	5
17546	3885	10.13	6.39	15.79	16.18	3*	5
17484	1082	3.37	5.44	2.78	151.73	13*	5
18033	29980	17.32	19.15	30.23	41.24	0	5
18098	30219	3.630	562.38	65.79	516.82	6*	5
19829	9699	19.92	5.82	1.44	102.73	3	5
20077	4126	27.18	6.49	4.90	85.97	0	5
17388	4453	54.87	26.75	6.25	23.27	3*	6

Table 3.5: Comparison of FMU track P_t, and χ^2 with those of the next lowest χ^2, oppositely charged segment.

that charge/momentum mismeasurement resulting from fitting the wrong hits is at most a 5% effect for momentum and less than that for misassignment of charge. This is not large enough to account for 9 mismeasured Z^0's. It has been shown that only one of the nine, 3885, could possibly have had its charge sign mismeasured from extra hits. Since seventeen of the twenty-one events in both tables 3.4 and 3.5 are 5/6 hit tracks, it seems quite likely that momentum and charge mismeasurement by the FMU system may be the result of missing hits (from chamber inefficiency) rather than extra hits. Six out of nine of the events identified as mismeasured Z^0's in section 1.1.3.3 are, in fact, 5/6 hit tracks. Two of the nine, 3885 and 2726, are like sign pairs. The alternate segment study leads to an estimate of the extent of charge mismeasurement and/or momentum mismeasurement in the 57 FMU-CMU dimuons of at most $6 \pm 3\%$ (i.e. 3 ± 2 events) due to extra hits. None of the 42 FMU-CMU Z^0 candidates seem to be affected by the delta ray phenomena. At most 1 of the 9 mismeasured Z^0 candidates may be affected by extra hits. It is seems more likely, though, that chamber inefficiency, producing 5/6 hit tracks, is responsible for the bulk of the mismeasurement phenomenon in the FMU system. Neither the delta ray effect nor the 5/6 hit inefficiency is correctly modelled by the current FMU detector simulation. This is an area which merits future in-depth study.

3.2 Efficiency of the Forward Muon Drift Chambers

The overall efficiency of the forward muon drift chambers was determined by comparing the relative %'s of 6/6 hit and 5/6 hit tracks in real data, and convolving the hit-detection efficiency implied by these ratios with the live-time of the FMU system during the 1988-89 run [18]. The live-time of the fmu chambers has been calculated to include the effect of having chambers in the system which were dead or under-efficient for parts of the run due to mis-cabling or bad gas [28]. Both results were calculated taking into account the complete disassembly and re-assembly of the FMU detector in January of 1989 following a catastrophic over-voltaging of the drift chambers by shift personel, which resulted in the destruction of many drift cells. The chambers were dismantled and repaired, but during the re-assembly of the system, the original arrangement of chambers and electronics was not preserved. The original configuration covered run numbers < 18200, and the repaired system took data for run numbers ≥ 18685. The chamber efficiency and livetime calculations were therefore done separately for both sets of run numbers, and for each end (east and west) of the detector. To calculate the individual drift cell efficiency, the relative probabilities for detecting 6/6 and 5/6 hit tracks were used. If one assumes that the probability of a single drift cell in chamber detecting a hit from a passing minimum ionizing particle as ϵ, then the probability, $P_{6/6}$, for each of 6 drift cells in a road to detect a hit from

the passing particle is

$$P_{6/6} = \epsilon^6 \tag{3.8}$$

(assuming that the individual hit probabilities are uncorrelated). The probability for detecting a 5/6 hit track is the probability of 5 hits +1 miss, .i.e.

$$P_{5/6} = \epsilon^5 \times (1 - \epsilon) \times 6 \tag{3.9}$$

Using these two equations to solve for the chamber efficiency

$$\epsilon = \frac{6}{6 + N_5/N_6} \tag{3.10}$$

where N_5 and N_6 are the respective numbers of 5/6 and 6/6 hit tracks in the data sample. ϵ was determined by counting the number of 5/6 and 6/6 hit tracks in all events taken during the 1988-1989 run which contained a forward muon satisfying the following criteria:

- $P_t^{fmu} > 5$ GeV/c.
- $E_{em} > 0.1$ GeV and $E_{had} > 0.9$ GeV, if crossing the plug calorimeters.
- $E_{em} > 0.2$ GeV and $E_{had} > 1.5$ GeV, if crossing the forward calorimeters.
- 1^{st} coordinate wire in the FMU track > 33.
- < 17 extra hits surrounding the track.
- χ^2 Probability > 0.02. χ^2 Probability describes the comparison of the χ^2 of the FMU track to the normal χ^2 distribution [5].

These cuts and the event selection procedure are described more fully in [28]. ϵ was extracted separately for the east and west ends of the detector from this data for runs< 18200:

- $\epsilon_{west} = .918 \pm 0.10$
- $\epsilon_{east} = .865 \pm 0.16$

and for runs> 18685:

- $\epsilon_{west} = .924 \pm 0.10$
- $\epsilon_{east} = .815 \pm 0.16$

The FMU livetime fractions, ϵ_{live} were determined using the same data sample by studying the variations in raw hit multiplicities on an octant by octant basis over the course of the run. The weighted averages (taking into account the shut-down period) for east and west are shown in table 3.6. The four different sets of run numbers refer to the times when each of four different FMU triggers were in use. This analysis, however, does not require the FMU trigger, and so the data from the pre-18200 runs and post-18865 runs can be combined. The total efficiencies of the system (chamber efficiency $\epsilon \cdot \epsilon_{live}$ for the east and west ends of the FMU detector are

$$\epsilon_{total}^{west} = 0.838 \pm 0.032 \tag{3.11}$$

and

$$\epsilon_{total}^{east} = 0.789 \pm 0.029 \tag{3.12}$$

Runs:	$R15880-R16566$	$R16567-R18199$	$R18865-R18847$	$R18848$-end
ϵ_{live}^{west}	$.787 \pm .060$	$.870 \pm .086$	$.895 \pm .014$	$.937 \pm 0.011$
ϵ_{live}^{east}	$.774 \pm .087$	$.846 \pm .071$	$.621 \pm .009$	$.957 \pm 0.009$

Table 3.6: FMU Live time fractions for the runs covering the 4 FMU triggers used during the 1988-1989 data run.

These two figures were inserted into the Monte Carlo simulation used to determine the acceptance of the FMU-CMU pairs.

3.3 Acceptance

The kinematic and fiducial acceptances were determined using the ISAJET monte carlo, and a simplified detector simulation code which reproduced the geometry of the CDF detector. First, events were generated using the ISAJET event generator [26]. Then, $cos\hat{\theta}$ was histogrammed for all events within the mass window $60-150$ GeV/c^2 for central-forward data, and $75-115$ GeV/c^2, otherwise. Next, the z vertex was smeared with a gaussian centered at 0 and with $\sigma = 30$ cm, consistent with the measured distribution of vertices of $p\bar{p}$ collisions at the CDF detector (Fig. 3.4). The momentum vectors were smeared by an amount consistent with the resolution of the detectors, and propagated from the vertex to the detectors. The smearing of tracks going into the FMU drift chambers, whose

resolution is momentum dependent, was parameterized by the curve shown in Figure 1.20, which takes into account the effects of survey errors and chamber resolution. After the smeared tracks were propagated to the muon detectors, fiducial cuts were made. Tracks in the pseudo-rapidity range $1.4 < |\eta| < 1.95$ were discarded. Events failing the mass, z vertex, and P_t cuts were also rejected. Finally, muon quality cuts were simulated by accepting and rejecting events based on the measured efficiencies shown in Table 3.1. The efficiency of the CTC was set to be 98% for $|\eta| < 1.0$ and 64% for $1.0 < |\eta| < 1.4$, determined from the central electrons. For tracks headed into the FMU chambers, the separate east and west efficiencies of 79% and 84% (described in the prevous section) were used. A second histogram of $dN/dcos\hat{\theta}$ was made from the events passing all of these selection criteria. This histogram was divided by the first histogram described above, to give the $cos\hat{\theta}$ acceptance, bin by bin and is shown in Figure 3.30. The very non-uniform shape of the acceptance distribution is due to the many gaps in the muon coverage (phi cracks, 90° crack, the gap in η coverage in the range $1.4 < |\eta| < 1.95$, and the constraint that one muon of the pair always lay in the good fiducial region of the central muon chambers, i.e. $0.04 < |\eta| < 0.61$. Figure 3.31 shows the ratio of CMUO-CMIO pairs as a function of η to total CMUO-CMUO pairs for both the acceptance monte Carlo and the real data. The source of part of the divergence is the uncertainty of the CTC track-finding efficiency for large η. However, the monte carlo ratio actually begins to diverge from that of the real data in the region of the CMU chambers themselves ($0.04 < |\eta| < 0.61$).

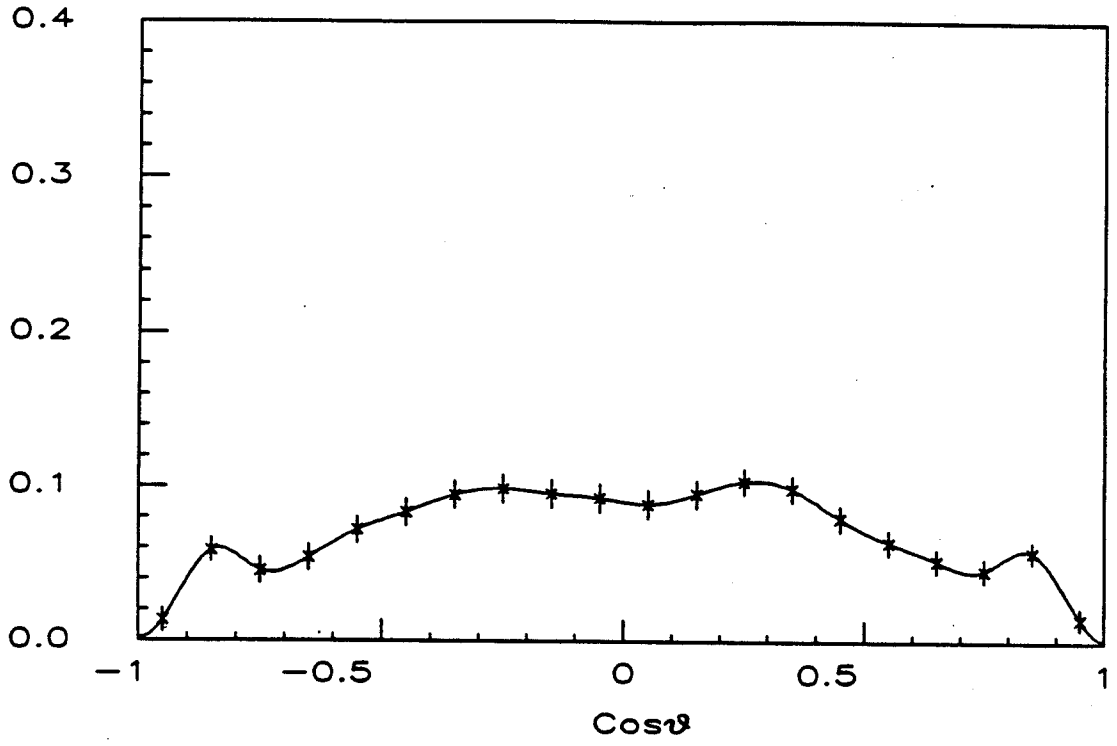

Figure 3.30: The CDF Muon Acceptance as a function of $cos\hat{\theta}$.

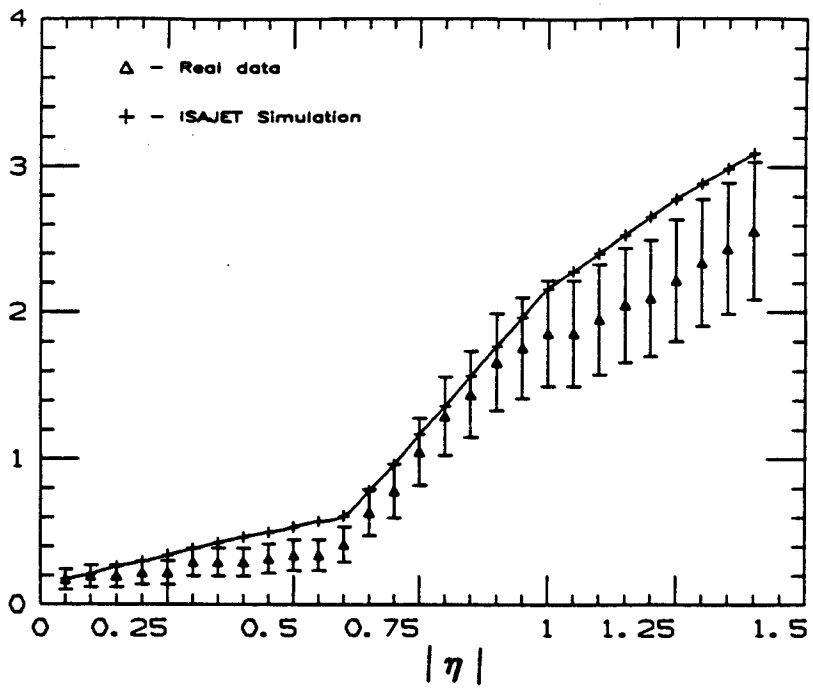

Figure 3.31: The cumulative ratio of CMUO-CMIO pairs to total CMUO-CMUO pairs versus $|\eta|$.

This difference propagates across the whole η range used in the analysis, and enhances the divergence, at large η, due tothe CTC uncertainty. In the η region of the CMU chambers, all CMUO-CMIO pairs consist of dimuons in which one leg has gone into one of 24 ϕ cracks, (refer to figure 1.3 of chapter 2), or into the chimney (a single CMU wedge fore-shortened in z to allow access to the solenoid and other hardware below). These last two CMUO-CMIO categories comprise a small amount of the data ($\sim$ 10%), but the ϕ cracks are each 3° wide and hence account for 20% of the total ϕ coverage in that η region. Table 3.7 shows the

Event Category	Real Data	Simulation
CMUO-CMUO	41 ($71 \pm 6\%$)	3157 (62%)
CMUO-ϕ crack	7 ($12 \pm 4\%$)	1495 (29%)
CMUO-90° crack	9 ($16 \pm 5\%$)	426 (8%)
CMUO-chimney	1 ($2 \pm 2\%$)	38 (1%)

Table 3.7: Break-down of central-central dimuon data into CMUO-CMUO and CMUO-CMIO pairs for the real data and for the acceptance simulation.

breakdown of dimuon pairs in to CMUO-CMUO and CMUO-CMIO types for both the real data and the monte carlo, in the eta range $\mid \eta \mid < 0.61$, along with the % of the total data in that η region each category comprises. It is apparent that the monte carlo does not reproduce the % of CMUO-ϕ crack pairs which is present in the real data. The simulation, in fact, behaves as if the azimuths of the two muons were almost completely uncorrelated. In such a case, then, if the ϕ cracks reduce the CMU ϕ coverage to 80%, then the probability of seeing a CMUO-CMUO pair in the detector is

$$0.80 \cdot 0.80 = 0.64 \tag{3.13}$$

or 64%, and the probability of getting a CMUO-ϕ crack event is

$$0.80 \cdot 0.20 \cdot 2 = 0.32 \tag{3.14}$$

or 32%. Thus, the ratio in the data of CMUO-CMUO to CMUO-ϕ crack events would be $64 \div 32 = 2$ to 1, which is the same ratio as the ISAJET based monte carlo produced. In the real data, the effects of multiple scattering and the magnetic field on the muons should tend to reduce the ϕ correlation, but their effects are small for muons in the relevant momentum range ($\sim$ 50 GeV/c).

The source of the difference between the real data and the monte carlo appears to be partly related to the input P_t spectrum of the Z^0 boson in ISAJET. Figure 3.32 show the comparison between the P_t^Z spectra of the real data and the monte carlo. While agreement in the tails is good, the real data peaks at a lower value than does the monte carlo spectrum. Leptons from Z^0's with lower P_t are going to go off more back-to-back in ϕ than those from Z^0's with higher P_t, and hence are going to show a stronger correlation in their azimuths. Figure 3.33 show the difference in ϕ for the two muons in the real data and in the simulation. To test this hypothesis, $Z^0 \longrightarrow \mu^+\mu^-$ events were generated with a fast monte carlo which decays Z^0 into leptons from on the zeroth order diagram, $q\bar{q} \longrightarrow Z^0 \longrightarrow l^+l^-$ [29]. For this process, the Z^0 has zero P_t. The plot of the ratio of CMUO-CMIO:CMUO-CMUO pairs was regenerated with using data from this generator (figure 3.34.

One can see that the agreement between the $P_t^z = 0$ monte carlo and the data is quite good above $|\eta| > 1.0$, though correspondence in this region seems to be helped by the fact that in the region $0.61 < |\eta| < 1.0$, this simulation tends to slightly underestimate the CMUO–CMIO acceptance. The acceptance as a

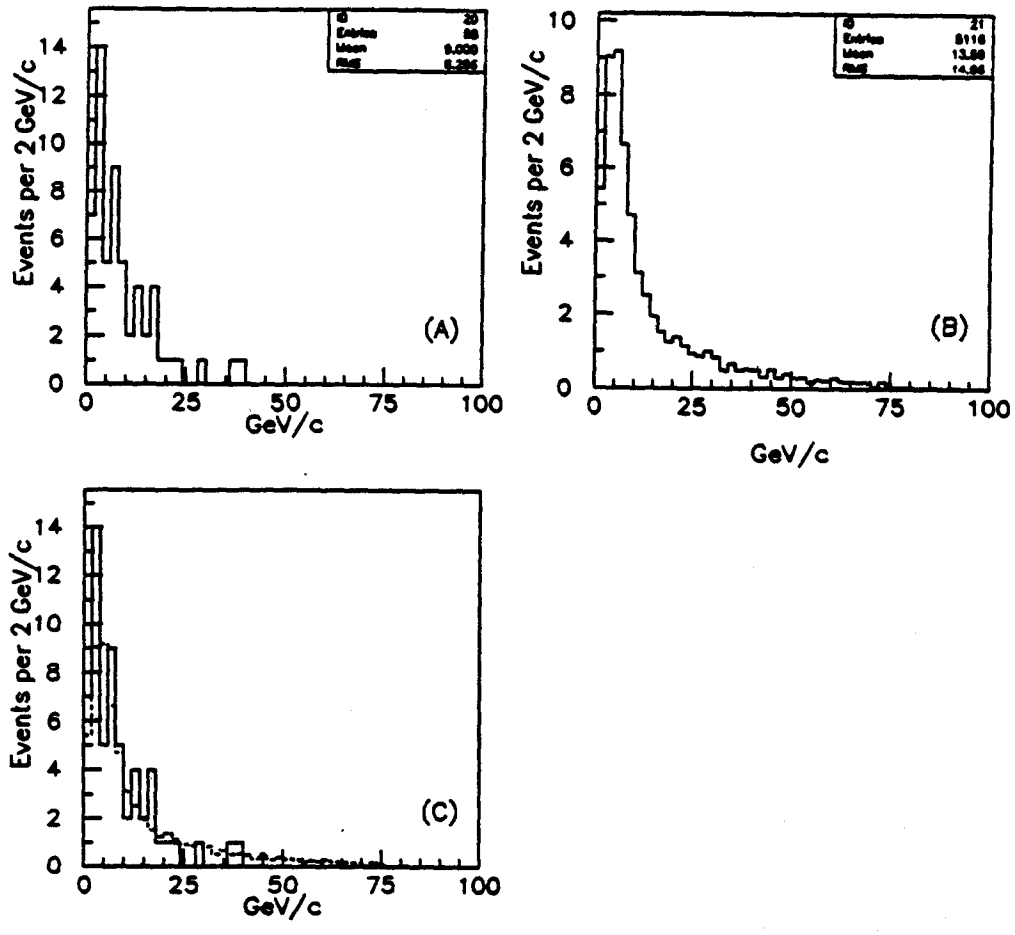

Figure 3.32: (A) real data, (B) simulation, and (C) (A)+(B). The simulated data is shown in dashed lines.

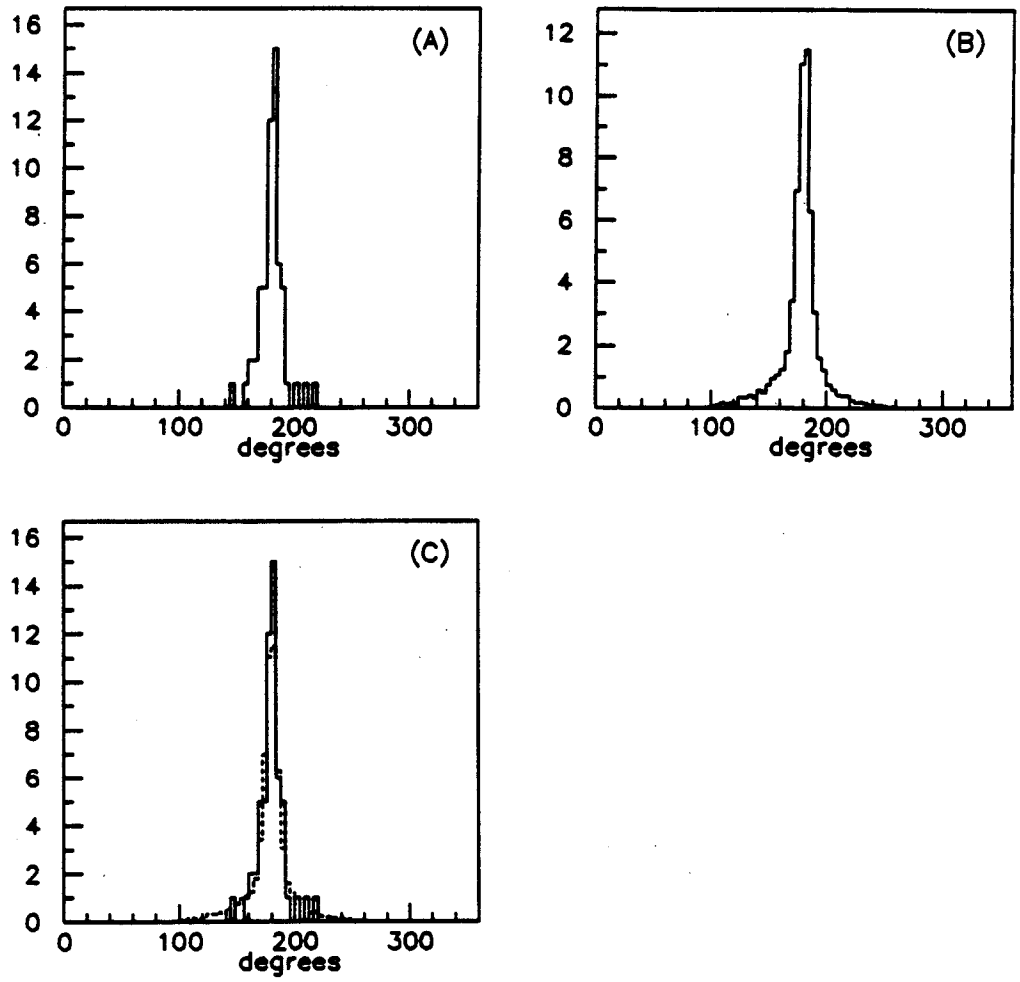

Figure 3.33: $\Delta\Phi = \mid \phi_1 - \phi_2 \mid$ for (A) real data, (B) simulation, and (C) (A)+(B). The simulated data is in dashed lines.

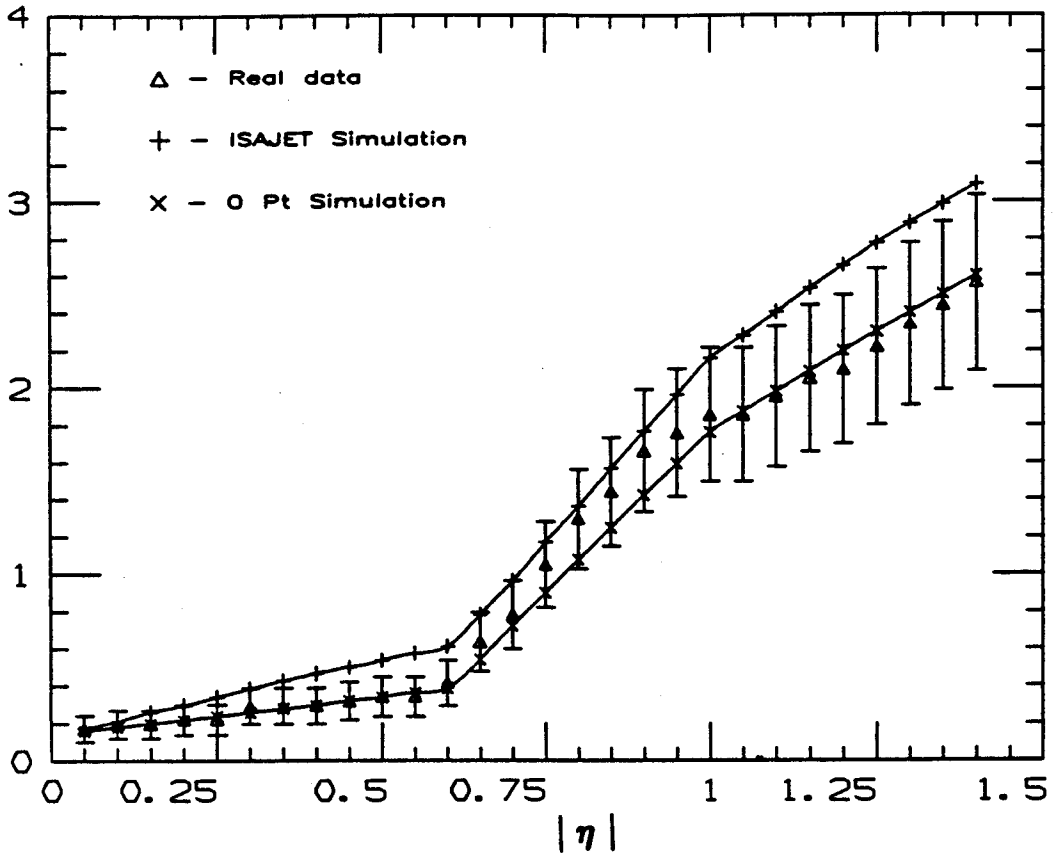

Figure 3.34: The cumulative ratio of CMUO-CMIO pairs to total CMUO-CMUO pairs versus | η | for real data and monte carlo.

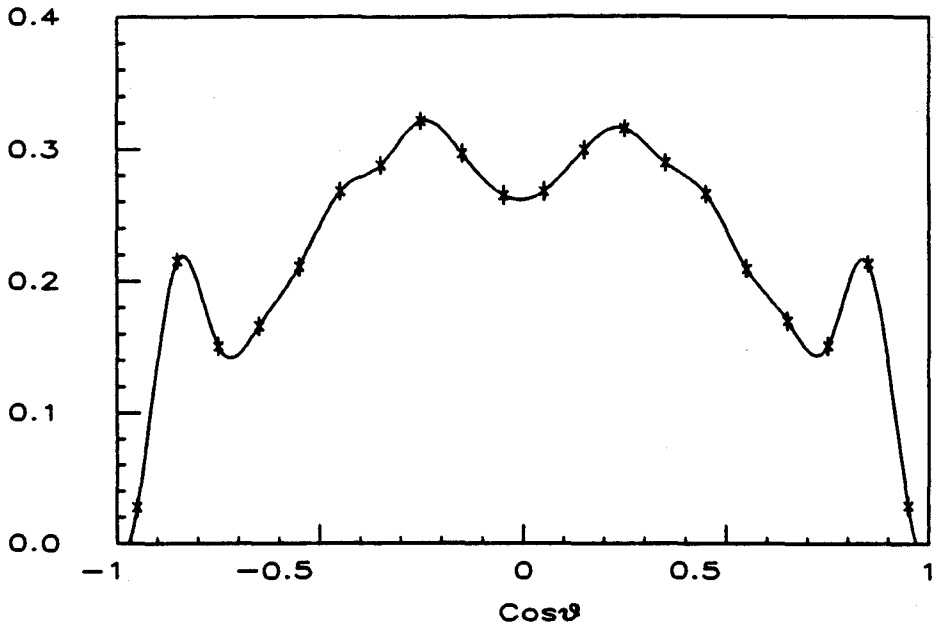

Figure 3.35: $\cos\hat{\theta}$ acceptance produced by a simulation having 0 boson P_t.

function of $\cos\hat{\theta}$ for this monte carlo is shown in 3.35. It seems clear that there is another effect at work here. The break-down of CMUO-CMIO pairs given by the $P_t^Z = 0$ monte carlo is shown in table 3.8.

Since the real data obviously does not feature Z^0's with 0 transverse momentum, the acceptance from such a simulation is not correct, and the agreement with the data is to some extent coincidental. However, there also is obviously a large systematic error in the acceptance done with the best set of corrections which exist. This systematic appears to be sensitive to the input P_t spectrum of the Z^0 boson. It was decided to proceed with the analysis correcting the data with

Event Category	Real Data	ISAJET Simulation	0 P_t^Z Simulation
CMUO-CMUO	41 ($71 \pm 6\%$)	3157 (62%)	12504 (72%)
CMUO-ϕ crack	7 ($12 \pm 4\%$)	1495 (29%)	3025 (18%)
CMUO-90° crack	9 ($16 \pm 5\%$)	426 (8%)	1758 (10%)
CMUO-chimney	1 ($2 \pm 2\%$)	38 (1%)	99 (0.6%)

Table 3.8: Break-down of central-central dimuon data into CMUO-CMUO and CMUO-CMIO pairs.

the acceptance given by each monte carlo, and assigning the difference between the two results as the systematic error due to uncertainties in the acceptance. The ratio of FMUO-CMUO to CMUO-CMUO pairs was given by the ISAJET simulation (using the best set of acceptance corrections) to be

$$4112 \div 3157 = 1.30 \pm .03 \text{ to } 1 \tag{3.15}$$

The real yields are 41 CMUO-CMUO and 42 FMUO-CMUO Z^0's. This ratio of the yields is

$$42 \div 41 = 1.0 \pm .2 \text{ to } 1 \tag{3.16}$$

which is consistent with the simulation to within 1.5σ. If the 9 mismeasured Z^0 candidates from the fitting procedure are added, this ratio improves to:

$$51 \div 41 = 1.2 \pm 0.3 \tag{3.17}$$

which is consistent with the simulation to within 1σ. The uncorrected distributions of $\cos\hat{\theta}$ for the 188 well-measured Z^0 events, and the 9 mismismeasured FMUO–CMUO Z^0 candidates shown in figure 3.36. The many gaps in the muon coverage are responsible for the flatness of the curves. Plots (A) and (B) of figure 3.36 were corrected with the acceptances of figure 3.30 (the best set of corrections extracted from known detector effects) and of figure 3.35, the $P_t^Z = 0$ monte carlo. The corrected samples are shown in figures 3.37 and 3.38. As one can see by comparing the 188 event sample to the 197 event sample, the addition of the 9 events actually tends to pull the observed asymmetry towards even more negative values, even though these events are all probable Z^0's.

The plot of the 188 event sample in figure 3.37 shows an excess of events in the second bin. Given that the background studies (described in previous sections), including the absence of like sign pairs in the data, indicate that the background in the 188 event sample is on the order of 1 ± 1 event, this excess in bin #2 must be attributed to statistics. Of the 9 mismeasured Z^0 candidates, 3 have $\cos\hat{\theta} > 0$ and 6 have $\cos\hat{\theta} < 0$, resulting in an asymmetry of $-33 \pm 16\%$ for these events. The background among the 9 is $\sim$ 2 events.

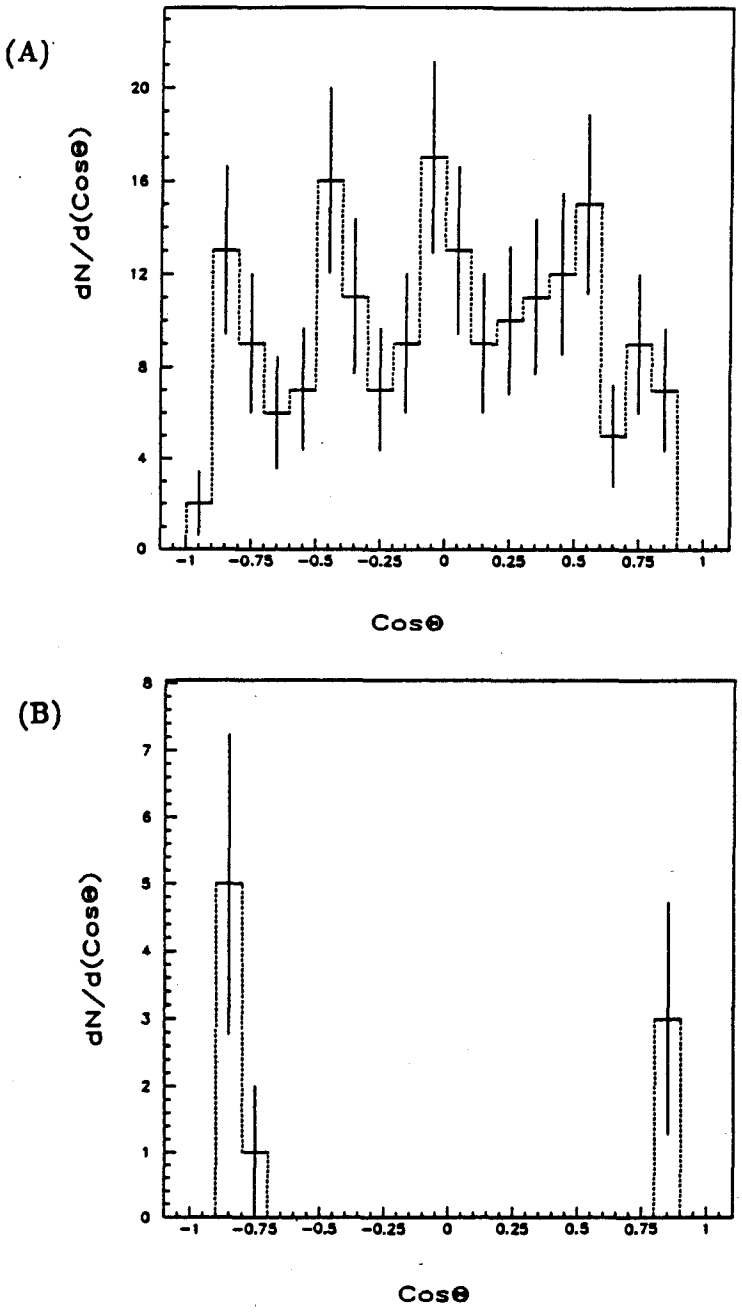

Figure 3.36: (A)Uncorrected $\cos\hat{\theta}$ for 188 Z^0's. (B) Uncorrected $\cos\hat{\theta}$ for 9 mismeasured FMU-CMU Z^0 candidates.

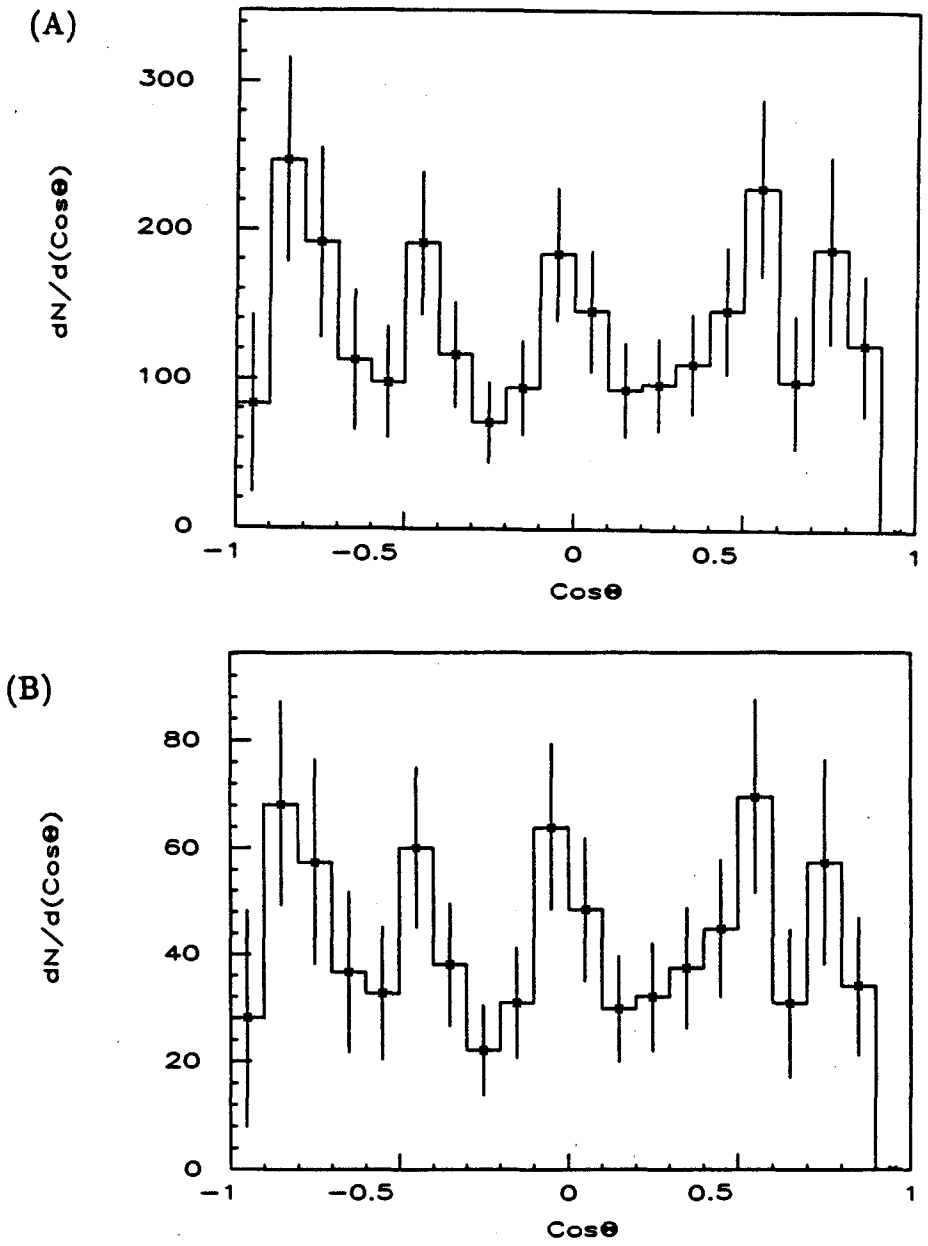

Figure 3.37: $\cos\hat{\theta}$ distribution for 188 Z^0 candidates, (A) acceptance-corrected with known detector effects. (B) corrected with the zeroth order monte carlo.

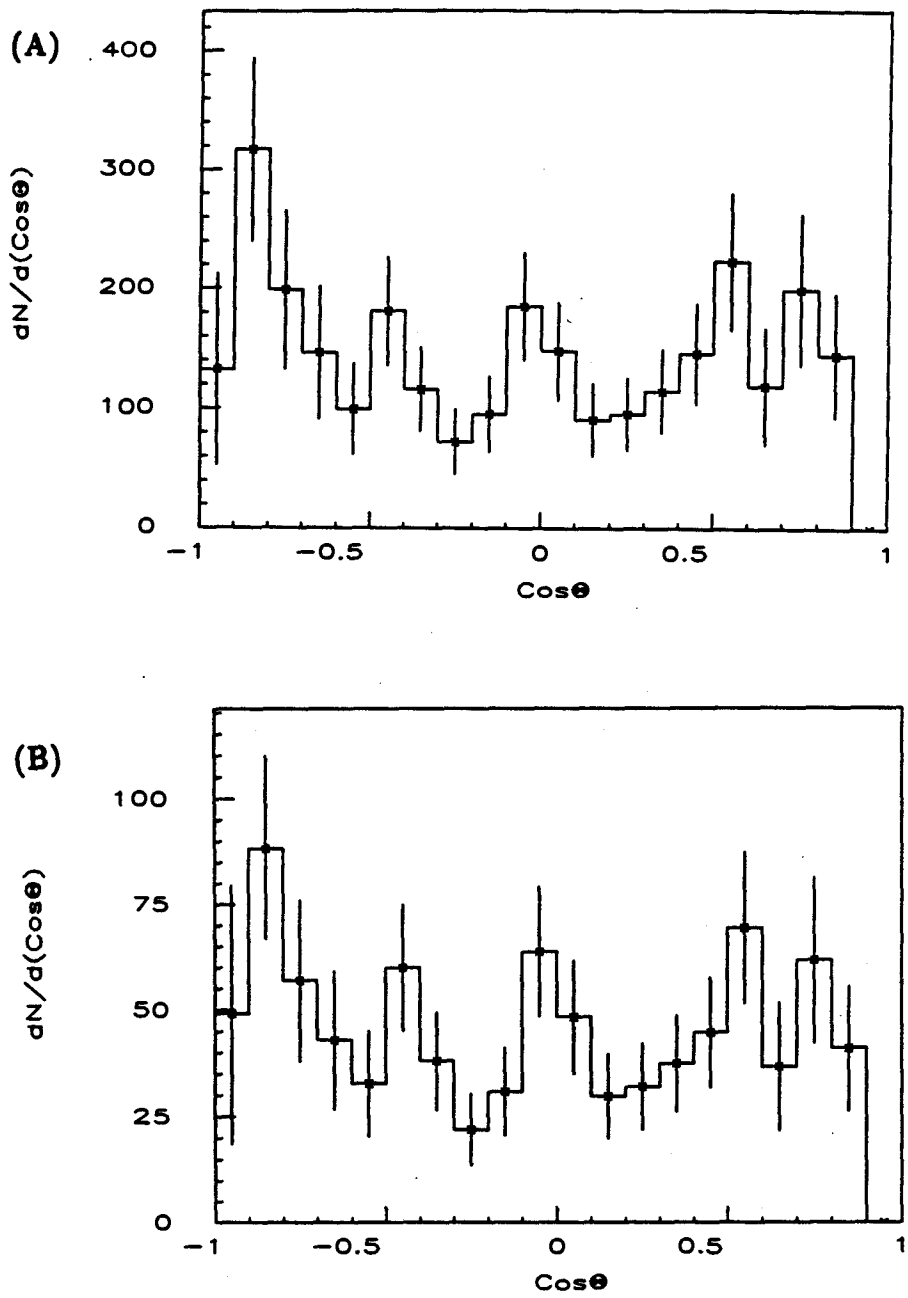

Figure 3.38: (A) $\cos\hat{\theta}$ distribution for 197 Z^0 candidates, acceptance-corrected with known detector effects. (B) corrected using the $P_t^Z = 0$ monte carlo.

Chapter 4

Analysis

The forward-backward asymmetry, A_{fb}, and the Weinberg angle, $\sin^2\theta_W$, were extracted from the data by fitting the lowest order lepton pair production cross-section to the data distribution of the Collins-Soper angle, $\cos\hat{\theta}$, defined in chapter 2. The equation for the lowest order cross-section, written in detail also in chapter 2 as 2.22, can be grouped into terms of order $\cos^2\hat{\theta}$ and $\cos\hat{\theta}$, and written in the simplified form

$$\frac{dN}{d\cos\hat{\theta}} = A\cdot(1+\cos^2\hat{\theta}) + B\cdot\cos\hat{\theta} \tag{4.1}$$

where, referring back to equation 25, A and B depend on the quark distribution functions, M_Z, Γ_Z, and the Weinburg angle, θ_W. If the cross-section is written in this form, then, referring to equation 28 of chapter 2 for the forward-backward asymmetry, A_{fb}, one finds upon performing the $cos\hat{\theta}$ integrals that

$$A_{fb} = \frac{3}{8}\cdot\beta \tag{4.2}$$

where $\beta \equiv B/A$. The function minimization package, MINUIT [33], was used to minimize both a negative log liklihood function to the data and a χ^2 function. The negative log likelihood fit has the advantage of being independent of the acceptance, provided that the acceptance is symmetric in $\cos\hat{\theta}$ (as will be shown). Results from this procedure are thus unaffected by errors in the acceptance, which, in this case, are known to be large. The negative log likelihood method does not, however, provide any measure of the goodness of the fit. The χ^2 fit, while sensitive to systematics in the acceptance, does provide an estimate of the fit quality, and is used as a check on the log likelihood results.

4.1 The Loglikelihood Fit Procedure

In the likelihood approach, the normalized probability function, P, for an event is written in the same way as the simplified cross-section of equation 4.1:

$$P = \frac{3}{8}\left((1+\cos^2\hat{\theta}) + \frac{B}{A}\cdot\cos\hat{\theta}\right) \tag{4.3}$$

To take into account the acceptance of the detector, an acceptance function, $\epsilon(\cos\hat{\theta})$, must be folded into the probability P.

$$P' = \epsilon(\cos\hat{\theta})\cdot N\cdot\frac{3}{8}\left((1+\cos^2\hat{\theta}) + \frac{B}{A}\cdot\cos\hat{\theta}\right) \tag{4.4}$$

where N is a normalization factor chosen such that

$$N^{-1} = \frac{3}{8}\left[\int_{-1}^{1}\epsilon(\cos\hat{\theta})\cdot(1+\cos^2\hat{\theta})d\cos\theta + \int_{-1}^{1}\epsilon(\cos\hat{\theta})\cdot\frac{A}{B}\cos\hat{\theta}d\cos\hat{\theta}\right] \tag{4.5}$$

Clearly, if $\epsilon = \epsilon(\cos^2\hat{\theta})$, i.e. the acceptance is symmetric in $\cos\hat{\theta}$, then the term in 4.5 which contains the asymmetry vanishes. Hence, the normalization, N, is independent of A_{fb}.

Now, the likelihood of a set of i events is given by

$$\mathcal{L} = \prod_{\mathrm{i}} \frac{3}{8} \cdot \mathrm{N}\epsilon(\cos^2\hat{\theta}_{\mathrm{i}}) \cdot \left((1+\cos^2\hat{\theta}_{\mathrm{i}}) + \frac{\mathrm{B}}{\mathrm{A}} \cdot \cos\hat{\theta}_{\mathrm{i}}\right) \tag{4.6}$$

and the negative log likelihood by

$$-\ln\mathcal{L} = -\sum_{\mathrm{i}} \ln\frac{3}{8} \cdot \mathrm{N}\epsilon(\cos^2\hat{\theta}_{\mathrm{i}}) - \sum_{\mathrm{i}} \ln\left((1+\cos^2\hat{\theta}_{\mathrm{i}}) + \frac{\mathrm{B}}{\mathrm{A}} \cdot \cos\hat{\theta}_{\mathrm{i}}\right) \tag{4.7}$$

The dependence on $\sin^2\theta_W$ and A_{fb} of the log likelihood function is contained entirely in the B/A factor. One can minimize equation 4.7 with respect to either β, to get the most probable value of A_{fb}, or with respect to $\sin^2\theta_W$, to determine the best value of that parameter. The term containing the acceptance, ϵ, being independent of $\sin^2\theta_W$ and A_{fb} if $\epsilon = \epsilon(\cos^2\hat{\theta})$, has no effect on the minimization, and so the log likelihood result is independent of acceptance, provided the acceptance is symmetric in $\cos\hat{\theta}$.

4.2 χ^2 Fit Procedure

The χ^2 fit was performed by fitting the angular distribution of equation 4.1 to the binned, acceptance corrected data. The best fit is the one which minimizes the χ^2 statistic defined as

$$\chi^2 = \sum_i \frac{(y_i - y(x_i))^2}{\sigma_i^2} \tag{4.8}$$

where $y(x)_i$ is the contents of the i^{th} bin in the acceptance- corrected histogram of the data, y_i is the value predicted by the angular distribution for the contents of i^{th} bin, and σ_i is the statistical error on $y(x_i)$. The χ^2 fit has two free parameters, which are $sin^2\theta_W$ (or B/A), and the overall normalization of the predicted distribution to the real data. The histogram of $\cos\hat{\theta}$ (see figure 4.1 contains 20 bins. Bins 1 and 20 are excluded from the χ^2 fit. Bin 20 has no data, and the acceptance of bin 1 is disproportionately small compared to the other bins. Eighteen total bins and two parameters result in a χ^2 with 16 degrees of freedom.

4.3 Event-Counting

The forward backward asymmetry can also be calculated directly by event counting:

$$A_{fb} = \frac{N_{\cos\theta>0} - N_{\cos\theta<0}}{N_{\cos\theta>0} + N_{\cos\theta<0}} \tag{4.9}$$

In the sample of 188 Z^0 candidates, there were 91 events with $\cos\hat{\theta} > 0$, and 97 events with $\cos\hat{\theta} < 0$. This implies an asymmetry of $-3.2 \pm 7.3\%$. If one calculates A_{fb} this way from the data, then it is possible to work backwards from the cross-section, using the known values of the quark couplings, to extract directly a value for $\sin^2\theta_W$. These results are presented in the following section.

Forward-Backward Asymmetry Results		
Measurement Method	A_{fb}	ΔA_{fb}
Event-Counting	−0.0337	0.0771
Log likelihood fit		
to β	−0.0334	0.0782
χ^2 fit to β	−0.0166	0.0807

Table 4.1: A_{fb} results using set 1 acceptance corrections and EHLQ1 parton distribution functions for the 188 event Z^0 sample.

4.4 Fit Results

The values of A_{fb} and $\sin^2\theta_W$ extracted from the 188 event data sample using the three measurement methods (loglikelihood fit, χ^2 fit, and event-counting) are shown in tables 4.1 and 4.2. The acceptance corrections used were those of figure 3.30 in Chapter 3, which incorporated all known detector effects. For simplicity's sake, these corrections will be referred to as 'set 1'. The corrections derived from the zeroth order ($P_t^Z = 0$) generator will be referred to as 'set 2'. The fitted results in tables 4.1 use the EHLQ1 set of parton distribution functions. The errors shown are statistical only. The χ^2 fit for the 188 event sample gave $\chi^2 = 17.51$ for 16 degrees of freedom and a confidence level of .3535. The loglikelihood fit to the data is shown in figure 4.1. Next these exercises were repeated with the 197 event sample in which 51 forward-central candidates (42

$\sin^2\theta_W$ Results		
Measurement Method	$\sin^2\theta_W$	$\Delta\sin^2\theta_W$
Event-Counting	0.2506	0.0290
Log likelihood fit	0.2557	0.0251
χ^2 fit	0.2504	0.0246

Table 4.2: $\sin^2\theta_W$ results using set 1 acceptance corrections and EHLQ1 parton distribution functions.

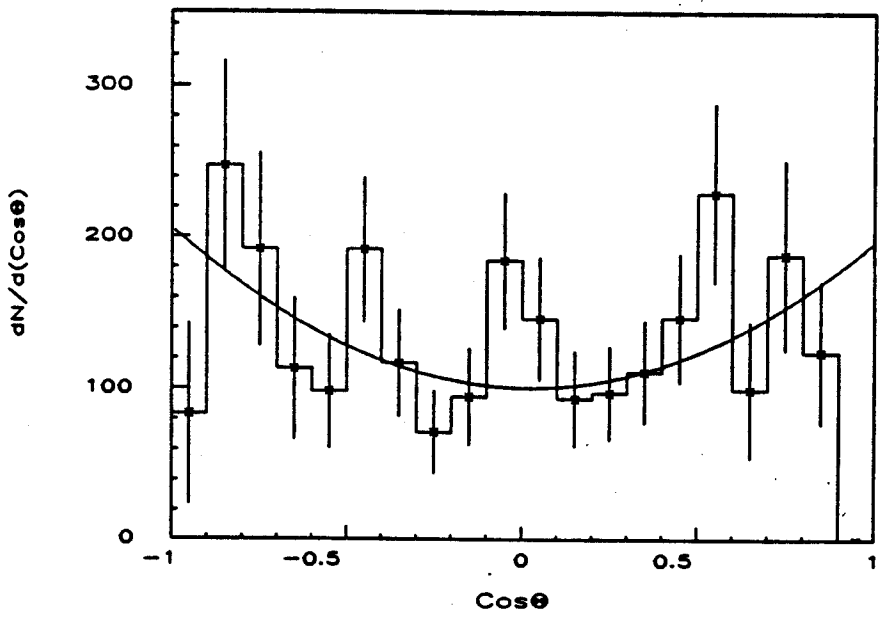

Figure 4.1: Negative Loglikelihood fit to $\cos\hat{\theta}$ distribution of 188 $Z^0 \longrightarrow \mu^+\mu-$ candidates.

Forward-Backward Asymmetry Results		
Measurement Method	A_{fb}	ΔA_{fb}
Event-Counting	−0.0484	0.0753
log likelihood fit		
to β	−0.0529	0.0748
χ^2 fit to β	−0.0244	0.0802

Table 4.3: A_{fb} results for 197 event data sample using set 1 acceptance corrections and EHLQ1 parton distribution functions.

well-measured Z^0's + the 9 mismeasured candidates pickerd up by the Z fitting procedure of section Chapter 3 section 3.1.3.3). All 51 events were constrained to fit the Z^0 mass, 91.1 GeV/c^2. This exercise was performed merely to test whether we gained anything for the asymmetry analysis by the Z^0 procedure. The results are shown in tables 4.3 and 4.4. The χ^2 fit for the 197 event sample gave $\chi^2 = 16.82$ for 16 degrees of freedom and a confidence level of .3975. As one can see, adding events to the sample did not improve quality of the fits, and so these events were NOT included in the fits which produced the results to be quoted at the end of this chapter. Since the 9 events added to the sample largely populate bin 2 of the $\cos\hat{\theta}$ histogram, these events tend to pull the fits even more strongly in the direction of negative asymmetry. As stated before, it is believed that this effect is purely a statistical fluctuation, and that the Z^0 fit procedure is a sound

$\sin^2\theta_W$ Results		
Measurement Method	$\sin^2\theta_W$	$\Delta\sin^2\theta_W$
Event-Counting	0.2574	0.0319
Log likelihood fit	0.2621	0.0258
χ^2 fit	0.2528	0.0250

Table 4.4: $\sin^2\theta_W$ results for 197 event sample using set 1 acceptance corrections and MRSB parton distribution functions.

one. However, the results which will quoted in this analysis were taken from the 188 event sample. The loglikelihood fitted data for the 197 event sample is shown in figure 4.2.

4.4.1 Effects of Acceptance Errors on A_{fb} and $\sin^2\theta_W$

Next, to test the effect of systmatic errors in the acceptance on A_{fb} and $\sin^2\theta_W$, the fits were repeated using the acceptance derived from the fast, zeroth order cross-section Monte Carlo (acceptance correction set #2, [29]). These results are shown in tables 4.5 and 4.6.

The χ^2 fit gave a $\chi^2 = 18.89$ for 16 degrees of freedom, with a confidence level of 0.2743. As shown earlier the results of the negative loglikelihood fits are independent of the acceptance, and hence are unaffected by its systematic errors. The χ^2 results, however, indicate the acceptance corrections derived from the

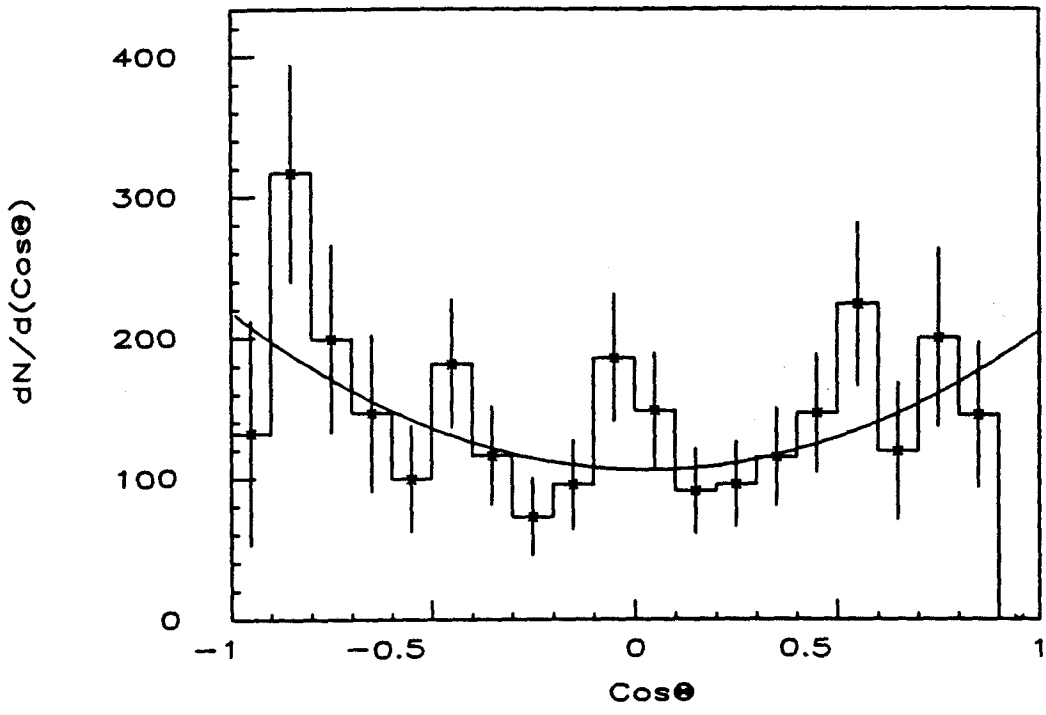

Figure 4.2: Negative Loglikelihood fit to $\cos\hat{\theta}$ distribution of 197 $z^0 \longrightarrow \mu^+\mu-$ candidates.

Forward-Backward Asymmetry Results		
Measurement Method	A_{fb}	ΔA_{fb}
Event-Counting	-0.0338	0.0772
log likelihood fit		
to β	-0.0334	0.0782
χ^2 fit to β	-0.0417	0.0787

Table 4.5: A_{fb} results using set 2 acceptance corrections and EHLQ1 parton distribution functions on the 188 event sample.

$\sin^2\theta_W$ Results		
Measurement Method	$\sin^2\theta_W$	$\Delta \sin^2\theta_W$
Event-Counting	0.2522	0.0294
log likelihood fit	0.2557	0.0251
χ^2 fit	0.2583	0.0260

Table 4.6: $\sin^2\theta_W$ results using set 2 acceptance corrections and EHLQ1 parton distribution functions on the 188 event sample.

monte carlo in which the P_t of the Z_0 yields a value of $\sin^2\theta_W$ which is 3% higher (0.2583 vs 0.2504) than the value derived from the simulation which incorporates all known detector effects. Moreover, the asymmetry goes from -1.7% to -4.2%, a factor of 2.5 change. The effects of uncertainties in the acceptance are, then, fairly large for the χ^2 procedures. In view of this, it it was decided to quote the loglikelihood fit results for the analysis.

4.4.2 Effects of Parton Distribution Functions

The choice of parton distribution functions adds a systematic uncertainty to the value of $\sin^2\theta_W$ extracted from the data. Parton distribution functions describe the relative densities of u and d valence and sea quarks within the proton and anti-proton. These distributions are measured by deep inelastic scattering of leptons and neutrinos on proton targets, and have uncertainties which grow as the momentum fractions of the partons decrease. The systematic effect on $\sin^2\theta_W$ was estimated by fitting the 188 event sample with several of the current parameterizations, EHLQ1, EHLQ2, DFLM1, DFLM2, MRSB, MRSE, DO1, AND D02. Tables 4.7 and 4.8 show the results of the negative loglikelihood and χ^2 fits. The systematic error on $\sin^2\theta_W$ was taken to be half the spread of values of $\sin^2\theta_W$ resulting from the loglikelihood fits. The systematic error on $\sin^2\theta_W$ due to uncertainty in the parton distribution functions is taken to be .001.

Log-Likelihood Fit Results		
P.D.F.	$\sin^2\theta_W$	$\Delta \sin^2\theta_W$
EHLQ1	0.2557	0.0251
EHLQ2	0.2557	0.0252
DO1	0.2562	0.0253
DO2	0.2563	0.0261
DFLM1	0.2557	0.0248
DFLM2	0.2558	0.0250
DFLM3	0.2553	0.0240
MRSB	0.2560	0.0256
MRSE	0.2561	0.0254

Table 4.7: Results of Negative Log Likelihood fits for $\sin^2\theta_W$ using various parton distribution functions.

χ^2 Fit Results		
P.D.F.	$\sin^2\theta_W$	$\Delta\sin^2\theta_W$
EHLQ1	0.2507	0.0249
EHLQ2	0.2507	0.0249
DO1	0.2512	0.0252
DO2	0.2511	0.0259
DFLM1	0.2508	0.0246
DFLM2	0.2508	0.0248
DFLM3	0.2504	0.0248
MRSB	0.2510	0.0254
MRSE	0.2511	0.0252

Table 4.8: Results of bin by bin weighted χ^2 fits for $\sin^2\theta_W$ using various parton distribution functions.

4.4.3 Effects of QCD Background on the Asymmetry

The background for the entire 188 event sample is estimated at 1 ± 1 event. Background events which consist $W^{\pm} \longrightarrow \mu^{\pm}\nu$ faking $Z^0 \longrightarrow \mu^+\mu^-$ show an asymmetry in $\cos\hat{\theta}$ of +36% [37]. Such events would produce a change in A_{fb} of

$$\Delta A_{fb} = \frac{n}{1-n} \cdot (A_{fb}^{backgrd} - A_{fb}^{observed}) \tag{4.10}$$

where n is the fraction of background events in the sample. The log likelihood result for A_{fb} is -0.0334. Therefore, one $W^{\pm} \longrightarrow \mu^{\pm}\nu$ background event in a sample of 188 Z^0 candidates would produce a change in A_{fb} of +0.21%. The measured value of A_{fb} should be decreased by 0.0021 to -0.0313. The effect on $\sin^2\theta_W$ is a shift of $\simeq 0.0008$. For dimuons from heavy quark decays faking a $Z^0 \longrightarrow \mu^+\mu^-$, the $\cos\hat{\theta}$ distribution would be symmetric, i.e. $A_{fb}^{backgr.} = 0$. In this case, equation 4.10 becomes

$$\Delta A_{fb} = n \cdot A_{fb}^{observed} \tag{4.11}$$

In this case, the observed asymmetry should be corrected by 0.02%. The effect on $\sin^2\theta_W$ for such a change is negligible. The estimate of 1 ± 1 event for the QCD background includes both heavy quark decay and W+jet events.

4.4.4 Limits on Charge Biases in Data Selection

The possibility of charge and η biases in the event selection criteria must be investigated since such biases would add a systematic error to the values of A_{fb}

and $\sin^2\theta_W$ extracted from the data. For a bias in the event acceptance to affect the $\cos\hat{\theta}$ distribution, it must be both η and charge dependent. The sign and magnitude of $\cos\hat{\theta}$ depends on the orientations of the positive and negative leptons in the detector relative to each other. If a selection criterion is purely η dependent, with no charge dependence, then of the events which are lost due to this bias, the number lost because the positive track failed to reconstruct should be the same as the number lost because the negative track failed to reconstruct. Because the effect is symmetric in charge, the events which survive the biased selection criterion would still have the same orientation relative to each other as would events in a totally unbiased sample. If the acceptance is symmetric in η, but has a charge dependent bias, then the events which get through have the same orientation relative to each other as events in a sample which has no bias. The event quality and trigger criteria used in the selection of the $Z^0 \longrightarrow \mu^+\mu^-$ sample were searched for evidence of charge and η dependent biases. It was assumed that such biases could not enter the sample through quantities measured by detectors which are charge blind (i.e. the calorimeters). Therefore, the minimum ionizing requirements on the muons ($E_{had} < 6$ GeV and $E_{em} < 2$ GeV for the central muons and $E_{had} + E_{em} < 20$ GeV for the forward muons) are assumed to be unbiased. Possible biases are investigated only for event quantities which are derived from the tracking detectors. These are:

- the CMUO Trigger.

- the CMUO and CMIO reconstruction.
- the isolation cut on the central muons, $ISO = \frac{E_{cone} - E_{\mu}}{P_{t_{\mu}}}$
- DIX, the match in the $x - y$ plane (measured in centimeters) between the CMUO stub and the CTC track.
- the forward muon recontruction.
- the P_t cuts on both the forward and central muons.

The high statistics central muon $W^{\pm}$ sample was used to investigate biases in the above-mentioned quantities for central muons. Samples of monte carlo events and of FMU+jet events were was used to search for biases in the FMU P_t cut and reconstruction.

4.4.4.1 Biases in the Central Muon Quality Requirements

The $W^{\pm}$ sample was divided into four sub-samples, positive muons, negative muons, muons with $\eta > 0$ (east), and muons with $\eta < 0$ (west). Distributions of P_t, DIX, and ISO were histogrammed, and a χ^2 for each distribution calculated. The distributions with the results of the χ^2 tests are shown in figure 4.3 and table 4.9. None of these three quantities show evidence for a bias which is both charge and η dependent.

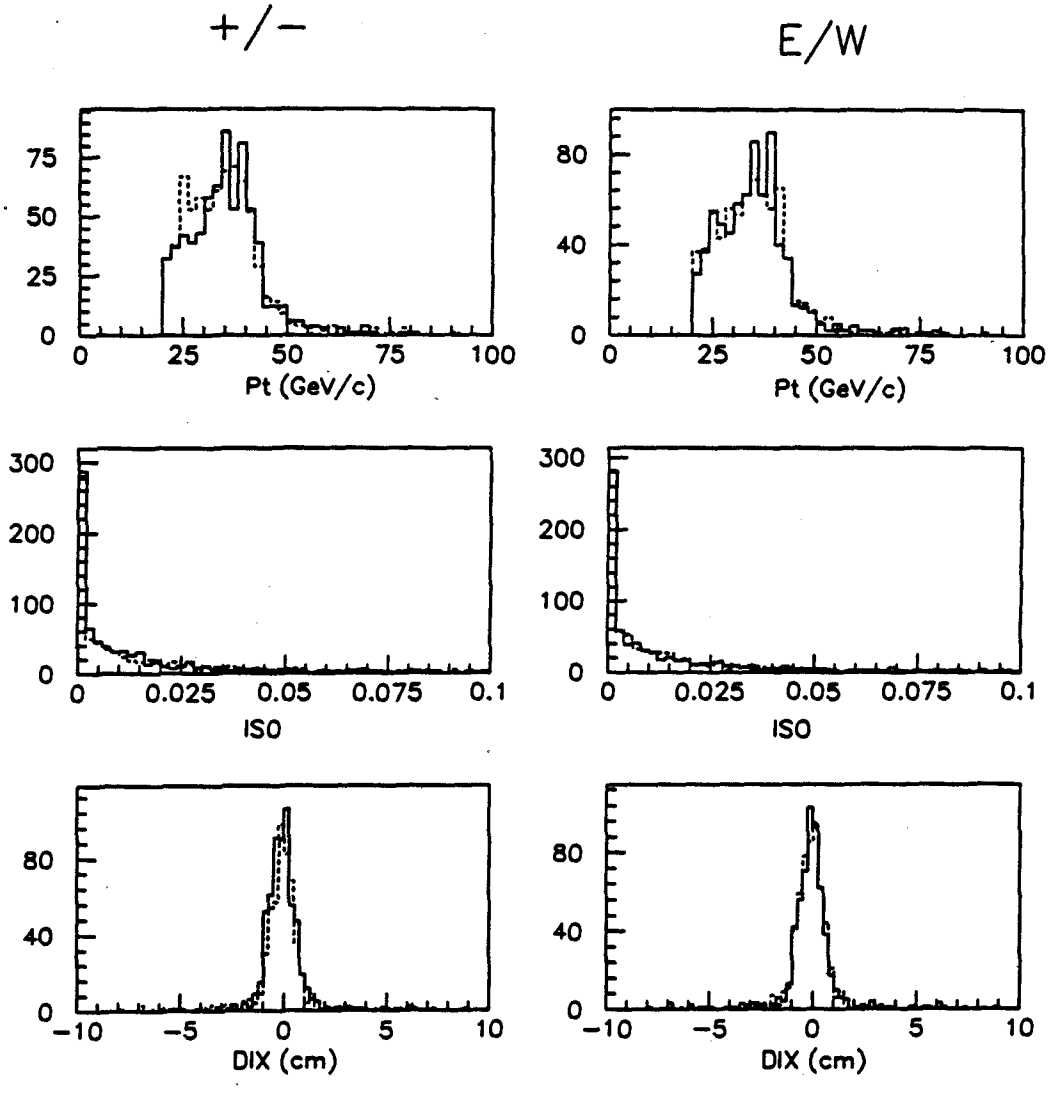

Figure 4.3: Distributions in DIX, P_t, and ISO for central muons in $W^{\pm} \longrightarrow \mu^{+}\nu$ events broken down by sign of the muon charge and η. Negative tracks shown in solid lines, positive in dashed.

Quantity	$\chi^2_{east/west}$	$\chi^2_{\pm}$	Degrees of Freedom
ISO	35.65	42.39	47
P_t	28.55	31.72	30
DIX	32.32	44.21	47

Table 4.9: Results of χ^2 comparison tests for muon quantities for east versus west side tracks, and positive versus negative tracks.

4.4.4.2 Biases in the Central Muon Trigger

All of the events in the $W^{\pm} \longrightarrow \mu^{\pm}\nu$ sample passed the CMU level 3 trigger. Of 1419 events, there were 723 W^+'s and 696 W^-'s. These numbers are within 1σ of each other. No study done with CDF data has shown evidence for such a bias in the momentum range of interest [35] [34] [36].

However, this does not put a quantitative limit to the size of such an effect (if it did exist, in spite of the evidence to the contrary) on either the forward-backward asymmetry or $\sin^2\theta_W$. In order to obtain such limits, a charge and η dependent trigger bias was inserted into the fast simulation used in the acceptance calculation of the form:

$$\mathrm{Eff_{bias}} = 0.914 + 0.141 \cdot \eta \cdot \mathrm{Q} \tag{4.12}$$

where Q is the charge of the lepton. This form was chosen in order to maximize the size of the effect in the simulated data. The factor of 0.141 ensured that

the biased efficiency went to 100% for $\eta \cdot Q = +0.61$, (the limit of the CMU chambers), and was less than 100% otherwise. 607 Z^0+ Drell Yan samples of 188 events apiece were generated using the ISAJET generator. They were first run through the fast simulation used for the acceptance (described in Chapter 3) using the actual 91.4% CMU level 3 trigger efficiency. Then, they were run through the same simulation into which the trigger was biased by equation 4.12. Each of the 607 samples, for each trigger condition, was fitted and values of A_{fb} and $\sin^2\theta_W$ were extracted. Finally, the distributions of A_{fb} and $\sin^2\theta_W$ were compared for the biased and unbiased samples. A large number of samples were needed to ensure that any observed effect was real. The distributions of differences in A_{fb} and $\sin^2\theta_W$ were found to cluster around 0.0042 ± 0.0032 and 0.0011 ± 0.0009, respectively. The systematic errors on A_{fb} and $\sin^2\theta_W$ due to possible trigger biases are therefore taken to be 0.0042 and 0.0011, respectively. These are, in some sense, 'worst case' estimates.

4.4.4.3 Reconstruction Biases

The CTC has been estimated to be better than 99.8% efficient for tracks falling in the range $|\eta| < 1.0$ [34], implying that reconstruction biases in this range are negligible. However, there is a large reconstruction inefficiency for tracks falling above $\eta = 1.0$, as has been discussed in previous sections. This inefficiency was estimated as a flat 64% over the range $1.0 < |\eta| < 1.4$ (the region of the PLUG calorimeteres) using a sample of $Z^0 \longrightarrow e^+e^-$ events, described in chapter 3.

η range	+ charges	− charges
$\eta > 0$	15	14
$\eta < 0$	9	19

Table 4.10: Breakdown of FMU-CMU Z^0 candidates according into sign of FMU charge and η.

In the actual data, there are 29 events which have a leg falling in the range $1.0 \mid \eta \mid < 1.4$. For eleven of these, the 'plug' leg is positively charged, and for 18, negatively charged. The 34 CEM-Plug Z^0 candidates for which track matches exist break down into 18 positively charged plug tracks and 16 negatively charged. If one adds these numbers to the 29 $Z^0 \longrightarrow \mu^+\mu^-$ legs, one has 29 positive and 34 negative tracks. These numbers are within 1σ of each other. There is no clear evidence for a charge bias, but these numbers are small.

There is a known east-west asymmetry in the forward muon acceptance, as was described earlier. This asymmetry reflects a reconstruction efficiency of 75% on the east of the detector ($\eta > 0$), and 85% on the west side ($\eta < 0$). The 51 FMU-CMU Z^0 candidates break themselves down as shown in table 4.10. There is no charge-related reconstruction bias in the FMU chambers for volunteer tracks with $P_t > 15$ GeV/c [39]. Only one of the 42 well-measured FMU-CMU Z^0 candidates has $10 < P_t^{fmu} < 15$ GeV/c, (2.4%). Since the east-west bias in the FMU system is not very pronounced, and since only $\sim 2\%$ of the FMU-CMU

sample would be affected by a charge bias, the dominant effect in the entire Z^0 sample, central-central plus central-forward, would be due to a reconstruction bias in the plug region, $1.0 <| \eta |< 1.4$.

Therefore, to put a limit on the effects on the effect of reconstruction biases on the asymmetry, a bias for tracks in the region $1.0 <| \eta | 1.4$ was modelled in the monte carlo, while the small forward bias was neglected. The procedure was the same followed for the study of the CMU trigger bias. First, based on the high CTC efficiency in the central region, the assumption was made that any bias in the region $| \eta |< 1.0$ was negligible. Then, for muons with $1.0 <| \eta |< 1.4$, a bias of a form similar to equation 4.12 was inserted into the fast monte carlo:

$$\mathrm{Eff_{bias}} = 0.65 + 1.75 \cdot (| \eta | -1.2) \cdot \mathrm{Q} \qquad (4.13)$$

The form of the equation for the reconstruction bias was modelled after that used for the trigger bias study. The fall-off in efficiency in the CTC is east-west symmetric, hence the absolute value signs on η. the boundary conditions were that the efficiency equal 100% for positively charged tracks at $\eta = 1.0$, and falls linearly to 30% at $\eta = 1.4$. For negatively charged tracks, the efficiency is 30% at $\eta = 1.0$, and 100% at $\eta = 1.4$. For both charges, the equation gives an efficiency of 65% at $\eta = 1.2$, the midpoint of the region, and also the average derived from the electrons. With this effect inserted into the simulation, 607 biased and unbiased samples of 188 events apiece were generated, as was done for the trigger bias study. In this case, the distributions of differences in A_{fb} and $\sin^2 \theta_W$ were found

to cluster around 0.00363 ± 0.00383 and $-.00105 \pm 0.00112$, respectively. The form of reconstruction bias was completely unreal, and enormous, yet it resulted essentially no observable effect on either the asymmetry or on $\sin^2 \theta_W$.

4.4.5 QCD and Other Radiative Corrections to the Asymmetry

The next highest order processes which affect the asymmetry fall into three categories:

- QCD processes involving gluon radiation by the initial state fermions.
- QED processes involving the radiation of a real or virtual photon by either the initial or final state particles.
- Electroweak effects involving the radiation of virtual W or Z bosons by either the initial or final state particles.

The Feynman diagrams for QCD processes are shown in figure 4.4. Gluon radiation produces Z^0 bosons with non-zero transverse momentum. In such cases, the approximation that the quark directions are collinear with those of the proton and anti-proton breaks down. The magnitude of the asymmetry is reduced in these events, since sometimes this assumption assigns the quark directions incorrectly, and thus has a symmetrizing effect on the angular distributions of the leptons, in a manner analgous to the effect of the sea quarks mentioned in chapter 2. The angular distribution of equation 4.1 ignores these and all other higher

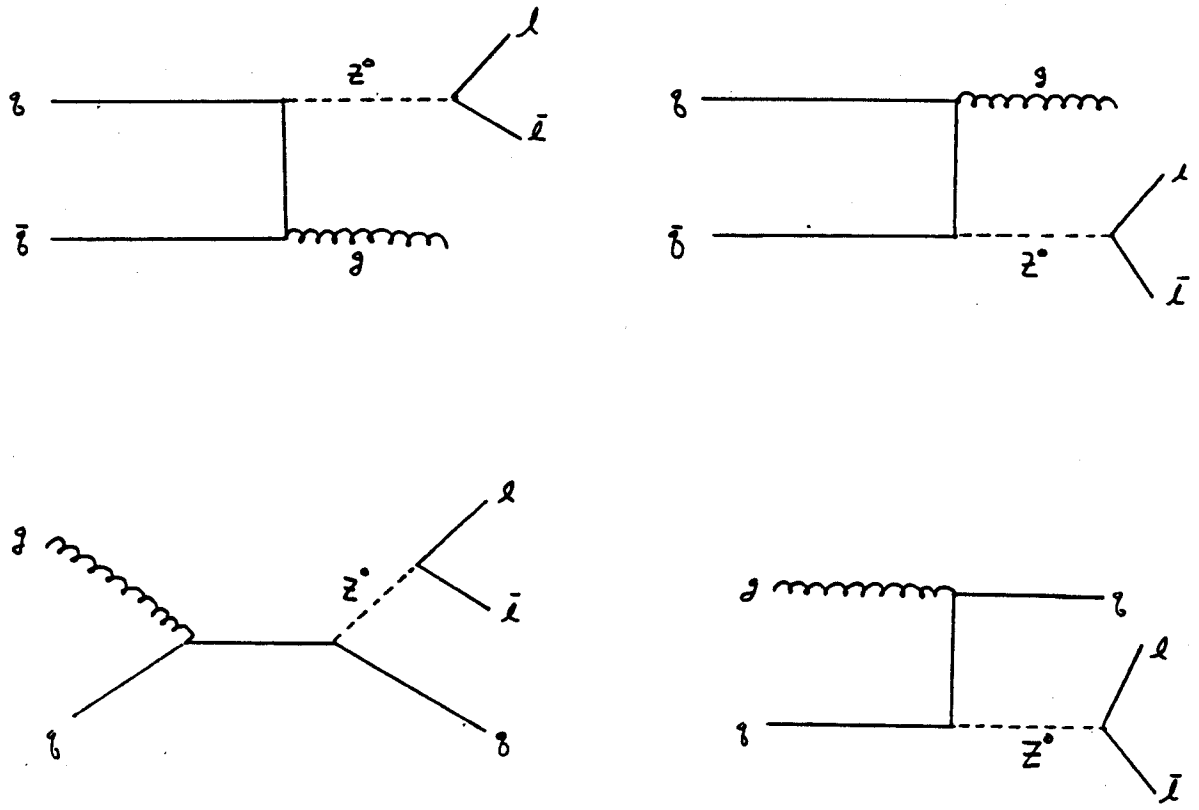

Figure 4.4: Feynman diagrams for QCD processes contributing to the dilepton cross-section.

order processes. The form of the distribution which correctly takes into account the effects of gluon radiation is given by [41]

$$\frac{d\sigma}{d\cos\hat{\theta}dP_t^Z} = \frac{d\sigma}{dP_t^Z}\{[((g_V^\mu)^2+(g_A^\mu)^2)((g_V^q)^2+(g_A^q)^2)]\cdot[1+\cos^2\hat{\theta}+\frac{1}{2}A_0(1-3\cos^2\hat{\theta})] \\ +8g_V^q g_A^q g_V^\mu g_A^\mu(1-A_3)\cos\hat{\theta}\} \quad (4.14)$$

A_0 and A_3 are functions of P_t^Z and are shown in in figure 4.5 taken from reference [42]. This corrected cross-sectionn is calculated in the Collins-Soper frame. Using this convention, as was stated previously in chapter 2, has the effect of dividing the P_t of the Z^0 evenly between the quark and anti-quark; it does not by itself 'correct' for non-zero transverse momentum of the boson. One must use equation 4.14 to correctly describe the angular distribution of the leptons when QCD effect are included. Writing the forward-backward asymmetry as

$$A_{fb} = \frac{\int_0^1 \frac{d\sigma}{d\cos\theta}d(\cos\theta)-\int_{-1}^0 \frac{d\sigma}{d\cos\theta}d(\cos\theta)}{\int_{-1}^1 \frac{d\sigma}{d\cos\theta}d(\cos\theta)} \quad (4.15)$$

and using this formula with the QCD corrected form of the cross-section of 4.14, and integrating over $\cos\theta$, one arrives at

$$A_{fb}^{measured} = \frac{3g_V^q g_A^q g_V^\mu g_A^\mu}{((g_V^\mu)^2+(g_A^\mu)^2)((g_V^q)^2+(g_A^q)^2)}\cdot\frac{\int_{-1}^1(1-A_3)\frac{d\sigma}{dP_t^Z}}{\int_{-1}^1\frac{d\sigma}{dP_t^Z}} \quad (4.16)$$

$$= A_{fb}(P_t^Z=0)\cdot\frac{\int_{-1}^1(1-A_3)\frac{d\sigma}{dP_t^Z}}{\int_{-1}^1\frac{d\sigma}{dP_t^Z}}$$

So, the measured asymmetry is equal to the asymmetry one would see if $P_t^Z = 0$, times a correction factor. The shift in the asymmetry due to QCD effects,

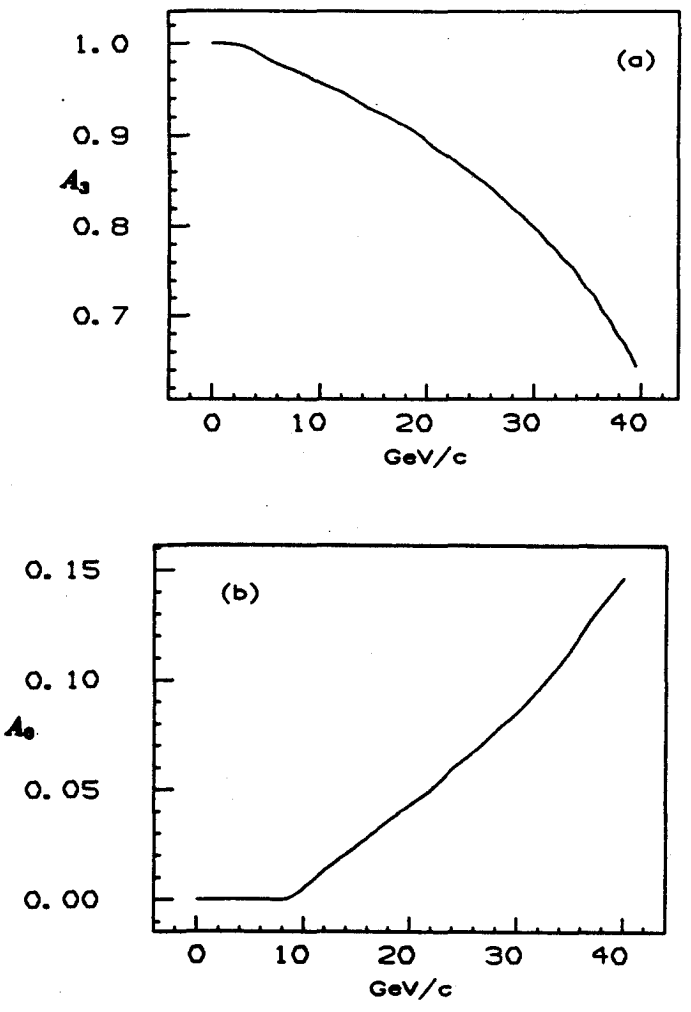

Figure 4.5: (A) A_3, the QCD smearing factor, versus P_t^Z. (B) A_0, the polarization coefficient, versus P_t^Z.

$\Delta A_{fb} = A_{fb}^{measured} - A_{fb}(P_t^Z = 0)$, is then given by

$$\Delta A_{fb} = A_{fb}^{measured}\left[1 - \left(\frac{\int_{-1}^{1}(1 - A_3)\frac{d\sigma}{dP_t^Z}}{\int_{-1}^{1}\frac{d\sigma}{dP_t^Z}}\right)^{-1}\right] \tag{4.17}$$

The integral in equation 4.17 was done by integrating the published CDF Z^0 P_t spectrum ([47], [48]) against the curve of figure 4.5. The CDF P_t^Z spectrum is of the form

$$\frac{d\sigma}{dP_t^Z} = \frac{P_t^Z\left[(P_t^Z)^2 + 39.04\right]^{-1.81}}{3.55\left[(P_t^Z \cdot 6.58 \times 10^{-5})^{7.20} + 1\right]} \tag{4.18}$$

Figure 4.6 shows the transverse momentum spectrum of the 188 $Z^0 \longrightarrow \mu^+\mu^-$ candidates used in this analysis. The curve is the parameterization of the published P_t^Z spectrum, normalized to the data. Performing the integral between 0 and 150 GeV/c, one obtains a multiplicative correction factor of 0.96996. Using this in equation 4.17, one finds that QCD effects reduce the observed asymmetry by 0.001. This corresponds to a shift in $\sin^2\theta_W$ of 0.0003.

4.4.5.1 QED and Electroweak Effects

The Feynman diagrams for the QED and weak processes are shown in figure 4.7. The QED effects consist of the bremsstrahlung diagrams of figure 4.7a, and the loop and box diagrams with an additional virtual photon shown in (b), (c) and (d). Of these four processes, this analysis considers only the effects of the final state bremsstrahlung on the asymmetry. Bremsstrahlung radiation is usually described as either 'hard' or 'soft', depending on the fraction of the femion energy, k, carried off by the brem'ed photon. The two states are distinguished by

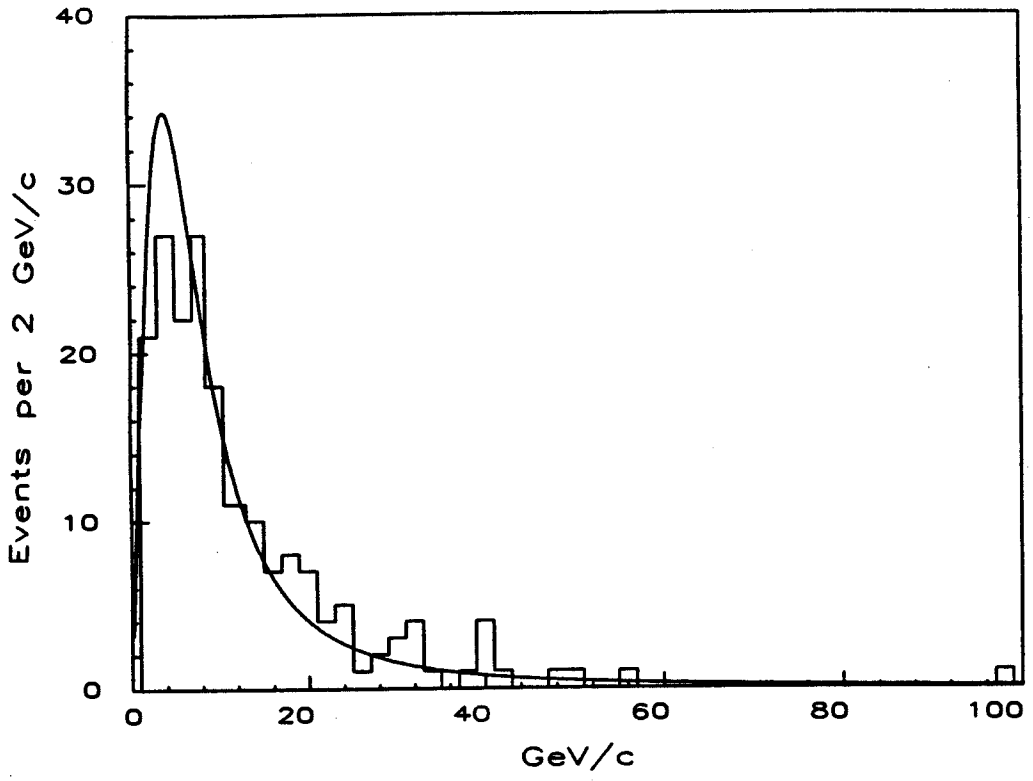

Figure 4.6: P_t **of the** Z^0 **for 188** Z^0 **candidates. The curve is the CDF published** P_t^Z **spectrum.**

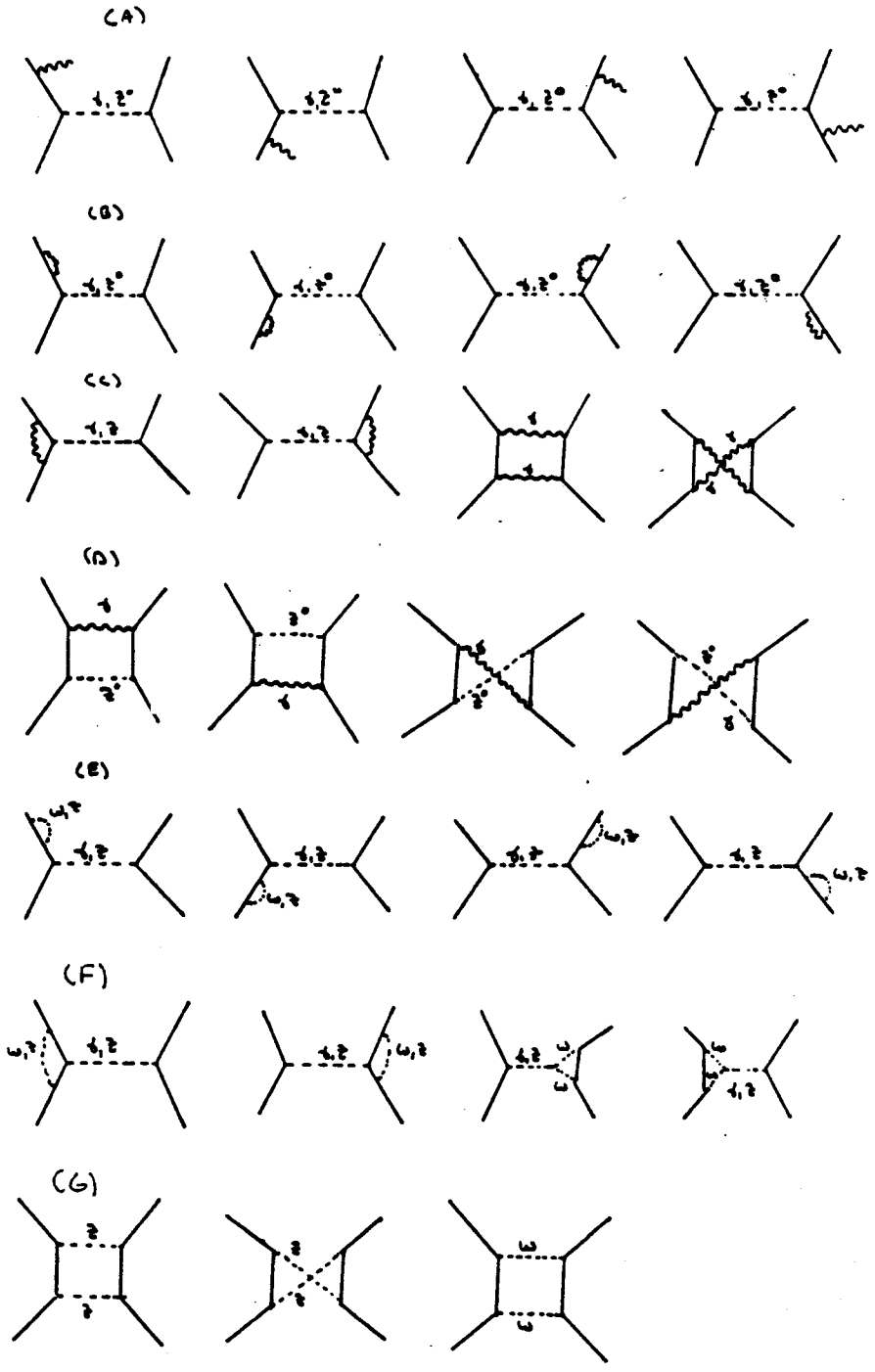

Figure 4.7: Feynman diagrams for QED and electroweak processes.

an arbitrary, dimensionless cut-off, k_0, which depends on the resolution of one's detector. 'Soft' radiation is less energetic, and has $k < k_0$. These photons can not be resolved by the detector, and the final state of the event is indistinguishable from a two-body final state. 'Hard' radiation, on the other hand, consists of brem'ed photons with $k > k_0$. These events have a three-body final state. Both hard and soft brem decrease the energy of the brem'ing particles, and slightly smear their angular distributions. The difference is only in the extent to which they produce these effects. The harder the brem, the larger the effect. Initial state brem is expected to have almost no visible effect, as the Z's in the sample must obviously be produced on resonance, and there is very little background above the Z peak. The final state brem would tend to cause the mass plot to grow a slight shoulder on the low end side, by slightly decreasing the momentum of the brem'ing muons. See figure 4.8. Events so affected would show an asymmetry smaller than one would expect for the region below the Z^0 resonance. However, unless one is looking specifically at asymmetries away from the Z^0, this effect is irrelevant. The effect is not visible when adding up events in a mass window 60 to 150 GeV/c^2, as was done in this analysis. The resolution of the detectors, particularly of the forward, coupled with the low statistics of the sample, did not make a study of the off-resonance asymmetries appear worthwhile. Therefore, only the effect of the smearing of angular distributions of the final state leptons was considered in this analysis. Smearing of the lepton directions would tend to reduce the observed asymmetry. One can easily put an upper limit on this effect

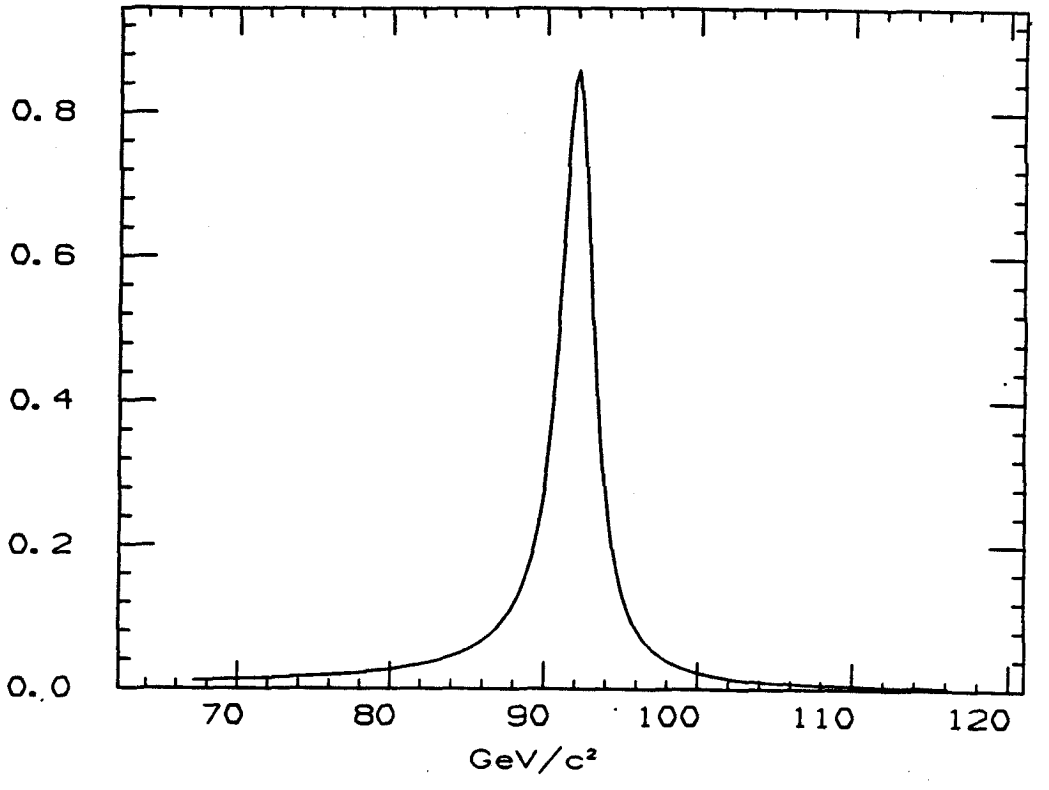

Figure 4.8: Invariant masses of dimuons about the Z resonance with (solid) and without (dashed) bremsstrahlung.

for the muons. Suppose that one of the muons in a $Z \longrightarrow \mu^+\mu^-$ decay brem'ed a photon which perturbed the polar angle of the muons by a small amount ϵ. Then, one actually measured an angle $\theta' = \theta + \epsilon$ for that muon, and

$$\cos\theta \rightarrow \cos(\theta + \epsilon) = \cos\theta - \epsilon \sin\theta \tag{4.19}$$

So, the lowest order form of the cross-section,

$$f(\theta) = A \cdot (1 + \cos^2\theta) + B \cdot \cos\theta \tag{4.20}$$

becomes

$$f(\theta') = A \cdot (1 + (\cos\theta - \epsilon\sin\theta)^2) + B \cdot (\cos\theta - \epsilon\sin\theta) \tag{4.21}$$

Keeping only terms up to order ϵ, this becomes:

$$f(\theta') = A(1 + \cos^2\theta) + B\cos\theta - 2\epsilon\sin\theta\cos\theta - \epsilon B\sin\theta \tag{4.22}$$

So, if one writes the forward-backward asymmetry in the form

$$A_{fb} = \frac{\int_0^1 f(\cos\theta)d\cos\theta - \int_{-1}^0 f(\cos\theta)d\cos\theta}{\int_{-1}^1 f(\cos\theta)d\cos\theta} \tag{4.23}$$

then

$$\begin{aligned} \int_0^1 f(\cos\theta)d\cos\theta &= \frac{4}{3}A + \frac{1}{2}B - \frac{\pi}{4}B\epsilon - 23A\epsilon \\ \int_{-1}^0 f(\cos\theta)d\cos\theta &= \frac{4}{3}A - \frac{1}{2}B - \frac{\pi}{4}B\epsilon + 23A\epsilon \end{aligned} \tag{4.24}$$

Taking the sum and difference of the results of the integrals in 4.24, and inserting them into 4.23, one finds

$$A_{fb} = \frac{B - \frac{4}{3}A\epsilon}{\frac{8}{3}A + \frac{\pi}{2}B\epsilon}$$

$$
\begin{aligned}
&= \frac{3}{8A}(B - \frac{4}{3}A\epsilon)(1 - \frac{3\pi B\epsilon}{16A}) \\
&= (A_0 - \frac{\epsilon}{2})(1 - \frac{\pi}{2}A_0\epsilon) \\
&= A_0 - \frac{\epsilon}{2} - \frac{\pi}{2}A_0^2\epsilon + \mathcal{O}(\epsilon^2)
\end{aligned}
\tag{4.25}
$$

where $A_0 = \frac{3}{8}\frac{B}{A}$, the unperturbed asymmetry. The dominant effect is the $\frac{\epsilon}{2}$ term, where ϵ is the amount the muon is deflected in emitting the photon. Figure 4.9 shows a muon of mass m_μ and momentum $\vec{k}$ radiating a photon of momentum q. The photon is emitted at an angle α with respect to $\vec{k}$, and the muon continues on with momentum $\vec{k}'$. Conservation of momentum requires

$$
\begin{aligned}
k' \sin\epsilon &= q \sin\alpha \\
k &= k' + q
\end{aligned}
\tag{4.26}
$$

For small α and ϵ, this becomes

$$k'\epsilon = q\alpha \tag{4.27}$$

or,

$$\epsilon = \frac{q\alpha}{k'} \tag{4.28}$$

For a particle of mass m, and momentum k, the angle at which a brem photon is emitted is given by

$$\alpha = \frac{m}{k} \tag{4.29}$$

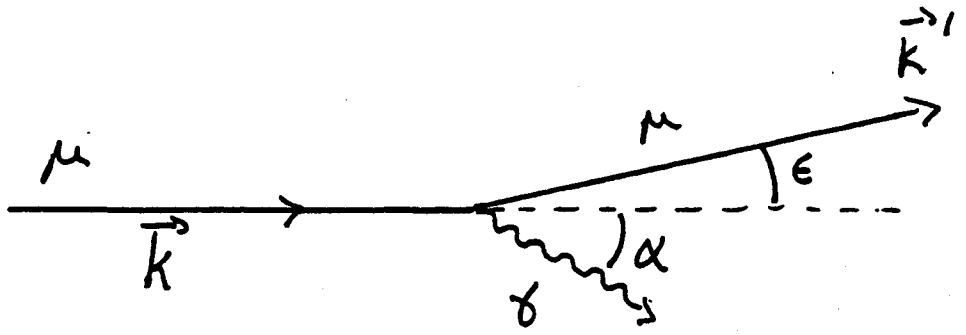

Figure 4.9: Muon bremsstrahlung.

So, the angle of perturbation, ϵ, is given in terms of the mass of the muon, its initial momentum, and the photon momentum by

$$\begin{aligned} \epsilon &= \frac{q \cdot m_\mu}{k(k-q)} \\ &= \frac{k_0 \cdot m_\mu}{k(1-k_0)} \end{aligned} \tag{4.30}$$

where $q = k_0 k$, and k_0 is the above-mentioned cut-off. Reference [43] computes the fraction of $Z^0 \longrightarrow \mu^+\mu^-$ events which have a brem photon of energy greater than the cut-off k_0, for various k_0 using the equation

$$\begin{aligned} \delta(k_0) = \frac{2\alpha}{\pi}\{ &\left(\ln\frac{s}{m^2} - 1\right) \cdot \left(\ln\frac{1}{k_0} - \frac{1}{4}(1-k_0)(3-k_0)\right) \\ &-\frac{\pi^2}{6} + Li_2(k_0) - \frac{1}{4}(1-k_0)(3-k_0)\ln(1-k_0) \\ &+\frac{1}{8}(1-k_0)(5-k_0)\} \end{aligned} \tag{4.31}$$

where $s = 8100$ GeV^2, $m = .106$ GeV$/c^2$, and $Li_2(k_0)$ is a dilogarithm defined by

$$Li_2(z) = \int_0^1 \frac{\ln(1-xz)}{x} dx \tag{4.32}$$

These results are contined in table 4.11, along with the values of ϵ, and the change in the asymmetry, $\Delta A_{fb} = \frac{\epsilon}{2}$ which would be produced for each k_0. The second and third columns of table 4.11 should be interpreted in the following way: 78% of all $Z^0 \longrightarrow \mu^+\mu^-$ decays (at $\sqrt{s} = 1.8$ TeV) will have a brem with $k_0 < 0.01$. Such muons will decrease the asymmetry by < 0.00003, an extremely small number. $22.2 - 13.1 = 9.1\%$ of the events will brem a photon with k_0 between 0.01 and 0.05. This 9% will tend to decrease the asymmetry between

k_0	$\delta(k_0)\%$	ϵ	ΔA_{fb}
0.01	22.2	0.00005	0.00002
0.05	13.1	0.00028	0.00014
0.10	9.2	0.00058	0.00029
0.15	7.2	0.00093	0.00046
0.20	5.8	0.00131	0.00066
0.30	4.0	0.00225	0.00112
0.40	2.9	0.00350	0.00175
0.50	2.1	0.00525	0.00262
0.60	1.4	0.00788	0.00394
0.70	0.9	0.01225	0.00612
0.80	0.5	0.02100	0.01050
0.90	0.2	0.04725	0.02362

Table 4.11: %'s of muons radiating a photon of fractional energy k_0 or greater.

0.00003 and 0.00014, and so forth. The calorimetry cuts used in selecting the muons in the data samples result in no muons with energy> 5 GeV in a cone of $R = 0.4$ about the muon in $\eta - \phi$ space. For muons in the data, k is at least 20 GeV/c. This implies that the largest k_0 we need to worry about is about 0.25. $k_0 = 0.25$ corresponds to $\Delta A_{fb} = 0.0009$. But, only $\sim 5\%$ of all events will feature a brem photon which will change the asymmetry by this much. 95% of the muons in the sample will brem with $k_0 < 0.25$, consequently making a change in A_{fb} much less than $\simeq 0.0009$. This figure, 0.0009 is taken as an upper limit on the change in the asymmetry. This corresponds to a change in $\sin^2\theta_W = 0.0003$. These rather simple arguments do not take into account any possible asymmetries arising from of the quantum mechanical interference between the initial and final state brem diagrams. Also, the box and loop diagrams, which are of order α^4 and produce extremely small effects, interfere with the lowest order, non-radiative diagrams, and produce terms in the cross-section of order α^3. The effects of these interference terms are also neglected.

4.4.5.2 Electroweak Effects

The Feynman diagrams for the order α^3 electroweak processes which contribute to the total cross-section are shown in figure 4.7e-g. These are box and vertex diagrams which have additional W and Z^0 bosons, and diagrams with loop corrections to the propagators. Like the QCD and brem corrections, these processes have only a small effect on the asymmetry, and are not calculated in this thesis.

Source	ΔA_{fb}	$\Delta \sin^2\theta_W$
Parton Distribution	—	0.0010
QCD Background	0.20%	0.0008
Trigger Bias	0.42%	0.0011
CTC Reconstruction Bias	0.39%	0.0010
Gluon Bremsstrahlung	0.10%	0.0003
QED Bremsstrahlung	0.09%	0.0003

Table 4.12: Summary of systematic uncertainties on A_{fb} and $\sin^2\theta_W$.

For interested readers, reference [49] contains the results of a detailed calculation of the weak effects, and also the QED processes neglected in this analysis, for the process $\bar{p}p \longrightarrow Z^0 \longrightarrow e^+e^-$ pairs.

4.5 Summary of Results

The systematic errors on A_{fb} and $\sin^2\theta_W$ are summarized in table 4.12. Adding these systematics in quadrature, one arrives at the total systematic uncertainty on A_{fb} equal to 0.62%, and on $\sin^2\theta_W$, .002. With the statistical errors, and the correction for the QCD effects, the following values for the forward-backward asymmetry and $\sin^2\theta_W$ are quoted for this analysis:

$$\begin{aligned} A_{fb} &= -3.34\% \pm 7.82\%(\text{stat.}) \pm 0.62\%(\text{sys.}) \\ \sin^2\theta_W &= 0.2566 \pm 0.0254(\text{stat.}) \pm 0.002(\text{sys.}) \end{aligned} \tag{4.33}$$

A_{fb} and $\sin^2\theta_W$ were extracted using the negative loglikelihood fit to the $dN/d\cos\hat{\theta}$ distribution of 188 central-central and central-forward Z^0 candidates, and EHLQ1 parton distribution functions in the cross-section. These results were selected because the log likelihood method is independent of the acceptance, which has been shown to have large systematic errors, though none which bias the $\cos\hat{\theta}$ distribution by being both charge and η dependent. The values for the asymmetry and $\sin^2\theta_W$ are both within 1σ of the results extracted by a similar analysis using the $Z^0 \longrightarrow e^+e^-$ data from the same CDF data run: $\sin^2\theta_W = 0.228\ ^{+0.017}_{-0.015}\ (stat.) \pm 0.002(sys.)$ and 5.2 ± 5.9(stat.) $\pm$ 0.002(sys.) [40], and also with the $\sin^2\theta_W$ results published by the ALEPH and L3 collaborations at LEP, 0.2292 ± 0.0040 and 0.230 ± 0.006 [45], [46] extracted from measurements of the mass and partial width of the Z^0 resonance.

Chapter 5

Conclusions

The analysis presented in this thesis describes a measurement of a physical parameter, the forward-backward angular asymmetry in the reaction $\bar{p}p \longrightarrow Z^0 \longrightarrow \mu^+\mu^-$ at $\sqrt{s} = 1.8$ TeV. From this measurement, a value of the Weinberg angle, $\sin^2\theta_W$, was extracted. The results are:

$$\begin{aligned} A_{fb} &= -3.34 \pm 7.82(\text{stat.}) \pm 0.62(\text{sys.})\% \\ \sin^2\theta_W &= 0.257 \pm 0.025(\text{stat.}) \pm 0.002(\text{sys.}) \end{aligned} \tag{5.1}$$

When combined with the published results using the electrons at CDF [40]:

$$\begin{aligned} A_{fb} &= 5.2 \pm 5.9(\text{stat.}) \pm 0.4(\text{sys.})\% \\ \sin^2\theta_W &= 0.228\ ^{+0.017}_{-0.015}\ (stat.) \pm 0.002(sys.) \end{aligned} \tag{5.2}$$

the combined results for all the $Z^0 \longrightarrow \bar{l}l$ data taken during the 1988-1989 run

at CDF become

$$\begin{aligned} A_{fb} &= 1.8 \pm 4.7(\text{stat.}) \pm 0.4(\text{sys.})\% \\ \sin^2\theta_W &= 0.239 \pm 0.014(\text{stat.}) \pm 0.014(\text{sys.}) \end{aligned} \tag{5.3}$$

The major obstacle to obtaining more precise results for this analysis was the limited nature of the muon coverage at CDF during the 1988-89 run. The central muon trigger covered only 60% of the region covered by the electron trigger. Also, the fall-off in the efficiency of the central tracking chambers made identification and the calculation of the acceptance very difficult for tracks with pseudo-rapidities greater than $|\ 1.0\ |$. For the 1992 run, the central muon chamber coverage has been extended to $\eta = |\ 1.0\ |$, making the coverage of the central muon trigger equivalent to that of the central electrons. In addition, it is hoped that improvements in the forward muon triggering and signal to noise ratio may make forward triggered data available. Finally, work continues towards a more quantitative understanding of the acceptance of the central tracking chamber in the region $|\ \eta\ | > 1.0$. It is hoped that the data from the 1992 will provide a higher statistics sample so that this measurement may be performed to a greater precision and accuracy.

Appendix A

The Forward Muon Gas Gain Monitoring System

This appendix contains a description of the FMU chamber gain monitoring system in use during the 1988-89 CDF data run. Twenty-three of the 144 drift chambers (four per plane, except for the west rear plane, which has only three) in the FMU detector had Fe-55 sources mounted on the inner wall of each of their drift cells for the purpose of calibrating the chambers' gain. This was done by measuring the position and width of the 5.9 keV K-capture peak of Fe-55 absorbed in Argon-Ethane. The goal of the source-monitoring project during the 1988-89 data run was to maintain the chamber voltages at or above the threshold where the chambers would be maximally efficient. This threshold was defined to be a voltage such that the 5.9 keV peak was fully resolved. Minimum ionizing radiation [52] typically deposits on the order of a few keV of energy in 1 cm of gas. It was hoped that by maintaining the voltages so that the Fe-55 peak was fully

resolved that this would ensure that the drift chambers would also be fully efficient in detecting minimum ionizing radiation. Figure A.1 [56] shows a schematic of the source monitoring read-out system. Photo-absorption signals from the 12 source drift cells on the chambers traveled along the wire to the chamber pre-amp and were picked off by a separate emitter-follower circuit on the chamber, and then sent along approximately 200 ft. of 12 channel twisted-pair ribbon cable to the CDF counting room above the detector. Here, they were read-out, amplified, shaped, and digitized by source read-out electronics. Based on the amplitude and width of the resulting spectra, the decision was made as to whether the FMU chamber voltage needed adjustment. With 23 source chambers in the detector, there were thus 276 (12 cells/chamber $\times$23 chambers) individual source signals to be read-out. The FMU source-monitoring electronics contained in the B0 counting room can be divided into two basic subsystems: signal read-out and triggering. The portions of the FMU source monitoring electronics used for signal read-out were part of the CDF RABBIT system, the front end of the CDF data acquisition electronics, while the triggering for the system was provided by CAMAC modules and the VAX. RABBIT was an acronym for Redundant Access Bus-Based Information Transfer. This simply means that each RABBIT crate housing DAQ electronics had two buses on its backplane for transferring the information the cards in the crate receive. During the 1988-89 run, however, only one of these buses was utilized. A more detailed description of the RABBIT system is contained in [54]. The brain of the FMU source monitoring hardware was

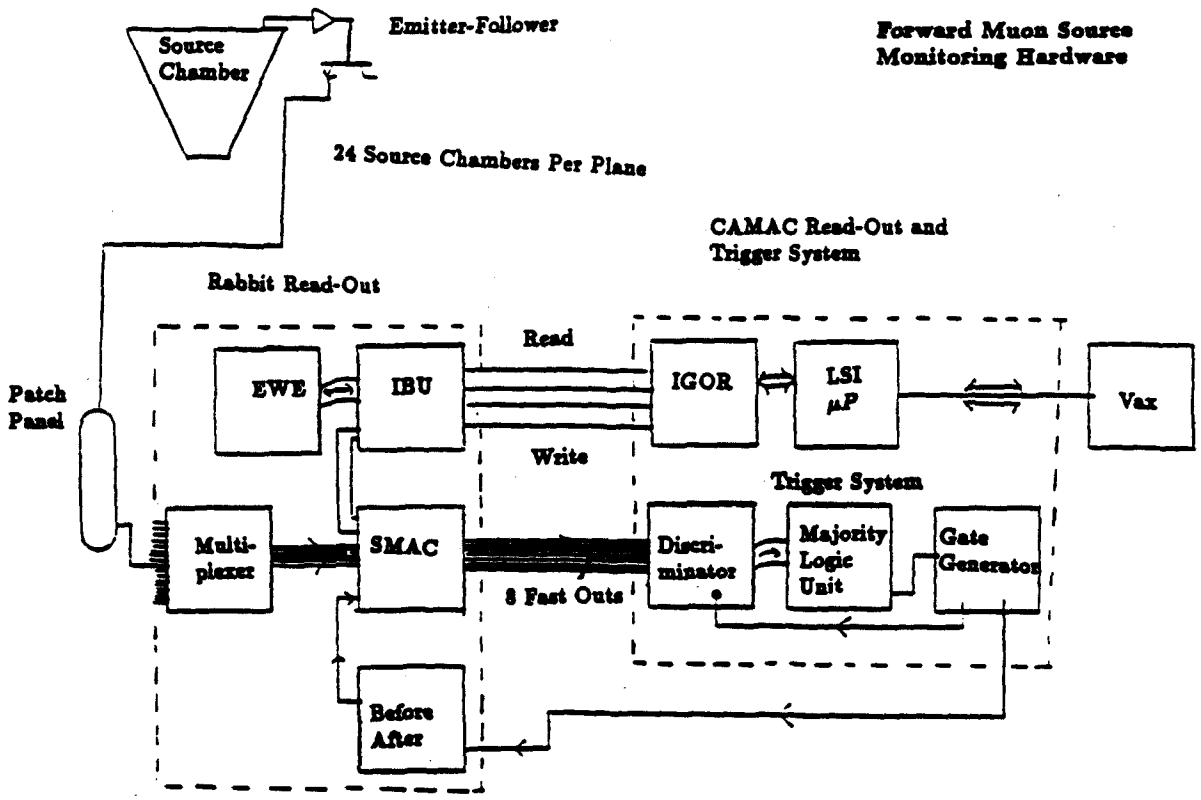

Figure A.1: Schematic of the FMU Fe-55 Source-Monitoring Read-out System.

a CAMAC LSI microprocessor. This unit relayed instructions from the VAX to the appropriate triggering and signal read-out modules, read back the processed source signal information from the RABBIT cards, and relayed this information to the VAX. The VAX talked to the LSI along the CAMAC serial highway via the 3952 Type L-2 Serial Crate controller module which sat next to the LSI in the CAMAC crate. The interface between the LSI and the other modules in the CAMAC crate is the 3923 Crate Controller, which sat next to the 3952.

Specifically, the read-out and triggering subsystems contain the following elements:

- Data Read-Out
  - The Source Multiplexer – this unit took the 276 Fe-55 signals coming into the counting room and fed them 8 at a time to the first module in the signal-processing chain, which was:
  - The Source Monitoring Amplification Card – A RABBIT module which took source signals from the chamber and fed them into a charge integrator and amplifier prior to their digitization by the following module:
  - The EWE – An analog-to-digital converter. Its I/O registers, upon instruction from the LSI, took analog source signals from the eight SMAC channels (which traveled to the EWE registers along the backplane of the RABBIT crate), digitized them, and then sent the digitized information back to the LSI which sent it on to the VAX. The

interface between the LSI and CAMAC module, and the EWE (RABBIT) was provided by the two modules:

- First, a Kinetic Systems 3061 General Purpose Input/Output Register, or IGOR. This CAMAC module was the first step in the EWE-LSI interface. The LSI wrote commands destined for the EWE first to the IGOR, which, in turn, relayed these commands to the module comprising part two of the interface:
- The IBU, a TTL to ECL converter. This is a RABBIT module which interfaced between the IGOR and the EWE. So, LSI commands travelled $LSI \rightarrow IGOR \rightarrow IBU \rightarrow EWE$, and digitized SMAC information was sent back by the EWE to the LSI via the same path.

• Triggering

- SMAC Card - The SMAC also provided its own triggering for the read-out via a 'fast-out' circuit on the board.
- LeCroy 4416B Programmable Discriminator - A CAMAC module which recieved the eight fast-outs and generated an ECL pulse for each of those exceeding a reasonable threshold for a real source signal. This pulse is sent to:
- The LeCroy 4352 Majority Analog Logic (MALU). This CAMAC module is a combination of an 'OR' circuit and a latch. It determined which of the Discriminator channel(s) had triggered, sent a look-at-me signal

to the LSI, informing the LSI that it had a trigger, and finally sent a pulse to the next unit in the trigger logic:

- A LeCroy CAMAC 2323 Programmable Gate Generator. This CAMAC unit sent the timing window down to a RABBIT module called:
- the Before/After Timing Unit or BAT. This module controlled the timing of the sample and hold circuit on the SMAC.

Inside the counting room, the 23 cables attached to a software-controlled multiplexer which the source-monitoring code directed to patch through the source signals 8 at a time to the rest of the source read-out sytem, according to cell size, and proceeding in alphabetical order from the front plane 'A' cells through the rear plane 'L' cells. (i.e. It started with the 'A' cell signals from the 8 front plane source chambers, which consisted of 4 chambers in east front plane, and 4 in the west; then it moved to the front plane 'B' signals, etc., through all the front cells. Then, it multiplexed through the cells A-L of the 8 middle plane chambers in the identical fashion, and finally the same with the rear plane chambers). Each channel was read out until the LSI saw that the EWE registers had accumulated 1000 events for each of the 8 channels, then this data was uploaded to the vax, and the multiplexer was signalled to move on to the next set of 8 source signals. After moving through the multiplexer, the source signals were fed into eight inputs of the Source Monitoring Amplifier Card (SMAC). The SMAC card had two functions: (1) it acted as a charge-integrating amplifier for the source

signals prior to their digitization, and (2) it provided its own timing gate via a separate 'fast-out' circuit on the board. A schematic of the SMAC card is shown in figure A.2 [56]. Referring to this schematic, the output of the charge integrator is first tapped for the trigger, then sent through a delay line to give time for trigger logic to provide a timing gate for the signal. The fast-out circuits on the SMAC sent the tapped signals up to the first module in the CAMAC trigger logic system, a LeCroy 4416B Programmable Discriminator, whose threshold was set via LSI at $300mV$. When a fast-out signal from the SMAC card exceeded this threshold, the discriminator generated an ECL pulse. The 8 discriminator outputs were sent to 8 inputs of a 32 channel LeCroy 4532 Majority Analog Logic Unit (MALU). The MALU counted the number of discriminator pulses it received and created a current proportional to the hit multiplicity. When the current generated in this way by the combined discriminator hits exceeded a level set by an internal potentiometer in the MALU (in this case, 30 mV), the MALU output an ECL level from the MDO (Majority Discriminated Output) connector on its front panel. This level was fed, in turn, to the Gate Input (GAI) connector next to the MDO. The gate input was used to provide a timing window within which the MALU counted the hits it received from the discriminator. Normally, this gate is always open, but when the Gate Input is attached to the Majority Discriminated Output, the receipt of the voltage level from the MDO causes the gate to close. So, as soon as the MALU had accumulated enough hits to exceed the pre-set current threshold, the Majority Discriminated Output sent an ECL

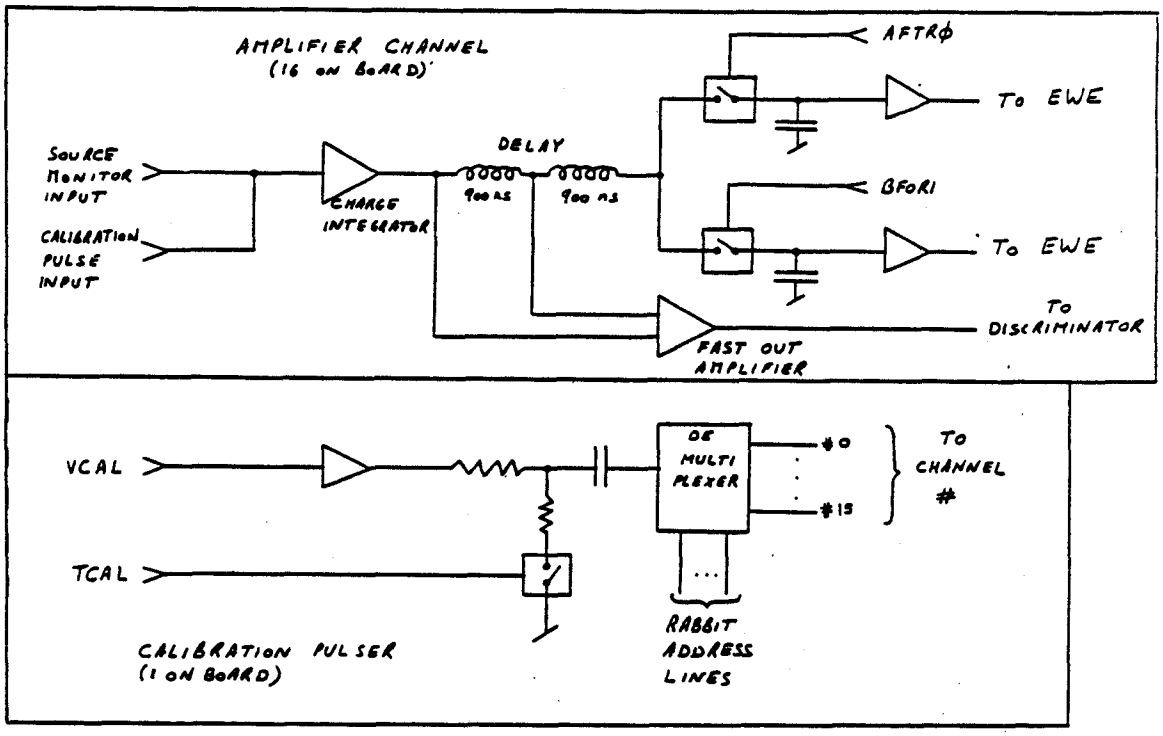

Figure A.2: A Functional Schematic of the FMU Source Monitoring Amplifier Card.

level to the Gate Input, thereby shutting off receipt of any more hits. At this point, the MALU latched its input pattern, sent a 'look-at-me' (LAM) to the LSI (telling it that it has a trigger), and finally issued a $20ns$ ECL strobe pulse from its Strobe Out connector (STO) to the next module in the CAMAC trigger system, a 2323 LeCroy Programmable Dual Gate Generator. The LSI read the MALU input pattern, determined which SMAC channel had the trigger, and sent commands to the EWE to set up its corresponding channel to read-out and digitize the event. Upon receipt of the MALU strobe, the gate generator issued a clear and strobe ECL pulse $2500ns$ wide to the Before/After Timing module (BAT) which resides in the RABBIT crate next to the SMAC card. The BAT generated two +15 volt levels, the Before and After signals, which were sent to two sample and hold circuits on the SMAC. Prior to the signal from Fe-55 source arriving at the sample and holds after the $1800ns$ delay lines, the Before and After were both high, and the switches on the sample and holds were closed. At this time, the circuits were sampling the pedestal level of the charge integrator output. On the rising edge of Clear and Strobe, the Before level dropped to 0 volts, and the switch to which it was connected opened, holding the accumulated charge of the pedestal on its capacitor. For the $2500ns$ of the Clear and Strobe window, the other sample and hold circuit continued to sample the output of the charge integrator, which was at this point a combination of pedestal and source signal. When the falling edge of Clear and Strobe arrived, the After level fell to zero, and the accumulated charge was held on the second capacitor. The timing

of the trigger logic is shown in figure A.3 [56]. The two accumulated charges were sent to the EWE where they were digitized and subtracted. Their net difference was the source signal for that SMAC channel. Each channel had a pre-set number of triggers which it had to accumulate (1000). This number was set by software, and was contained in the commands the VAX sent to the LSI. The LSI continued to read out the MALU input patterns until each of the eight source channels had accumulated the required number of hits. Once this was accomplished, the LSI sent a LAM to the VAX indicating that it was ready to upload its data arrays to the VAX. Data from the source chambers was uploaded in batches of eight, in the same order as the multiplexer moved through the various cell sizes in the detector: front plane 'A' cells through the rear plane 'L' cells. The spectrum from a typical 'D' cell, digitized in ADC counts, is shown in figure A.4. The main peak comes from the 5.9 keV photons. The first escape peak (3.1 keV) is clearly visible on the low end of the main peak. The position of the 5.9 keV peak and its sigma are calculated in terms of EWE ADC counts from the uploaded data. The level of pedestal in each amplifier channel was measured prior to source data-taking and subtracted from the peak position. This pedestal was a finite offset in the data due to hardware elements, such as the EWE ADC's, downstream from the SMAC's sample and hold circuits [56]. Table A.1 contains the mean values of the pedestal in each of the eight SMAC channels, digitized in EWE ADC counts, along with their widths. The magnitude of the peak-pedestal was measured for each source cell in the detector on roughly a daily basis during the

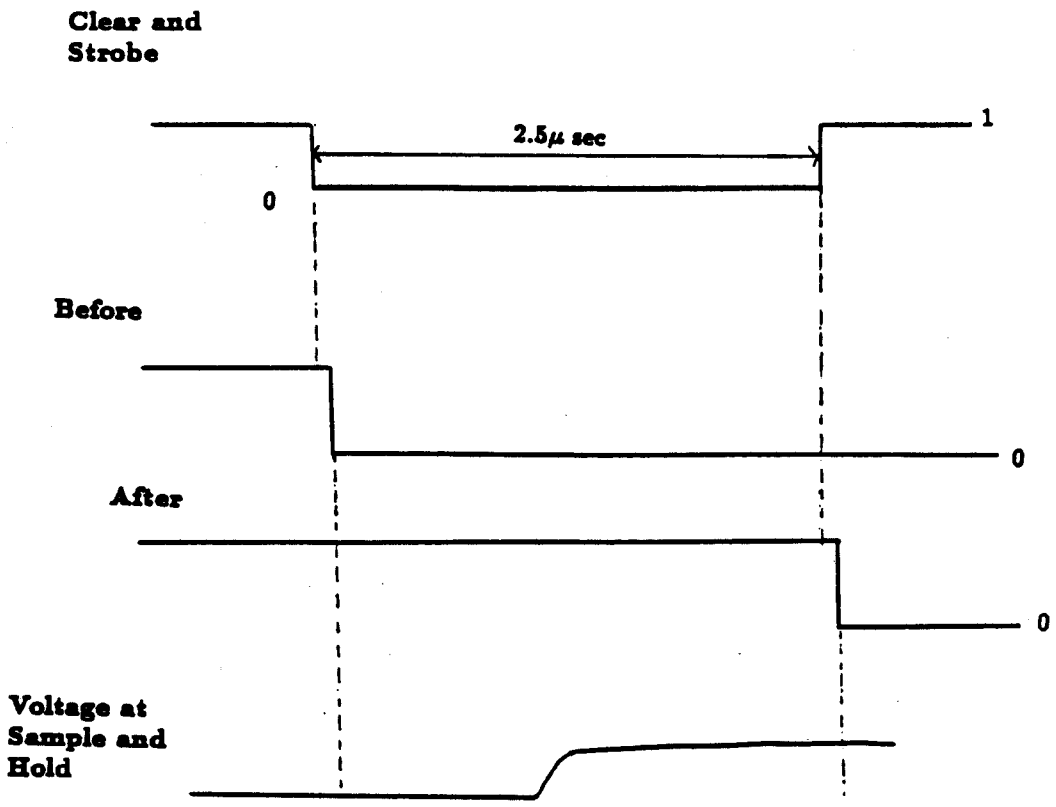

Figure A.3: Trigger logic Timing in the FMU Source Monitoring System.

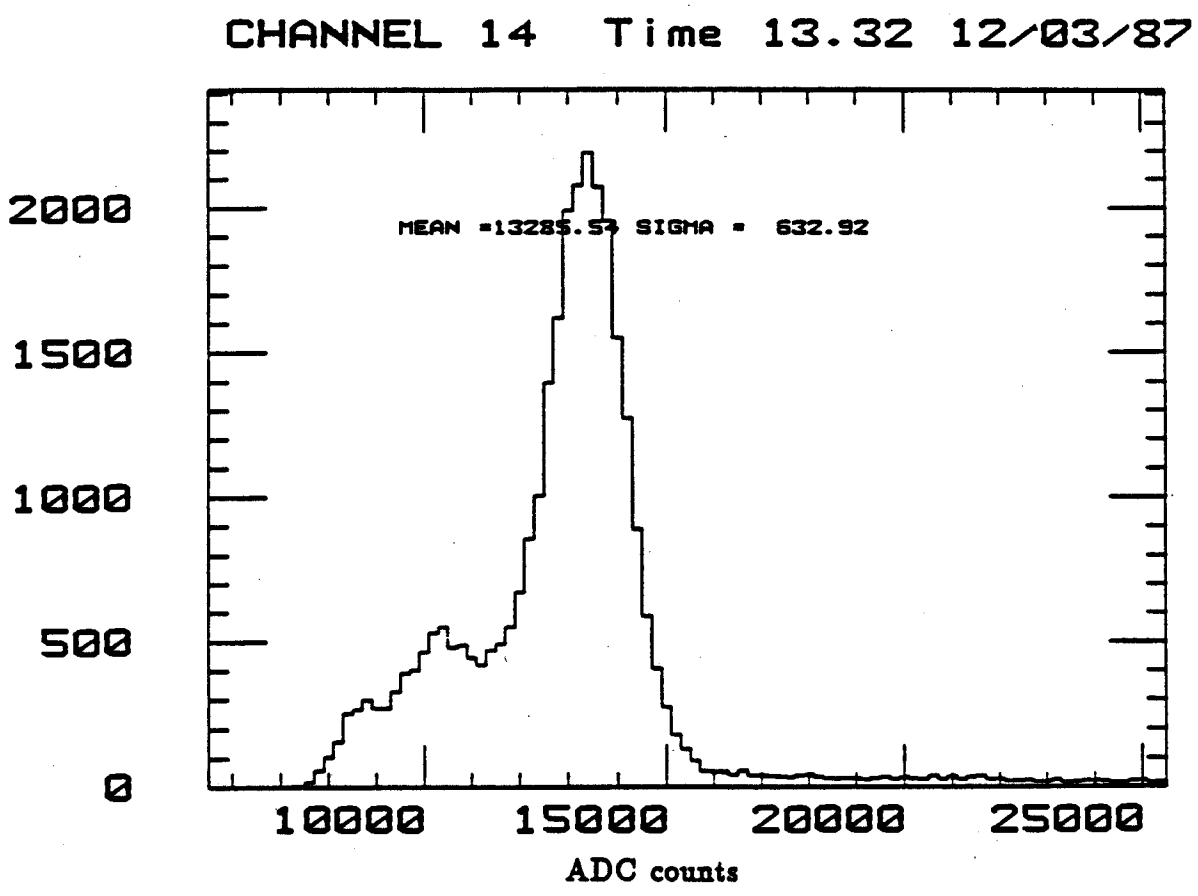

Figure A.4: Digitized Fe-55 spectrum from a 'D' cell in an FMU source chamber, before pedestal subtraction.

SMAC Channel	Pedestal	σ
0	6455.	52.
1	6480.	77.
2	6699.	66.
3	6362.	72.
4	6529.	45.
5	6460.	36.
6	6538.	58.
7	6537.	55.

Table A.1: Mean Values of SMAC pedestals in EWE ADC counts.

run. An attempt was made to maintain all of the cells at a voltage which resulted in a peak-pedestal reading of $\sim$ 5500 ADC counts, by adjusting the voltages on the high voltage power supplies which fed the cells. However, large variation in chamber response made this difficult. Chamber response tended to degrade over time due to space charge build-up on the non-conducting portions of the chamber drift cell walls. Figure A.5 shows histograms of the peak-pedestal values and sigmas for the 'H' cells in the eight middle plane source chambers for data taken on August 4, 1988. All eight 'H' cells are powered by the same high voltage supply, and yet show factor of two variations in gain. The cells in the source chambers on the bottom half of the east middle plane (labelled 'channel 2' and 'channel 4' in figure A.5), are barely above threshold, while channels 5-8 (the chambers in the middle plane on the west end of the detector) all have at least one escape peak, in addition to the main peak clearly resolved. Such variations are attributable to chamber-to-chamber variations in gas quality, emitter-follower response, and space charge accumulation. The peak - pedestal values and sigmas for all source cells in the detector are histogrammed in figure A.6.

Figure A.7 shows the peak-ped response for a front plane 'E' cell over a period of 90 days, each bin in the histogram corresponding to one day. The voltage adjustments were made with the intention of keeping all of the drift cells in the detector above the threshold for detecting minimum ionizing radiation. The cell to cell variations in gain were not important as long as the variations were all above this threshold. Independent studies of data taken during the 1988-89 run

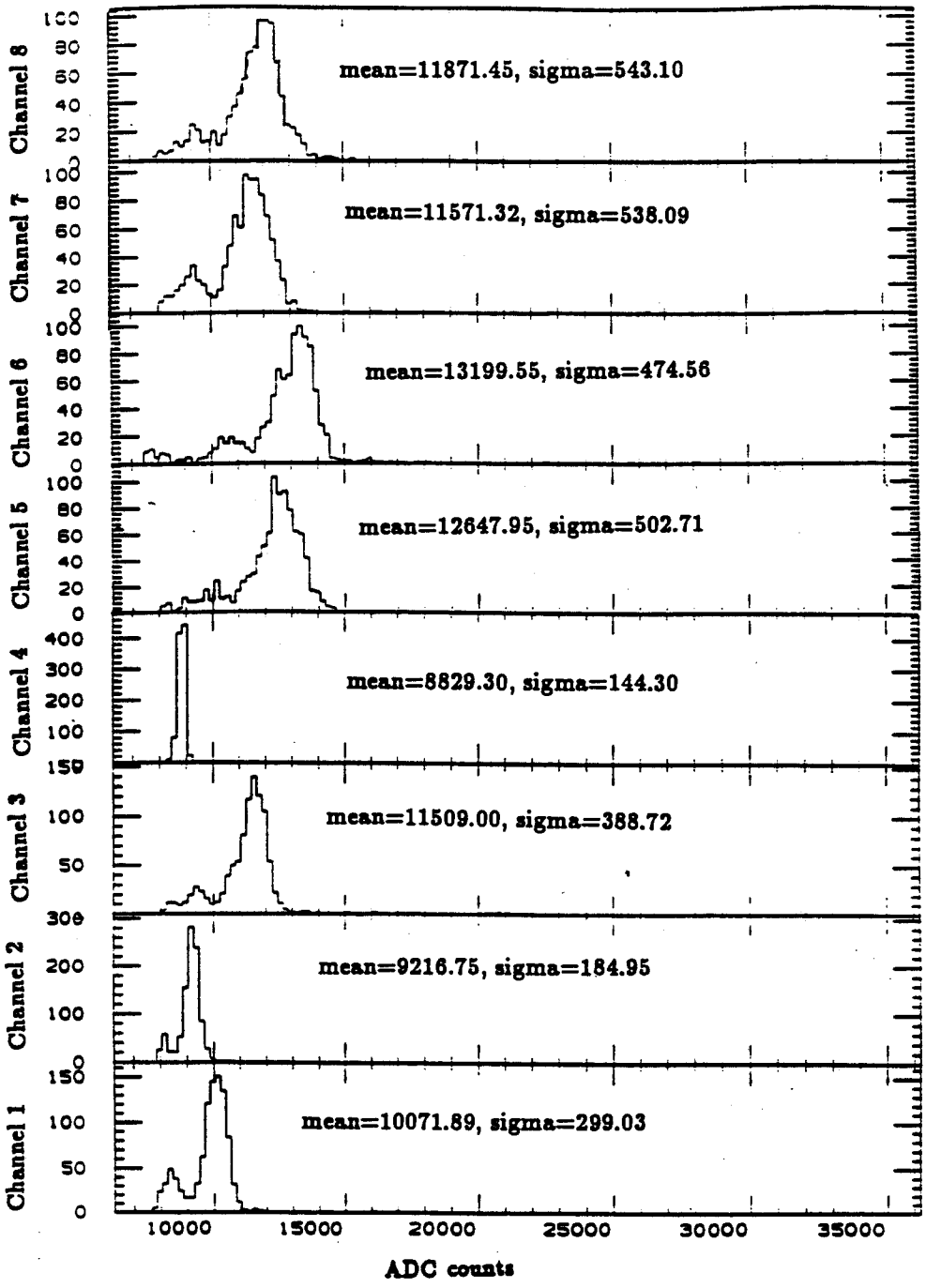

Figure A.5: Variation in peak-pedestal readings for eight 'H' drift cells receiving the same value of high volts.

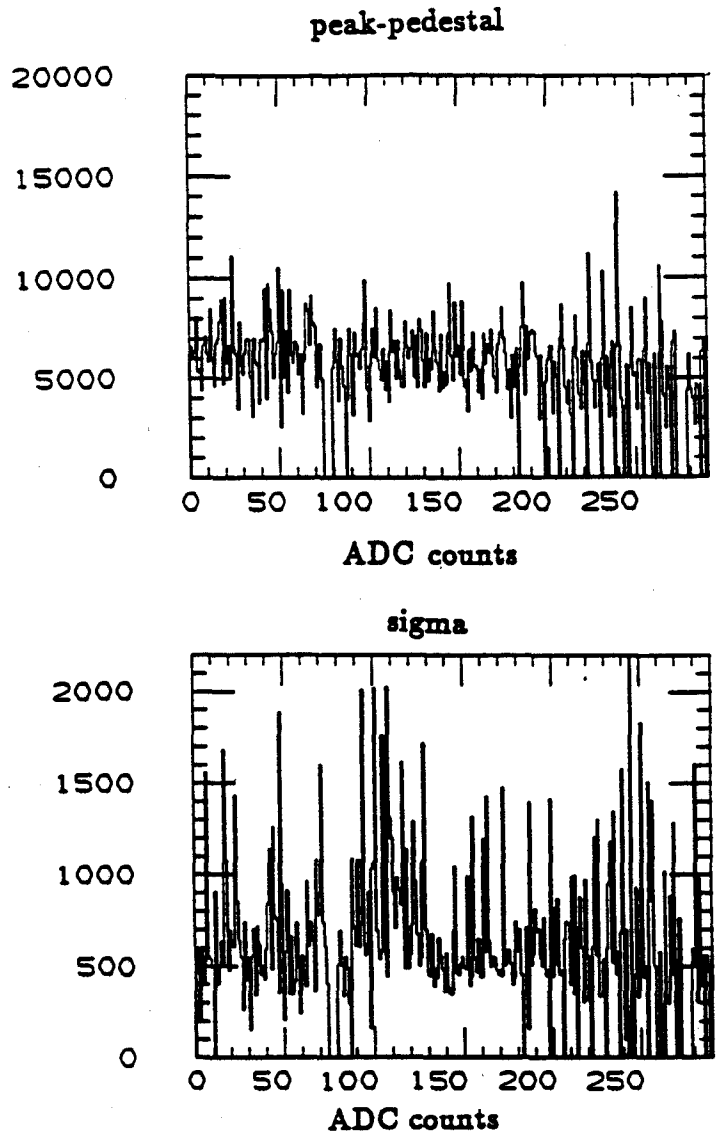

Figure A.6: Digitized peak - pedestal and peak sigmas (in EWE ADC counts) for all Fe-55 source cells in the FMU chambers.

[57] [58] indicate that the gas monitoring scheme achieved an average drift cell efficiency of 94% and an efficiency of 99.6% for the large cells in the detector.

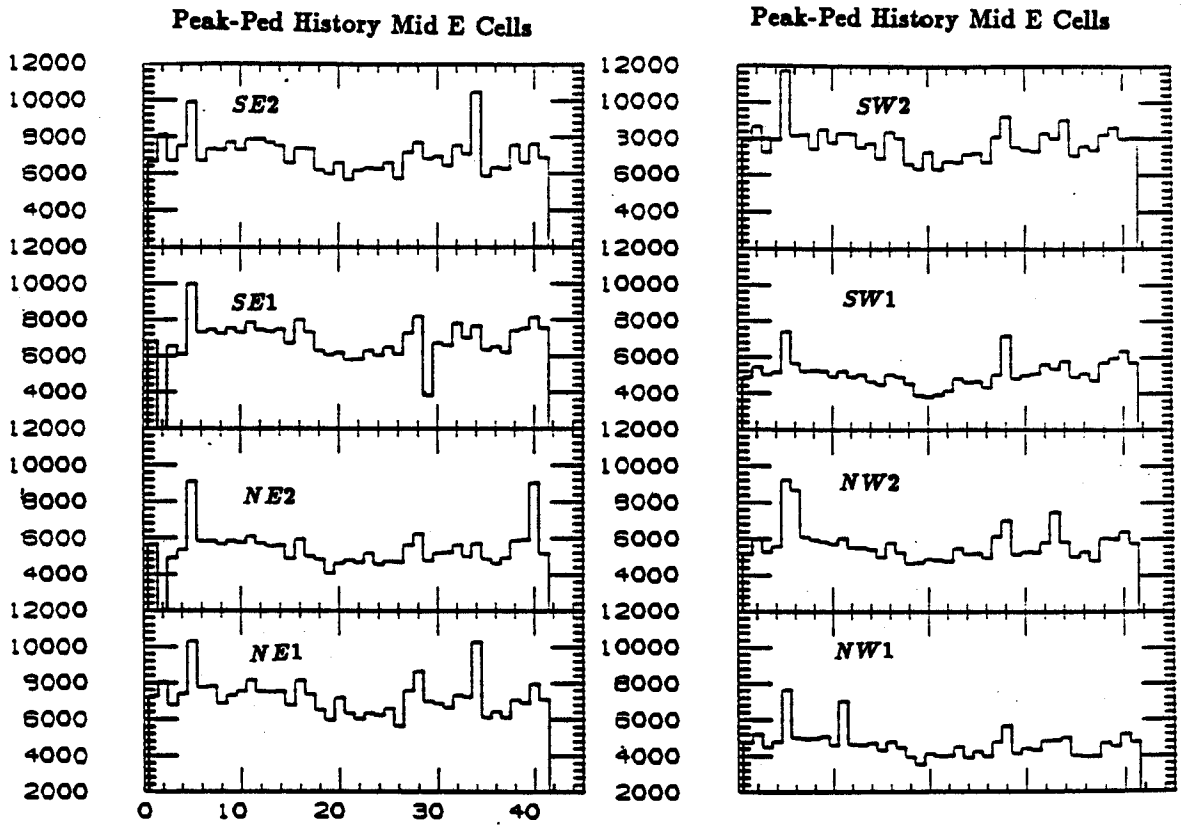

Figure A.7: Variation in peak- pedestal for a middle plane 'E' cell from August 22,1988 through November 27, 1988. Each bin represents 1 day.

Appendix B

Fitting Dimuons to the Z^0 Hypothesis

It is possible to test the hypothesis that a FMUO-CMUO pair is the result of a Z^0 decay without using the momentum of the forward muon. One starts with the assumption that the FMU azimuth and polar angles are measured correctly, and the constraint that the invariant mass of the dimuon be equal to 91.1 GeV/c^2. Next, two equations for the momentum of the forward muon are written in terms the azimuths and polar angles of the two muons, the momentum of the central muon, and the momentum of the Z^0, which is extracted from the missing E_t information recorded for the event, and corrected for the energies of the two muons. The two equations give two predictions, k_1 and k_2, for what the FMU momentum should be, if the mass of the pair is 91.1 GeV/c^2. Using the appropriate elements of the covariance matrices for the central muon 3-momentum, and for the forward muon ϕ and θ, one can calculate σ's for k_1 and k_2, and from there, a χ^2.

Minimizing the χ^2 gives the value of FMU momentum most consistent with the hypothesis that the event is a Z^0 decay. The magnitude of the χ^2 is a measure of the goodness of the fit to that hypothesis. This approach is another means of separating Z^0 candidates from background, while avoiding the problem of possible mismeasurement of the the FMU momenta. Let ϕ_{cm}, θ_{cm} and P^{cm} designate the azimuth, polar angle, and 3-momentum of the central muon. The azimuthal and polar angles of the central muon, written in terms of its momentum components, are given by:

$$\phi_{cm} = \tan^{-1}(P_y^{cm}/P_x^{cm}) \quad \text{(B.1)}$$

$$\theta_{cm} = \tan^{-1}(P_t^{cm}/P_z^{cm}) \quad \text{(B.2)}$$

First, calculate the x and y components of the calorimeter E_t, E_x and E_y, and their errors, ΔE_x, and ΔE_y. Then correct E_x and E_y for the hadronic and electromagnetic calorimeter energy deposited by the muons. The results are the x and y components of the Z^0 momentum. The energies in the missing E_t bank are organized in 24 ϕ slices of 15° a piece. The error on the calorimeter E_t ϕ measurement is given by

$$\delta\phi = 15°/\sqrt{12} \quad \text{(B.3)}$$

The error on the energy measurement for the i^{th} slice is

$$\delta E_i = \sqrt{E_i} \quad \text{(B.4)}$$

E_x and E_y are calculated by summing the x and y components of the calorimeter E_t over the whole detector:

$$E_x = \sum_{i=0}^{23} E_i \cdot \cos\phi_i \tag{B.5}$$

$$E_y = \sum_{i=0}^{23} E_i \cdot \sin\phi_i \tag{B.6}$$

The errors on E_x and E_y are gotten by summing separately the squares of the contributions of the $\delta\phi_i$ and δE_i over the whole detector, then adding the sums in quadrature:

$$(\Delta E_x)^2 = \sum_{i=0}^{23}(\delta E_i \cdot \cos\phi_i)^2 + \sum_{i=0}^{23}(E_i \cdot \sin\phi_i \cdot \delta\phi_i)^2 \tag{B.7}$$

$$(\Delta E_y)^2 = \sum_{i=0}^{23}(\delta E_i \cdot \sin\phi_i)^2 + \sum_{i=0}^{23}(E_i \cdot \cos\phi_i \cdot \delta\phi_i)^2 \tag{B.8}$$

The x and y components of the muon calorimeter energies are written as:

$$E_x^{fm} = (E_{had}^{fm} + E_{em}^{fm}) \cdot \cos\phi_{fm} \sin\theta_{fm} \tag{B.9}$$

$$E_y^{fm} = (E_{had}^{fm} + E_{em}^{fm}) \cdot \sin\phi_{fm} \sin\theta_{fm}$$

$$E_x^{cm} = (E_{had}^{cm} + E_{em}^{cm}) \cdot \cos\phi_{cm} \sin\theta_{cm}$$

$$E_y^{cm} = (E_{had}^{cm} + E_{em}^{cm}) \cdot \sin\phi_{cm} \sin\theta_{cm}$$

Finally, the x and y components of the total calorimeter E_t are corrected for the muon energies like so:

$$E_x^0 = E_x - E_x^{fm} - E_x^{cm} \tag{B.10}$$

$$E_y^0 = E_y - E_y^{fm} - E_y^{cm}$$

Next, E_x and E_y are multiplied by a 'calorimeter energy scale correction factor', E_{scale}, which has been determined empirically to be 1.35. (See the section at the end of this appendix entitled 'Calorimetry Scale Correction Factor' for an explanation of this number):

$$\begin{aligned} E'_x &= E^0_x \cdot E_{scale} \\ E'_y &= E^0_y \cdot E_{scale} \end{aligned} \tag{B.11}$$

These are the x and y components of the Z^0 momentum which will be used with the central muon momenta to predict P^{fm}. Now that all the missing E_t information has been collected together, one can write the first of the two equations for the momentum of the forward muon by using the equation for the invariant mass of the FMU-CMU pair:

$$M^2_{Z^0} = (E_{fm} + E_{cm})^2 - (\vec{P}^{fm} + \vec{P}^{cm})^2 \tag{B.12}$$

$$\begin{aligned} &= E^2_{fm} + E^2_{cm} + 2E_{fm} \cdot E_{cm} - (P^{fm}_x + P^{cm}_x)^2 - (P^{fm}_y + P^{cm}_y)^2 \\ &\quad -(P^{fm}_z + P^{cm}_z)^2 \end{aligned}$$

$$\begin{aligned} &= E^2_{fm} - P^2_{fm} + E^2_{cm} - P^2_{cm} + 2 \cdot (E_{fm} \cdot E_{cm} - P^{fm}_x P^{cm}_x \\ &\quad -P^{fm}_y P^{cm}_y - P^{fm}_z P^{cm}_z) \end{aligned} \tag{B.13}$$

$$\approx 2 \cdot (P_{fm} P_{cm} - P^{fm}_x P^{cm}_x - P^{fm}_y P^{cm}_y - P^{fm}_z P^{cm}_z) \tag{B.14}$$

where the mass of the muon is taken to be ≈ 0:

$$m^2_\mu = E^2_{fm} - P^2_{fm} \tag{B.15}$$

$$= E_{cm}^2 - P_{cm}^2$$

$$\approx 0$$

Writing the muon momenta in terms of angles θ and ϕ, one has

$$P_x^{fm} = P^{fm} \cdot \sin\theta_{fm} \cos\phi_{fm} \quad \text{(B.16)}$$

$$P_x^{cm} = P^{cm} \cdot \sin\theta_{cm} \cos\phi_{cm} \quad \text{(B.17)}$$

$$P_y^{fm} = P^{fm} \cdot \sin\theta_{fm} \sin\phi_{fm}$$

$$P_y^{cm} = P^{cm} \cdot \sin\theta_{cm} \sin\phi_{cm}$$

$$P_z^{fm} = P^{fm} \cdot \cos\theta_{fm}$$

$$P_z^{cm} = P^{cm} \cdot \cos\theta_{cm}$$

Substituting the relations of B.18 into equation B.14 , one has

$$M_{Z^0}^2 = 2P^{fm}P^{cm} \cdot (1 - \cos\theta_{fm}\cos\theta_{cm} - \sin\theta_{fm}\sin\theta_{cm}\cos(\phi_{fm} - \phi_{cm})) \quad \text{(B.18)}$$

By solving for the momentum of the forward muon, equation B.18 becomes

$$P^{fm} = \frac{M_{Z^0}^2}{(2P^{cm} \cdot (1. - \cos\theta_{cm}\cos\theta_{fm} - \sin\theta_{cm}\sin\theta_{fm}\cos(\phi_{cm} - \phi_{fm}))} \quad \text{(B.19)}$$

One can derive a second equation for the FMU momentum by starting with the requirement that the momentum components of the muons equal those of the total, corrected, calorimeter E_t in the event (i.e., the E_t of the Z^0):

$$P_i^{fm} + P_i^{cm} + E_i^Z = 0 \quad \text{(B.20)}$$

where $i = x, y, z$.

By rotating the $x-y$ plane about the z-axis by an amount ϕ_{fm}, so that the resulting x'-axis coincides with the direction of the forward muon transverse momentum (i.e. $P_{x'}^{fmu} = P_t^{fmu}$ and $P_{y'}^{fmu} = 0$), equation B.20 becomes for the x' components:

$$P_t^{fm} = -P_{x'}^{cm} - E_{x'}^{Z} \tag{B.21}$$

or

$$P^{fm} \cdot \sin\theta_{fm} = -P_{x'}^{cm} - E_{x'}^{Z} \tag{B.22}$$

where

$$P_t^{fm} = P^{fm} \cdot \sin\theta_{fm} \tag{B.23}$$

Solving for the momentum of the forward muon, one obtains

$$P^{fm} = \frac{-P_{x'}^{cm} - E_{x'}^{Z}}{\sin\theta_{fm}} \tag{B.24}$$

where, in this rotated coordinate system,

$$E_{x'}^{Z} = E_x^{Z} \cdot \cos\phi_{fm} + E_y^{Z} \cdot \sin\phi_{fm} \tag{B.25}$$

$$E_{y'}^{Z} = E_y^{Z} \cdot \cos\phi_{fm} - E_x^{Z} \cdot \sin\phi_{fm} \tag{B.26}$$

$$P_{x'}^{cm} = P_x \cdot \cos\phi_{fm} + P_y^{cm} \cdot \sin\phi_{fm} \tag{B.27}$$

$$P_{y'}^{cm} = P_y \cdot \cos\phi_{fm} - P_x^{cm} \cdot \sin\phi_{fm} \tag{B.28}$$

Also, in the rotated system, since $P_{y'}^{fmu} = 0$, so

$$E_{y'}^{Z} + P_{y'}^{cm} = 0 \tag{B.29}$$

Call the values of forward muon momentum given by equations B.24 and B.19 k_1 and k_2, respectively. For a function f which is a function of variables A and B, i.e. $f = f(A, B)$, the variance, σ^2, is given by

$$\sigma_f^2 = (\frac{\partial f}{\partial A})^2 \cdot \sigma_A^2 + (\frac{\partial f}{\partial B})^2 \cdot \sigma_B^2 \tag{B.30}$$

So, for k_1 and k_2,

$$\sigma_1^2 = \frac{k_1^2}{\tan^2\theta_{fm}} \cdot \Delta^2\theta_{fm} + \frac{(\Delta P_{x'}^{cm})^2 + (\Delta E_{x'}^{Z})^2}{\sin^2\theta_{fm}} \tag{B.31}$$

$$\begin{aligned}\sigma_2^2 = {} & \Delta P_{xx}^{cm} \cdot (\frac{\partial k_2}{\partial P_x^{cm}})^2 + 2. \cdot \frac{\partial k_2}{\partial P_x^{cm}} \cdot \frac{\partial k_2}{\partial P_y^{cm}} \cdot \Delta P_{xy} \\ & + 2. \cdot \frac{\partial k_2}{\partial P_y^{cm}} \cdot \frac{\partial k_2}{\partial P_z^{cm}} \cdot \Delta P_{yz} + 2. \cdot \frac{\partial k_2}{\partial P_x^{cm}} \cdot \frac{\partial k_2}{\partial P_z^{cm}} \cdot \Delta P_{xz} \\ & + \Delta P_{yy}^{cm} \cdot (\frac{\partial k_2}{\partial P_y^{cm}})^2 + \Delta P_{zz}^{cm} \cdot (\frac{\partial k_2}{\partial P_z^{cm}})^2 + (\Delta\theta_{fm})^2 \cdot (\frac{\partial k_2}{\partial \theta_{fm}})^2 \\ & + (\Delta\phi_{fm})^2 \cdot (\frac{\partial k_2}{\partial \phi_{fm}})^2\end{aligned} \tag{B.32}$$

$$\sigma_3^2 = (\Delta E_{y'}^{Z})^2 + (\Delta P_{y'}^{cm})^2$$

where σ_3^2 originates from the requirement that the transverse energies balance in the rotated frame. $\Delta\theta_{fm}$ and $\Delta\phi_{fm}$ are the errors on the FMU polar and azimuthal angles, respectively. ΔP_{xx}^{cm}, ΔP_{yy}^{cm}, ΔP_{zz}^{cm}, ΔP_{xy}^{cm}, ΔP_{yz}^{cm}, and ΔP_{xz}^{cm}, are the track covariances of the central muon, written in terms of the following

CTC track quantities: the track curvature, CRV, the CTC momenta components P_x, P_y, and P_z, the transverse momentum, P_t, the covariance of cot θ, Δcot_c, and the covariance of ϕ, $\Delta\phi_c$:

$$\begin{aligned}
\Delta P^{cm}_{xx} &= \Delta\phi_c \cdot P_y^2 + CRV^2 \cdot P_x^2 \\
\Delta P^{cm}_{yy} &= \Delta\phi_c \cdot P_x^2 + CRV^2 \cdot P_y^2 \\
\Delta P^{cm}_{zz} &= \Delta cot_c \cdot P_t^2 + CRV^2 \cdot P_z^2 \\
\Delta P^{cm}_{xy} &= P_x P_y \cdot (CRV^2 - \Delta\phi_c) \\
\Delta P^{cm}_{yz} &= P_y P_z \cdot CRV^2 \\
\Delta P^{cm}_{xz} &= P_x P_z \cdot CRV^2
\end{aligned} \tag{B.33}$$

The errors on the Z^0 E_t and the CMUO momentum in the rotated frame, $(\Delta E^Z_{x'})^2$ and $(\Delta P^{cm}_{x'})^2$, are written in terms of the unrotated quantities as :

$$\begin{aligned}
(\Delta E^Z_{x'})^2 &= (\Delta E_x \cdot \cos\phi_{fm})^2 + (\Delta E_y \cdot \sin\phi_{fm})^2 \\
&\quad +(\Delta\phi_{fm})^2 \cdot (E_y \cos\phi_{fm} - E_x \sin\phi_{fm})^2 \\
(\Delta E^Z_{y'})^2 &= (\Delta E_y \cdot \cos\phi_{fm})^2 + (\Delta E_x \cdot \sin\phi_{fm})^2 \\
&\quad +(\Delta\phi_{fm})^2 \cdot (E_y \sin\phi_{fm} - E_x \cos\phi_{fm})^2
\end{aligned} \tag{B.34}$$

and

$$(\Delta P^{cm}_{x'})^2 = \Delta P^{cm}_{xx} \cdot \cos^2\phi_{fm} + \Delta P^{cm}_{xx} \cdot \sin^2\phi_{fm} + 2 \cdot \Delta P^{cm}_{xy} \cos\phi_{fm} \tag{B.35}$$

$$\cdot \sin\phi_{fm} + (\Delta\phi_{fm})^2 \cdot (P_y \cos\phi_{fm} - P_x^{cm} \sin\phi_{fm})^2$$

$$(\Delta P_{y'}^{cm})^2 = \Delta P_{yy}^{cm} \cdot \cos^2\phi_{fm} + \Delta P_{yy}^{cm} \cdot \sin^2\phi_{fm} + 2 \cdot \Delta P_{xy}^{cm} \cos\phi_{fm}$$

$$\cdot \sin\phi_{fm} + (\Delta\phi_{fm})^2 \cdot (P_x \cos\phi_{fm} + P_y^{cm} \sin\phi_{fm})^2$$

where ΔE_x and ΔE_x, are as calculated in equation B.8.

The partial derivatives of k_2 with respect to P_x^{cm}, P_y^{cm}, and P_z^{cm} are given by

$$\frac{\partial k_2}{\partial P_x^{cm}} = k_1 \cdot \{\frac{-P_x^{cm}}{P_{cm}^2} \tag{B.36}$$
$$- [\sin\theta_{cm}\cos\theta_{fm} - \cos\theta_{cm}\sin\theta_{fm}\cos(\phi_{cm} - \phi_{fm})]$$
$$\cdot \frac{P_z^{cm} P_x^{cm}}{P_{cm}^2 P_t^{cm} \cdot denom} + \sin\theta_{cm}\sin\theta_{fm}\sin(\phi_{cm} - \phi_{fm})$$
$$\cdot \frac{P_y^{cm}}{P_t^{cm} \cdot P_t^{cm} \cdot denom}\}$$

$$\frac{\partial k_2}{\partial P_y^{cm}} = k_2 \cdot \{\frac{-P_y^{cm}}{P_{cm}^2} \tag{B.37}$$
$$- [\sin\theta_{cm}\cos\theta_{fm} - \cos\theta_{cm}\sin\theta_{fm}\cos(\phi_{cm} - \phi_{fm})]$$
$$\cdot \frac{P_y^{cm} P_z^{cm}}{P_{cm}^2 P_t^{cm} denom} - \sin\theta_{cm}\sin\theta_{fm}\sin(\phi_{cm} - \phi_{fm})$$
$$\cdot \frac{P_x^{cm}}{P_t^{cm} P_t^{cm} \cdot denom}\}$$

$$\frac{\partial k_2}{\partial P_z^{cm}} = k_2 \cdot \{\frac{-P_z^{cm}}{P_{cm}^2} \tag{B.38}$$
$$+ [\sin\theta_{cm}\cos\theta_{fm} - \cos\theta_{cm}\sin\theta_{fm} \cdot \cos(\phi_{cm} - \phi_{fm})]$$
$$\cdot \frac{P_t^{cm}}{P_{cm}^2 \cdot denom}\}$$

$$\frac{\partial k_2}{\partial \theta_{fm}} = -k_2 \cdot \frac{\cos\theta_{cm}\sin\theta_{fm} - \sin\theta_{cm}\cos\theta_{fm}\cos(\phi_{cm}-\phi_{fm})}{denom} \quad \text{(B.39)}$$

$$\frac{\partial k_2}{\partial \phi_{fm}} = k_2 \cdot \frac{\sin\theta_{cm}\sin\theta_{fm}\sin(\phi_{cm}-\phi_{fm})}{denom} \quad \text{(B.40)}$$

where

$$denom = 1. - \cos\theta_{cm}\cos\theta_{fm} - \sin\theta_{cm}\sin\theta_{fm}\cos(\phi_{cm}-\phi_{fm}) \quad \text{(B.41)}$$

Writing χ^2 in the form

$$\chi^2 = \sum_{i=1}^{j} \frac{(k^* - k_i)^2}{\sigma_i^2} \quad \text{(B.42)}$$

one has

$$\chi^2 = \frac{(k^* - k_1)^2}{\sigma_1^2} + \frac{(k^* - k_2)^2}{\sigma_2^2} + \frac{(E_{y'} + P_{y'}^{cm})^2}{\sigma_3^2} \quad \text{(B.43)}$$

The best value of forward muon momentum, k^*, comes from minimizing equation 1.29 with respect to k^*, and is written as

$$k^* = \frac{(\sigma_2^2 \cdot k_1 + \sigma_1^2 \cdot k_2)}{(\sigma_1^2 + \sigma_2^2)} \quad \text{(B.44)}$$

B.1 Calorimetry Scale Correction Factor

The reason there is a 'calorimetry scale correction factor' inserted in the calculation of the Z^0's energy components and their errors is that 'we', meaning my

advisor and I, decided that the fitting method outlined above did not give completely sensible answers if $E_{scale} = 1.0$. Approximately 15% of what we believed to be well-identified FMUO-CMUO Z^0's had $\chi^2 > 10$, as did one quarter to one third of the events in the CMUO-CMUO and CMUO-CMIO Z^0 sample. It was found that the σ_3 component of the χ^2, (corresponding to the transeverse energy balance) was very sensitive to the errors on the energies in the problem. So, we fit the entire data sample, FMUO-CMUO, CMUO-CMUO, and CMUO-CMIO with various values of E_{scale}, to see which one gave us the 'best' answer (i.e. the fewest number of real Z^0's with $\chi^2 > 10$. This turned out to be $E_{scale} = 1.35$. Scaling E_x and E_y by 1.35 implied that the error, $\delta E_i = \sqrt{E_i}$ should be scaled by $\sqrt{1.35} = 1.16$, also. This scale factor on the error was rounded down to 1.0 for this analysis.

Bibliography

[1] Decriptions of the Fermilab Tevatron can be found in the following references:

R. Johnson, *Proceedings of the IEEE 1987 Particle Accelerator Conference,* Washington, D.C. 8-12.

P. Martin, *Ibid.,* 47-49.

J. Gannon,*Proceedings of the IEEE 1989 Particle Accelerator Conference,* Chicago, Il. 68-70.

G. Dugan, *Ibid.,* 426-430.

[2] F. Abe, *et. al.,* Nucl. Inst. and Meth. A **271**, 387 (1988), and the references contained therein.

[3] J.Skarha, Ph.D. Thesis. University of Wisconsin at Madison (1989) (unpublished).

[4] *Ibid.*, p. 40.

[5] K. Byrum, Ph.D. Thesis. University of Wisconsin at Madison (1992) (unpublished).

[6] K. Byrum, Private Communication (1991).

[7] A. Gauthier, *Efficiency of the Level 1 Central Muon Trigger.* CDF-937 (1989).

[8] A. Gauthier, *Efficiency of the Level 2 Central Muon Trigger.* CDF-1106 (1990).

[9] For a more detailed description of the theory than is contained in this chapter, see :

V. Barger and R. J. N. Phillips, *Collider Physics.* (Addison-Wesley Publishing Company, Redwood City, California, 1987);

I. J. R. Aitchison and A. J. G. Hey, *Gauge Theories in Particle Physics*, (Adam Hilger, Philadelphia, Pa, 1989);

D. H. Perkins, *Introduction to Particle Physics*, (Addison-Wesley Publishing Company, Redwood City, California, 1982);

F. Halzen and A.D. Martin *Quarks and Leptons*, (Wiley, New York, 1984).

[10] Particle Data Group, Particle Properties Data Booklet, North-Holland (1991).

[11] V. Barger and R. J. N. Phillips, *Collider Physics.* Addison-Wesley Publishing Company (1987). p. 42.

[12] *Ibid.*, p. 43.

[13] *Ibid.*, p. 169.

[14] J. Collins and D. Soper, Phys. Rev. **D 16** (1977) 2219.

[15] D. Kardelis, *A Study of CTC-CMU Matching Cut Efficiency for the W/Z Muon Analysis.* CDF-1336 (1991) (unpublished).

[16] D. Kardelis, *Efficiency of the 'Standard' Muon Tower Calorimeter Cuts for the W/Z Muon Analysis.* CDF-1301 (1991) (unpublished).

[17] S. Eno, *et. al., W/Z Cross-Sections in the Muon Channel.* CDF-1349 (1991) (unpublished).

[18] K. Byrum, *et. al., Forward Muon Chamber Efficiency, Gain, and Resolution Studies.* CDF-1343 (1991) (unpublished).

[19] J. Lamoureux, Private Communication (1991).

[20] R.L. Swartz and D.A. Smith, *Fiducial Cuts for Central Muons.* CDF-1259 (1991) (unpublished).

[21] A. Byon-Wagner *et. al., Cosmic Filtering of Central Muon Events.* CDF-1260 (1990) (unpublished).

[22] P. Berge, Private Communication (1991).

[23] A. Gauthier, *Tracking Studies With Cosmic Rays.* CDF-965 (1989) (unpublished).

[24] A. Gauthier, *Study of Tracking Asymmetry in Cosmic Ray Data.* CDF-1199 (1990) (unpublished).

[25] B. Winer, Ph.D.Thesis. University of California at Berkeley. (unpublished) (1991). 33-34.

[26] F. Paige and S.D. Protopopescu, BNL Report No. BNL 38034, (1986) (unpublished).

[27] P. Hurst, Ph.D. Thesis. University of Illinois at Champaign-Urbana (1990). (unpublished) 39.

[28] K. Byrum, *The Forward Muon Efficiency for the 88/89 Run.* CDF-1600 (1991) (unpublished).

[29] C. Campagnari, *A Fast W and Z Monte Carlo.* CDF-1025 (1989) (unpublished).

[30] P. Derwent *et. al.*, *Measurement of* $\sigma(W \longrightarrow e\nu)$ *and* $\sigma(Z \longrightarrow e^+e^-)$ *in* $p\bar{p}$ *at* $\sqrt{s} = 1.8$ *TeV.* CDF-1107 (1990) (unpublished).

[31] P. Schlabach, Ph.D. Thesis, University of Illinois at Champaign-Urbana. (1990) 38.

[32] J. Proudfoot, *Measurement of Missing E_t in the CDF Calorimeter.* CDF-1011 (1989) (unpublished).

[33] F.E. James and M. Roos, Comput. Phys. Commun. **10**, 343 (1975).

[34] A. Gauthier, *Study of Tracking Asymmetry in Cosmic-Ray Data.* CDF-1199, (1990) (unpublished).

[35] A. Gauthier, *CTC Tracking Studies with Cosmic Rays.* CDF-965, (1989) (unpublished).

[36] D. Smith and L. Holloway, *Azimuth and Charge Dependence of CFT and DF Tracks.* CDF-947 (1989) (unpublished).

[37] P. Hurst, Ph.D. Thesis. 81.

[38] J. Freeman, *Description of the CDF Detector Simulation Program CDFSIM.* Internal CDF document. (1985).

[39] K. Byrum, Private Communication (1991).

[40] F. Abe, *et. al.,* Phys. Rev. Lett. **67**, 1502 (1991).

[41] P. Hurst, Private Communication (1991).

[42] P. Chiappetta, Z. Phys. **C 32**, 521-526 (1986).

[43] F.A. Berends, Z. Phys. **C 27**, 365-372 (1985).

[44] P. Hurst, Ph.D. Thesis. 103-115.

[45] D. Decamp, *et. al.*, Z. Phys. C **32**, 365-391 (1990).

[46] B. Adeva, *et. al.*, Z. Phys. C **51**, 179-203 (1991).

[47] F. Abe, *et. al.*, Phys. Rev. Lett. **67**, 2609 (1991).

[48] P. Hurst, Private Communication (1991).

[49] P. Hurst, Ph.D. Thesis, 115.

[50] R. Cahn, Phys. Rev. D **36** 2666 (1987).

[51] E. A. Kuraev and V. S. Fadin, Yad. Fiz. 41, 4661 (1985) [Sov. J. Nucl. Phys. 41, 466 (1985)].

[52] T. Ferbel, *Experimental Techniques in High Energy Physics.* (Addison-Wesley Publishing Co., Menlo Park, California, 1987).

[53] US NIM Committee, *CAMAC Tutorial Articles* Energy Research and Development Administration, Washington, D.C., October 1976, TID-26618.

[54] G.Drake, *et. al.*, CDF Front End Electronics: The RABBIT System. Nuclear Instruments and Methods in Physics Research, A269 (1988) 68-81.

[55] Louis Costrel, CAMAC Instrumentation System - Introduction and General Description National Bureau of Standards, Washington, D.C.

[56] L. Demortier, *The CDF Gas Gain Data Acquisition System.* CDF-533 (1988) (unpublished).

[57] K. Byrum, *Forward Muon Chamber Efficiency, Gain, and Resolution Studies.* CDF-1343 (1991) (unpublished).

[58] J. Lamoureux, *The Forward Muon Efficiency for the 88/89 Run.* CDF-1597 (1991) (unpublished).